MODELING AND IDENTIFICATION OF AN AXIALLY-MOVING CANTILEVER BEAM

Liyan Deng ©

November 15, 2002

A THESIS SUBMITTED IN PARTIAL FULFILLMENT OF THE
REQUIREMENTS OF THE MScENG DEGREE
IN
CONTROL ENGINEERING
FACULTY OF ENGINEERING
LAKEHEAD UNIVERSITY
THUNDER BAY, ONTARIO

Your file Votre référence
ISBN: 0-612-83404-2
Our file Notre référence
ISBN: 0-612-83404-2

Abstract

An axially-moving cantilever beam is used to study identification of time-varying systems. A circuitry for DC motor current control and sensor conditioning is built. The circuitry meets the design requirement of controlling the axial motion of the beam and amplifying the sensor signals.

A linear time-varying model governing lateral vibration of the beam is developed. Computer simulation is conducted to study the dynamic properties of the system, such as transient responses, varying state transition matrices, "frozen" modal parameters, "pseudo" modal parameters, etc.

A previously developed algorithm is applied to identify the system. Two identification tasks are carried out. The system identification determines the discrete-time state space model of the system. The modal parameter identification determines the "pseudo" modal parameters of the system. In both cases, an ensemble of freely vibrating responses are used. The study addresses several critical issues encountered in the experiment such as excitation, data preprocessing, the beam motion control, etc. The study also investigates several important factors that affect the accuracy of identification, such as the number of necessary experiments, model order, the block row number, etc. An algorithm based on the moving-average method is developed to select the "pseudo" natural frequencies of vibratory modes. The study shows that the algorithm is capable of estimating the "pseudo" natural frequencies of the vibratory modes, present in responses, while it fails to give good estimates for the "pseudo" damping ratios.

Acknowledgements

I gratefully acknowledge my supervisor Dr. K. Liu for his support and responsible supervision. The thesis would not have been possible without his knowledge and guidance. I would like to thank my co-supervisor Dr A. Sedov for his comments on the thesis. I would like to thank Dr. K. Natarajan and Dr. A. Tayebi for their valuable suggestions in designing and testing the circuitry, Mr. M. Klein and Mr. W. Paju for their assistance in building the circuitry, and Mrs. N. Behman and Mrs. D. Lehtinen for their proofreading of my thesis.

I dedicate this work to my wife and my parents for their love, patience and support.

Table of Contents

List of Figures

List of Tables

List of Acronyms

- BSG Base Strain Gauge
- LTI Linear Time-Invariant
- LTV Linear Time-Varying
- MSG Middle Strain Gauge
- MOSFET Metal-Oxide Field-Effect Transistor
- MAC Middle Accelerometer
- SNR Signal to Noise Ratio
- SVD Singular Value Decomposition
- TAC Tip Accelerometer
- $IPNF_i$ ith Identified "pseudo" Natural Frequency

Chapter 1

Introduction

The dynamics of axially-moving cantilever beams and strings have received a good deal of attention in connection with vibration problems of time-varying mechanical systems, such as band saw blades, paper and magnetic tapes, threadline in textile industry, high-rise elevators, spacecraft antennae and tethered satellite in space exploration, robotic arms with prismatic joint [1-7]. This study is motivated to develop an axially-moving cantilever beam system for study of identification and control of time-varying mechanical systems. The main task of the research is to develop an experimental system, to develop an analytical model of the system, and to identify the system.

The rest of this chapter is organized as follows: Section 1.1 overviews the previous studies on axially-moving cantilever beams, Section 1.2 overviews the previous studies on time-varying systems, Section 1.3 reviews identification methods of linear time-varying systems, Section 1.4 lists the objectives of the thesis research, and Section 1.5 outlines the thesis.

1.1 Overview of the Previous Studies on Axially-Moving Cantilever Beams

The studies on axially-moving cantilever beams can be classified into two areas: modeling and control. Efforts in modeling have been made in two different aspects. One is analytical modeling; The other is identification as described in section 1.3.

Studies dealing with the mathematical modeling of axially-moving cantilever beams are re-

ported in [1-9]. The models are derived by applying Newton's second law, extended Hamilton's principle or Lagrangian formulation based on the assumption that the deflection gradients of the beam are small and the beam is axially rigid. The axial motion influences the dynamics of the axially-moving cantilever beams. A positive damping effect is induced by axial extension and a negative damping effect is induced by axial retraction respectively [2]. The extending and retracting motions of a flexible robot arm have destabilizing and stabilizing effects on the arm vibration based on the fact the deflection at the tip of the beam becomes large during axial extension and small during axial retraction respectively [4]. The motion-induced vibration is considerable and the vibration of the tail section of the robotic arm can cause appreciable position errors [5]. The deflection and velocity of an axially-moving cantilever beam are simulated numerically [7]. It is found that the axial extension increases the amplitude of the deflection due to a reduced stiffness while the axial retraction reduces the deflection of the beam due to an increased stiffness. Also, the axial extension decreases the amplitudes of the vibration velocity because of dissipation of vibration energy while the axial retraction increases the amplitudes of the vibration velocity because of absorption of vibration energy [7].

To date, little effort has been made in modeling the axially-moving cantilever beam systems using state space representation. Also, little work has been done in analyzing the contributions of generalized coordinates, generalized velocities, and/or vibratory modes to the transient responses including strain, deflection, velocity and acceleration in the axially-moving cantilever beam system. This is the first motivation of the present study.

1.2 Overview of the Previous Studies on Time-Varying Systems

The studies on time-varying systems may be classified into two groups. One is the theoretical analysis of controllability and observability of time-varying systems [10-13]. The other is the analysis of modal parameters of time-varying systems. It is noted that a LTV (linear time-varying) system violates one of the assumptions of the conventional modal analysis, that is, stationarity. The concept of the "pseudo" modal parameters was introduced in [14,16]. They are obtained by conducting eigendecomposition of the varying discrete-time state transition matrices [16]. The identification of the "pseudo" modal parameters for LTV systems was

extended to the cases of forced responses and forcing inputs in [14]. The applicability of the "pseudo" modal parameters based on the "pseudo" transfer function are also reported in time-varying structures in [15]. However, the algorithms developed have only been verified using computer simulation. To implement the algorithm experimentally is the second motivation of this study.

1.3 Identification of Linear Time-Varying Systems

In order to design a high performance active control system, an accurate system model is a prerequisite. It is difficult to obtain an accurate mathematical model due to the fact that irregularities, including physical damping effect and nonlinear factors, exist in the system. On the other hand, identification obtains a system model based on experimental data. Such a model can represent the actual system better.

Adaptive method is a popular method in time-varying system identification. It uses recursive algorithm to estimate or identify the time-dependent parameters of the model which is assumed to be a polynomial. The feature of this method is the use of data from a single experiment [17]. Ensemble method is an alternative approach to time-varying system identification. The feature of the method is the use of multiple input and output data from multiple experiments, and each of the experiments must experience the same time-varying change. The key of the ensemble method is concerned with three steps. First, a series of Hankel matrices are formed by an ensemble of the freely vibrating responses from multiple experiments; Second, the varying state transition matrix at each moment is estimated through the SVD (singular value decomposition) of two successive Hankel matrices; Third, the "pseudo" modal parameters are obtained by conducting the eigendecomposition of the varying state transition matrix [16]. The varying state transition matrices can also be estimated using forced responses and forcing inputs. The "pseudo" modal parameters are evaluated by conducting eigendecomposition of the varying state transition matrices [14]. The identification algorithms mentioned in [14] and [16] have been successfully verified using computer simulation. A wavelet-based approach for the identification of a linear time-varying lumped-mass system is reported in [19]. However, it is noted that experimental identification of LTV systems remains a relatively inactive area that deserves

more attention. Meanwhile, little effort has been made to identify the axially-moving cantilever beam system with time-varying state transition matrix and the time-varying output matrix.

To capture the dynamics of the system, the model to be identified should be overparameterized [20-25]. The overparameterized model contains both the system modes and computational modes caused by the noise or irregularity of the system. It is important to distinguish between these modes. To qualify the contribution of individual modes to pulse responses, mode singular value is defined in [23]. Modal response magnitude is also proposed to qualify the maximum contribution of the individual modes to the responses [21-22]. However, this research is limited to time-invariant systems.

It can be inferred that the overparameterized model contains system modes and computational modes at each time moment if a system is time-varying. It is expected that for the case of time-varying systems, selection of the system modes among the identified modes is more challenging than the case of time-invariant systems as identification must be conducted at each moment. An effective method to select vibratory modes remains to be found. This is the third motivation for the present study.

1.4 Objectives of the Research

1. The first objective of the research is to build a motor current control and sensor signal conditioning circuitry in order to control axial motion of the cantilever beam and amplify the sensor signals.

2. The second objective of the research is to develop an analytical model and conduct a computer simulation in order to understand the dynamics of the system.

3. The third objective of the research is to apply an identification algorithm to the axially-moving cantilever beam system and to identify the model of the system.

1.5 Outline of the Thesis

The following chapters of the thesis are organized as follows: Chapter 2 describes the development of the experimental system, Chapter 3 develops an analytical model for the axially-moving

cantilever beam and presents some computer simulation results, Chapter 4 focuses on identification of the system, and Chapter 5 draws the conclusions of the study and recommends future work.

Chapter 2

The Experimental System

This chapter presents the development of the experimental system. The entire system consists of three subsystems: (1) an axially-moving cantilever beam apparatus, (2) a motor current control and sensor signal conditioning circuitry, (3) the system of a data acquisition (DAQ) and PC computer; all shown in Figure 2-1.

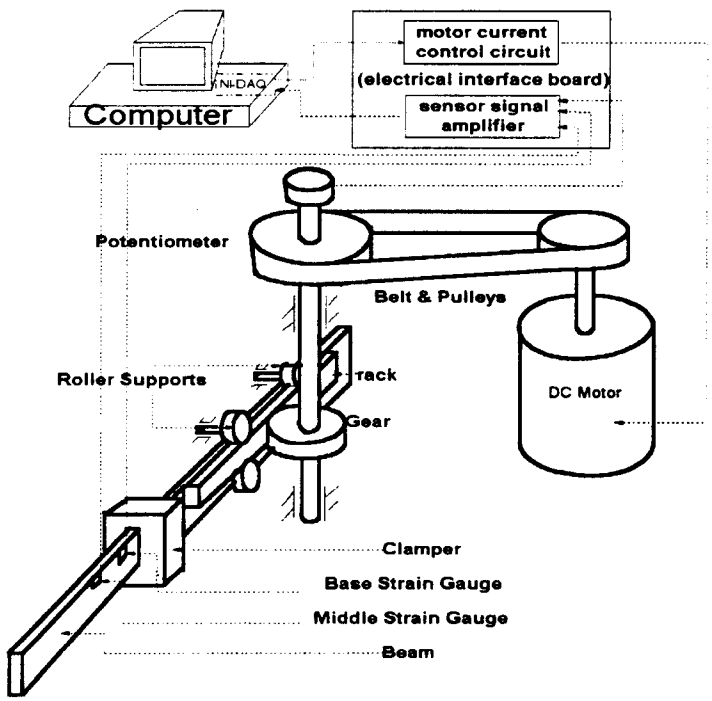

Figure 3.1 The experimental system

The chapter is organized as follows: Section 2.1 describes the axially-moving cantilever

beam apparatus, section 2.2 describes the DAQ board and PC computer, section 2.3 presents the development of the motor current control and sensor conditioning circuitry, and section 2.4 is a brief summary.

2.1 Axially-Moving Cantilever Beam Apparatus

The apparatus was designed and built by Mr Ahmed Hage as his Bechelor Degree project [29]. It consists of a 12V DC permanent magnet reversible motor, a belt and pulley set, rack and pinion, and the beam. The motor has a built-in gearbox with a transmission ratio of 13:1. The motor idle speed is 180 rpm. The speed under a load of 24 in-lb on the shaft is 160 rpm @ 6.2 to 7.2 amps. Under a 45 in-lb load, the output speed is 145 rpm @ 10.5 to 11.6 amps. The transmission ratio of the belt and pulley set can be 1.9, 2.9, or 5.2 by changing the large pulley. The center distance of two pulley shafts is 3.96 inches. In order to measure the angular position of the large pulley shaft, or the axial displacement of the cantilever beam, a pot is attached at one end of the large pulley shaft. The cantilever beam is made from 6061-T6 aluminum-magnesium-silicon alloy and its dimension are 1850 mm (length) $\times$50.6 mm (width) $\times$3.175 mm (thickness). A clamp is used to ensure the boundary conditions at the clamped end. In order to measure the lateral vibration signals of the beam, the strain gauge sensors are bonded on the beam surface at two positions. One refers to as base strain gauge (BSG), the other refers to as middle strain gauge (MSG).

2.2 DAQ Board and Computer

The computer used to control the system is a Pentium III with a speed of 1000MHz and 128MB RAM. The DAQ board is a National Instruments PCI Series Model PCI-MIO-16E-4, which has a resolution of 12 bits, 16 single-ended or 8 differential analog input channels with maximum sampling rate of 500KS/s, 2 D/A output channels with a maximum update rate of 1MS/s, eight digital IOs, and two counters. Labview is used for programing.

The voltage command from one of the analog output channels (DAC0 and DAC1) of the DAQ board in the computer is referred to as setpoint. It serves as an input that can be separated into two signals: one is the magnitude signal and the other is the direction signal in

signal separation circuit (see in section 2.3.1). The magnitude and direction signals are used to control the magnitude and direction of the motor current, respectively. The relationship between motor current and the setpoint voltage is shown in Figure 2.2 and the testing method is described in section 2.3.2. A proportional gain between the magnitude of the setpoint voltage in Channel DAC0 and motor current is 0.5 A/V within the range of 0V to 3V. As long as the setpoint voltage exceeds 3V, the motor current saturates.

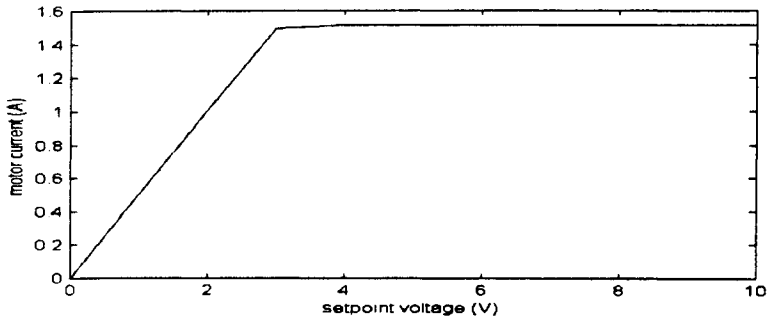

Figure 2.2 Relationship between setpoint voltage and motor current

2.3 Motor Current Control and Sensor Signal Conditioning Circuitry

One of the main tasks of this project is to build an electrical circuitry. The decision of building the circuitry in house was due to the limited budget and a training opportunity for the author to gain some practical experience in electrical engineering. The requirements for the circuitry are

1. to control the magnitude and direction of motor currents;

2. to amplify the signals of potentiometer and strain gauges.

The circuitry design was based on the one used in previous projects [26-27]. Some mistakes in the original schematic drawings have been found and corrected accordingly. The overall circuitry, shown in Figure 2.3, consists of motor power supply module, bridge module, power supply module, current control module, signal separation module, sensor modules including

potentiometer circuit, strain gauge circuits.

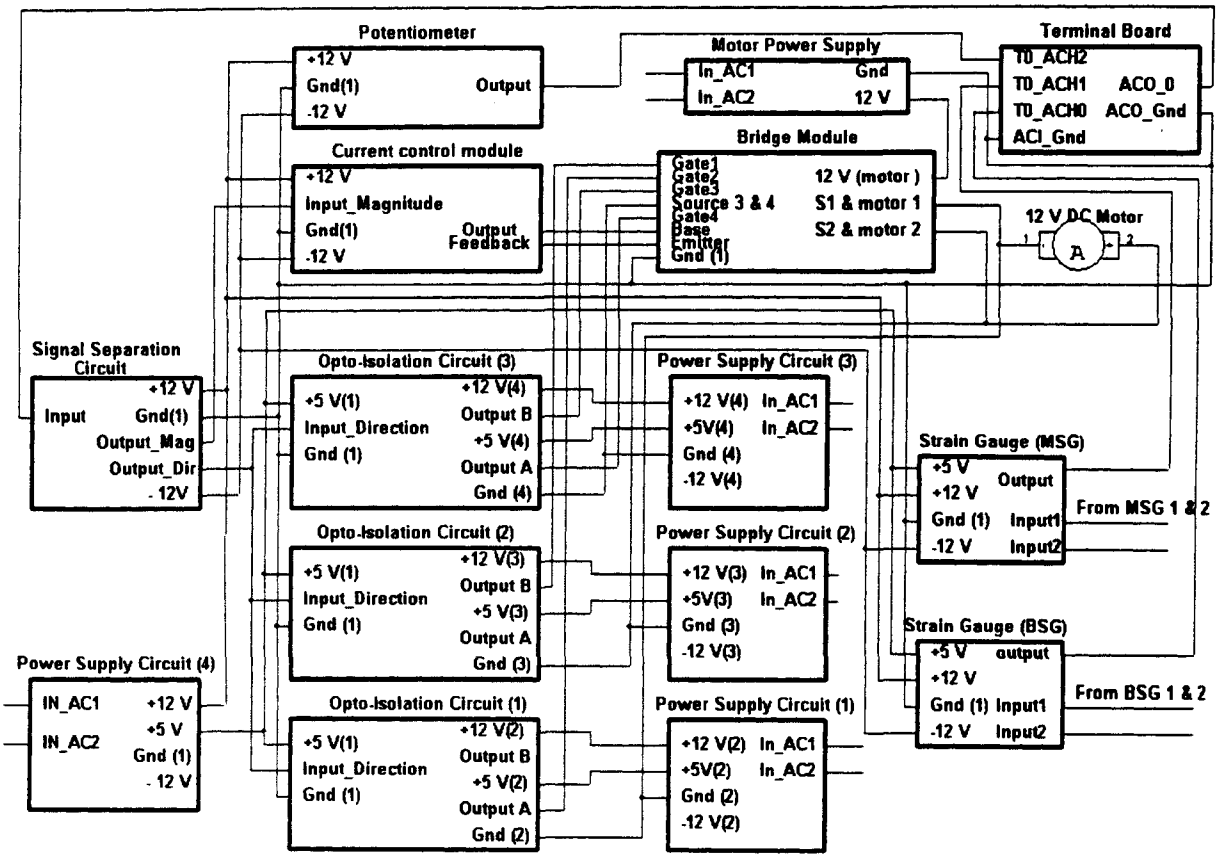

Figure 2.3 Motor current control and sensor conditioning circuitry

2.3.1 Description of Individual Circuits

(1) Motor Power Supply Module

The schematic of motor power supply circuit is shown in Figure A2.1 of Appendix A. The module provides an DC power source to the current amplification circuit of transistor 2N6059 in bridge module in order to change the magnitude and direction of the motor current. It is capable of providing maximum 5A DC currents at 12V. The module consists of a transformer, a fuse, a diode bridge, a RC filter, and a current boost circuit. A transformed AC waveform is rectified by the diode bridge. Then, the rectified DC waveform is passed through the RC filter to obtain a smooth waveform. The transistor 2N6052 is used to amplify or to boost the current. LM 317 is an adjustable voltage regulator and R3 pot resistor is used to obtain and

adjust a desired output voltage. The voltage regulators 7805 and 7912 are used to obtain +5V and -12V voltage respectively.

(2) Bridge Module

As shown in Figure A2.2 of Appendix, there are four MOSFETs (Metal-Oxide Field-Effect Transistors) Q_1, Q_2, Q_3, and Q_4 in the circuit. They are used to switch the current directions. If $Q_1$and Q_3 are on, the motor current flows in one direction; If Q_2 and Q_4 are on, the motor current flows in the opposite direction. Thus, the motor rotation can be reversed. The output of the current control module is applied at the base of the transistor of 2N6059 to obtain a desired current. The actual motor current is detected by measuring voltage of resistor R_9. Since there is an extreme buildup of voltage during the MOSFET switching which can reduce MOSFET's life, the capacitors, resistors and diodes between drain and source of each MOSFET must be used in order to damp high voltage buildup. The resistors at the gates of the MOSFETs are used to damp the noise from the outputs of opto-isolation circuits.

(3) Current Control Module

The circuit is used to control the magnitude of the motor current. It is a proportional (P) and integral (I) controller. The values of corresponding resistors and capacitors are given in the schematic shown in Figure A2.3 of Appendix.

The voltage across 1Ω resistor R_9 in the bridge module shown in Figure A2.2 is fed to the non-inverting terminal of the operational amplifier circuit consisting of an Opamp LM1458 and the two resistors, R_{13} and R_{14}, in the bridge module. The feedback gain is designed to be 2. The output of the amplifier circuit is compared with the reference input from magnitude output of the signal separation module. The output voltage of the current control module is given by

$$u = (1 + \frac{R_{12}}{R_{11}}) \left(\frac{R_{10}}{R_8} \frac{R_7}{R_5} e + \frac{R_{10}}{R_9} \frac{1}{R_6 C_1} \int_0^t e dt \right) \qquad (2\text{-}1)$$

where e is the error between the reference input and the feedback voltage. $R_{10}/R_8 = R_{10}/R_9 = 1.2/1.2 = 1$, $R_{12}/R_{11} = 5.6/82 = 0.0683$, $R_7/R_5 = 180/1200 = 0.15$, and $1/R_6C_1 = 1/(18000 \times 1.2 \times 10^{-9}) = 46269$. Because ratio $R_{12}/R_{11}$is very small, the output voltage or

control effort can be approximated by

$$u = K_p e + K_i \int_0^t e dt \tag{2-2}$$

where $K_p = 0.15$ is the proportional gain and $K_i = 46269$ is the integral gain.

(4) Opto-Isolation Module

Figure A2.4 in Appendix A shows the schematic of the opto-isolation circuit. The function of the module is to obtain two outputs that are inverted with each other, which can guarantee that MOSFET's pair (Q_1& Q_3) and (Q_2 & Q_4) in the bridge module do not turn on and off at the same time. Thus, the direction control of the motor current can be realized in this way. There are three opto-isolator circuits. As shown in Figure 2.3 of the overall circuitry, the output B and its ground in opto-isolation circuit (2) are connected to Gate 1 and Source 1 of MOSFET Q_1 respectively. The output A and its ground in opto-isolation circuit (1) are connected to Gate 2 and Source 2 of MOSFET Q_2 respectively. Since MOSFETs Q_3 and Q_4 shares the same point at the source, only one opto-isolation circuit (3) is needed. The output A, output B and their shared ground in opto-isolation circuit (3) are connected to Gate 4 of MOSFET Q_4, the Gate 3 of MOSFET Q_3, and the shared Source S_3 & S_4 of MOSFETs Q_4 and Q_3 respectively. Careful grounding should be considered because the output grounds in three opto-isolation circuits are independent with each other and they do not share the same ground as the common ground in the circuitry. On the other hand, the magnitude of output voltage with respect to its ground must be greater than 10V, because 10V voltage is needed to turn on MOSFETs fully.

$DS0026CN$ is a clock chip which can drive capacitive load at the MOSFET with a peak of one ampere. The opto-isolation chip is HP261A. The opto-isolation circuit must be able to operate at high frequency, the same as the sampling frequency in data acquisition.

Since each of these circuits must be isolated with each other, they require different power supplies. The +5V supply is used for HP261A opto-isolation and +12V for $DS0026CN$.

(5) Signal Separation Module

The schematic is shown in Figure A2.5 of Appendix A. The function of the signal separation circuit is to separate the command voltage from the DAQ board into a magnitude signal and a direction signal. The gain $R_2/R_1 = 1$ and diode D_1 are used to rectify and to obtain the absolute value of the command voltage. The direction output is a binary value. If the input signal is positive, the direction output is zero because of the diode D_2 action; If input signal is negative, the direction output value is

$$V_{dir} = \frac{R_4}{R_3 + R_4} V_+ \tag{2-2}$$

where V_+ is the output voltage of Opamp LM1458.

(6) Power Supply Module

Figure A2.6 in Appendix A shows the schematic of the power supply module. To provide $\pm 12V$ and $+5V$ DC voltages to various chips including opto-isolation chip HP261A, clock chip $DS0026CN$, LM1458 opamps etc., four power supply modules are needed. The circuit consists of a transformer, a diode bridge, voltage regulators, and capacitors.

(7) Sensor Module

The sensor module includes one potentiometer circuit, two strain gauge circuits.

A. Potentiometer Circuit Figure A2.7 in Appendix A shows the schematic of the potentiometer circuit. The circuit is a simple voltage follower. The output voltage $V(t)$ at time instant t can be expressed by

$$V(t) = \frac{(V_1 - V_2)}{L_1 - L_2} x(t) + \frac{V_2 L_1 - V_1 L_2}{L_1 - L_2} \tag{2-3}$$

where V_1 is the voltage reading when the beam is L_1, V_2 is the voltage reading when the beam is L_2, and $x(t)$ is the axial position of the cantilever beam at time instant t.

B. Strain Gauge Circuit Figure A2.8 in appendix shows the schematic of strain gauge circuit. The function of the circuit is to amplify the strain gauge signals. The output $V(t)$ of the circuit is determined by

$$V(t) = \frac{R_7}{R_5}(\frac{R_4}{R_1}V_1 - \frac{R_4}{R_2}V_2) = 100 \times 10(V_1 - V_2) \quad (2\text{-}4)$$

where V_1 is the input from one terminal of the strain gauge sensor and V_2 is the input from the other terminal of the strain gauge sensor.

2.3.2 Testing Results of the Circuitry Board

After the circuits have been set up, they are tested individually. Then, the assembly circuitry is tested. The testing results are presented below.

(1) Testing of the Bridge Module

Figure A2.9 in Appendix A shows the hookup for testing bridge module. The testing was done by measuring the voltage between the gate and source of each MOSFET to make sure that MOSFET's pair (Q_1& Q_3) and pair (Q_2& Q_4) do not turn on and off at the same time. Note that Case 1 is the testing condition for shorting common ground and input direction of one of the opto-isolation modules, and Case 2 is the testing condition for shorting input direction and +5V terminal of the module on the left. The results are shown in Table 2-1.

Table 2-1. Voltage between gate and source of MOSFET

MOSFET's No	Voltage in Case 1(V)	Voltage in Case 2 (V)
Q_1	11.53	0
Q_2	0	10.86
Q_3	11.53	0
Q_4	0	10.86

Meanwhile, the motor current can be read from the Amp meter by adjusting the voltage from voltage source shown in Figure A2.9 of Appendix A. The relationship between the setpoint voltage and the motor current is shown in Figure 2.2.

It is found from testing that

1. MOSFET's pairs do not turn on or off simultaneously.
2. The voltage between the gate and the source of each MOSFET is greater than 10V, which can turn on MOSFET fully.
3. There is nearly linear relationship between the setpoint voltage and the motor current if the setpoint voltage ranges from 0V to 3V. However, the linear relationship does not exist if setpoint voltage is greater than 3V.

(2) Testing of the Motor Power Supply Module

The testing was done by measuring the output voltages 12V, -12V and +5V with respect to their ground. The waveforms of three outputs were displayed on a Fluke scope. The testing diagram is shown in Fig A2.10 of Appendix A.

(3) Testing of the Current Control Module

Figure A2.11 and Figure A2.12 in Appendix A show the hookup for testing the module. The results are shown in Figure 2.4 and Figure 2.5 respectively. It is concluded that P control, I control and PI effort have sensible output waveforms when 1V square waveform is input from function generator. The output of proportional control has a ratio of 0.15 with respect to 1v square input. The integral (I) waveform in Figure 2.4 are almost the same as the proportional (P) and integral (I) waveform shown in Figure 2-5 when 1V square waveform is input to the

circuit, which means that the integral (I) effort dominates control effort.

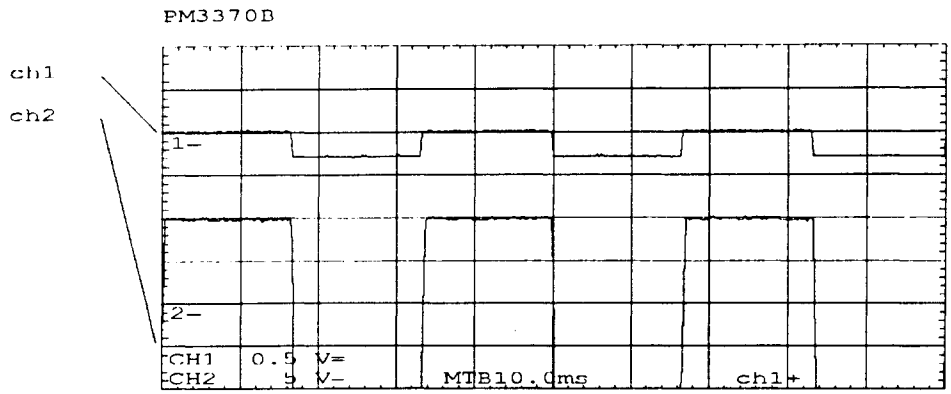

Figure 2.4 The P effort and I effort for 1V square waveform input

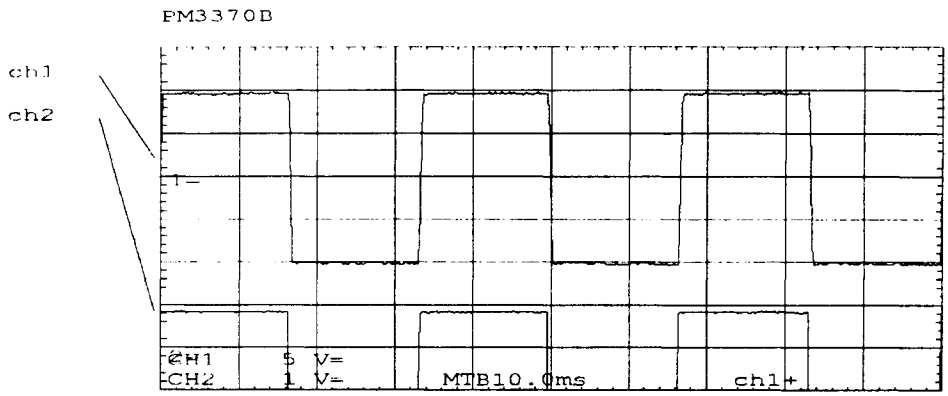

Figure 2.5 The 1V square waveform input and PI effort waveform

(4) Testing of the Opto-Isolation Module

The testing diagram is shown in Figure A2.13 of Appendix A. Figure 2.6 shows that output A is out of phase with the input. Figure 2.7 shows that output B is in phase with the input. Thus, outputs A and B are always inverted with each other so that switching MOSFET pair

can be realized.

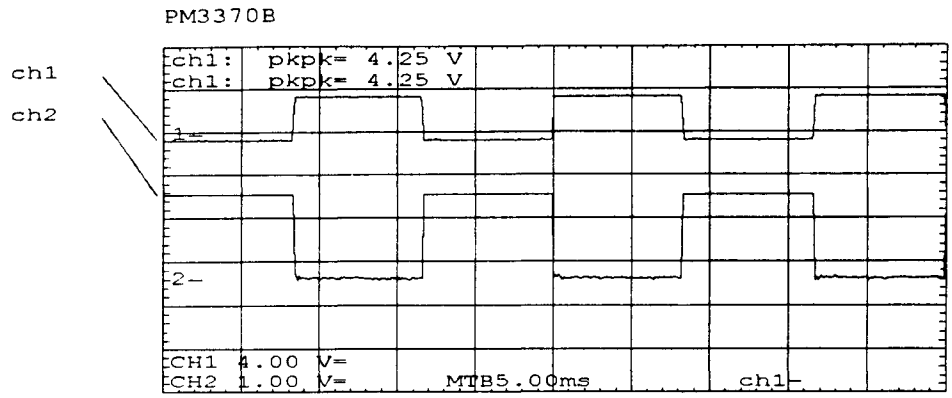

Figure 2.6 Output A and 1V square input waveform

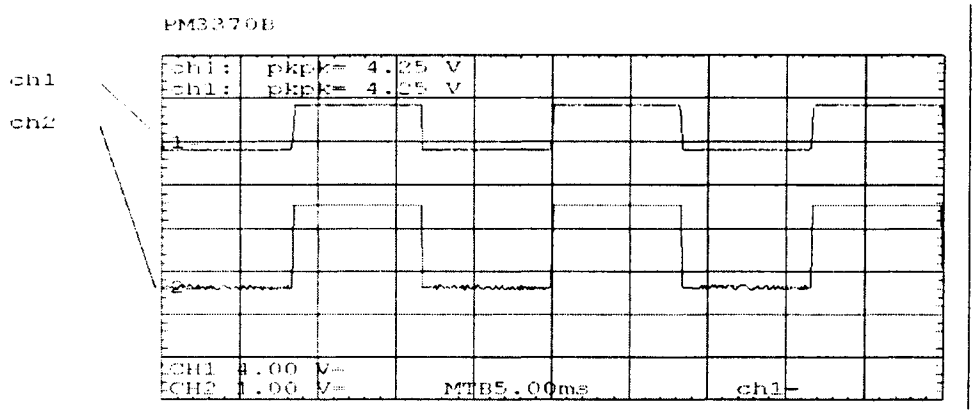

Figure 2.7 Output B and 1V square input waveform

(5) Testing of the Signal Separation Module

Figure A2.14 of Appendix A shows the hookup for testing diagram of the circuit. Figure 2-8 shows the magnitude output and direction output waveforms when a 1V sine waveform with 60Hz frequency from function generator is input to the circuit. It seems that the circuit can behave as expected, i.e., producing a rectified waveform for the magnitude and a square waveform for the direction.

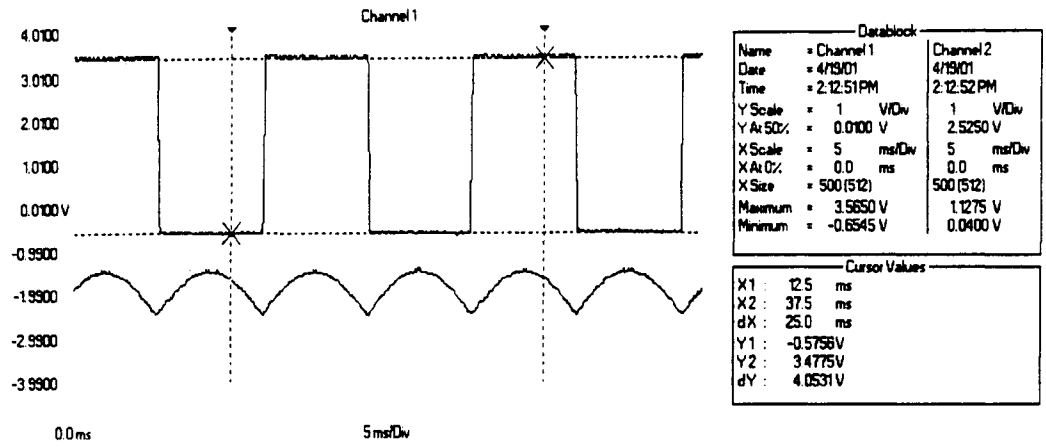

Figure 2.8 Rectified magnitude waveform and square waveform for direction

(6) Testing of the Power Supply Module

The testing method of power supply module is the same as that of testing motor power supply module. It was done by measuring the voltage outputs marked as 12V, -12V and 5V. The waveforms of three outputs were checked using a Fluke scope.

(7) Testing of the Sensor Modules

The experimental results are given as follows:

A. Potentiometer Circuit Figure A2.15 shows testing diagram of potentiometer circuit. By turning the pot, output waveform is shown in Figure 2.9. The result shows that the circuit can change angular position signal into voltage signal properly.

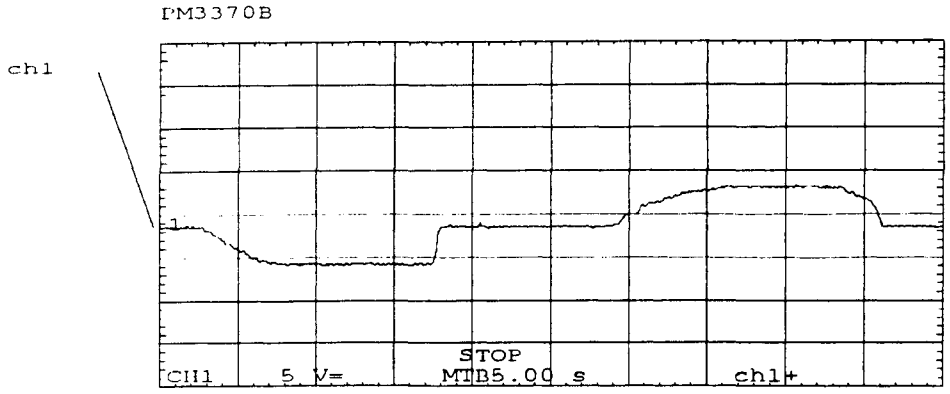

Figure 2.9 Potentiometer output waveform

B. Strain Gauge Circuit The testing diagram of the circuit are shown in Figure A2.16. Figure 2.10 shows strain gauge signals. When the beam was impacted, the amplified strain gauge signals follow the oscillation of the beam, which indicates that the circuit works properly.

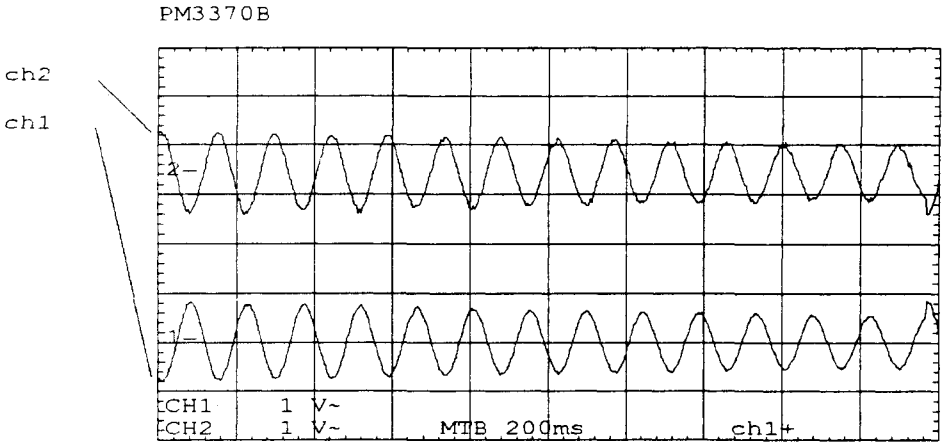

Figure 2.10 The strain gauge signals at two positions

(8) Testing of the Overall Circuitry

The testing diagram of the overall circuit assembly is shown in Figure A2.17. Figure A.2.18 of Appendix A. In the testing, the variable resistor was used as the motor. Figure 2-11 shows the comparison between the setpoint waveform and feedback one. Figure 2-12 shows the comparison between the setpoint waveform and feedback one when magnitude of the setpoint changes.

Figure 2-13 shows the comparison between the setpoint waveform and feedback one when frequency of the setpoint changes. Figure 2-14 shows voltage waveforms of the setpoint and the variable resistor. Figure 2-15 shows that saturation occurs when resistance of the variable resistor and/or amplitude of the setpoint waveforms from function generator increases.

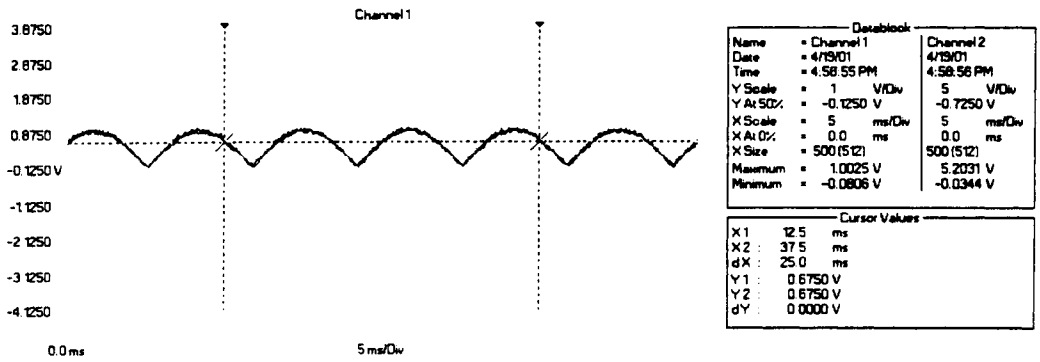

Figure 2.11 Waveform comparison between setpoint and feedback

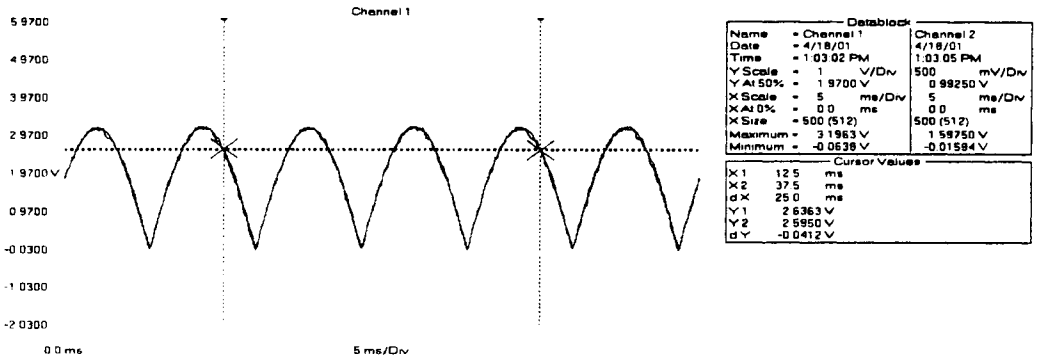

Figure 2.12 Waveform comparison when setpoint amplitude changes

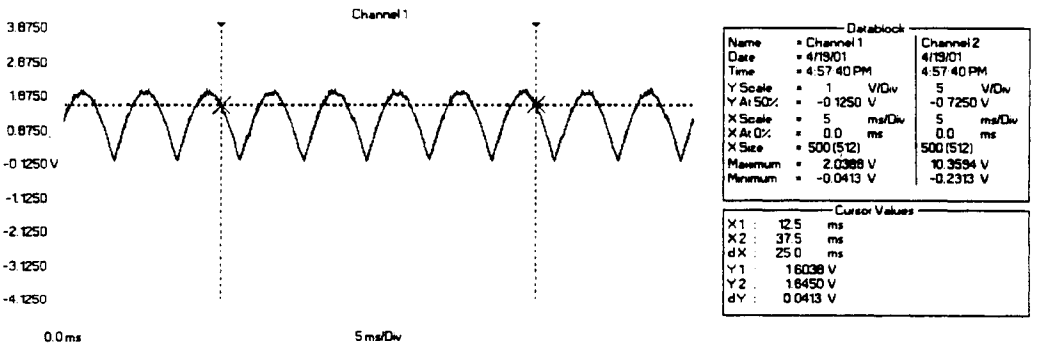

Figure 2.13 Waveform comparison when setpoint frequency changes

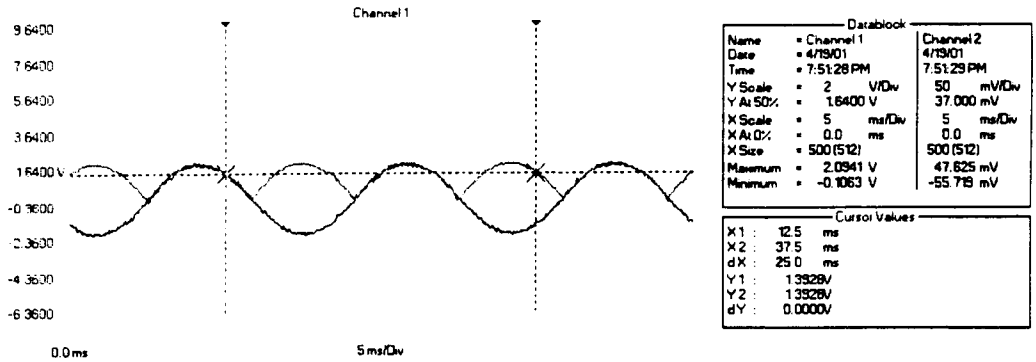

Figure 2.14 The waveforms of the variable resistor and the setpoint

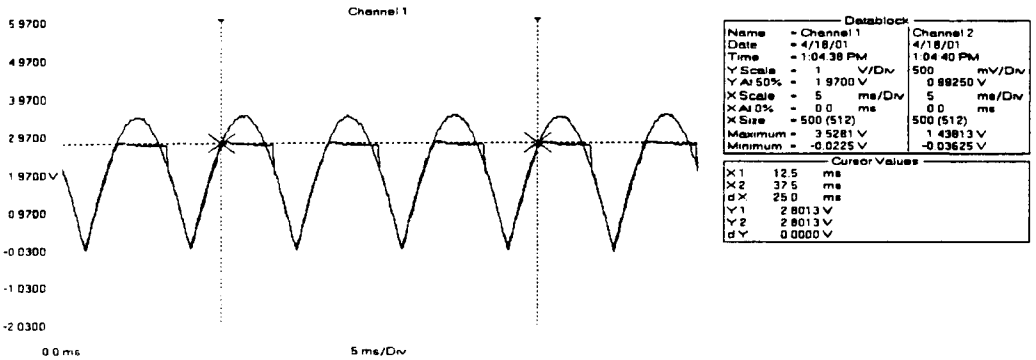

Figure 2.15 High-amplitude setpoint waveform and saturated feedback waveform

It is concluded that the output follows the setpoint no matter how frequency of the setpoint changes and under the condition of small variations of the resistance of the motor and small variations of setpoint amplitudes. However, the output does not follow the setpoint or saturation occurs when the amplitudes of both the resistance of the motor and the setpoint become too high.

2.4 Summary

The circuitry functions properly. It can meet the requirements of controlling the mangitude and direction of the motor current and amplifying the sensor signals. The testing method is useful in maintenance and troubleshooting for the circuitry. A valuable experience has been obtained from the building and testing of the circuitry.

Chapter 3

Dynamics of an Axially-Moving Cantilever Beam

The second objective of the present work is to develop an analytical model to study the dynamics of an axially-moving cantilever beam. First, the dynamics of a fixed-length cantilever beam is briefly reviewed. Then, a state-space model is derived for a cantilever beam engaged in axial motion. The model is time-varying as the system matrix, input matrix, output matrix and direct transmission matrix are all functions of time when the beam is axially moving. As an analytical solution of the model is not possible, a computer simulation is conducted. The simulation results are given acccordingly to show how the axial motion of the cantilever beam influences the dynamics of the system, including transient responses, "frozen" modal parameters, and "pseudo" modal parameters.

The chapter is organized as follows: Section 3.1 reviews the dynamics of the fixed-length cantilever beam, Section 3.2 describes the modeling of the axially-moving cantilever beam, Section 3.3 shows the computer simulation results, Section 3.4 discusses the evaluation of varying discrete-time transition matrix and "pseudo" modal parameters, and Section 3.5 is a brief summary.

3.1 Dynamics of the Fixed-Length Cantilever Beam

3.1.1 Mathematical Modeling

A schematic diagram of a fixed-length cantilever beam is shown in Figure 3.1.1.

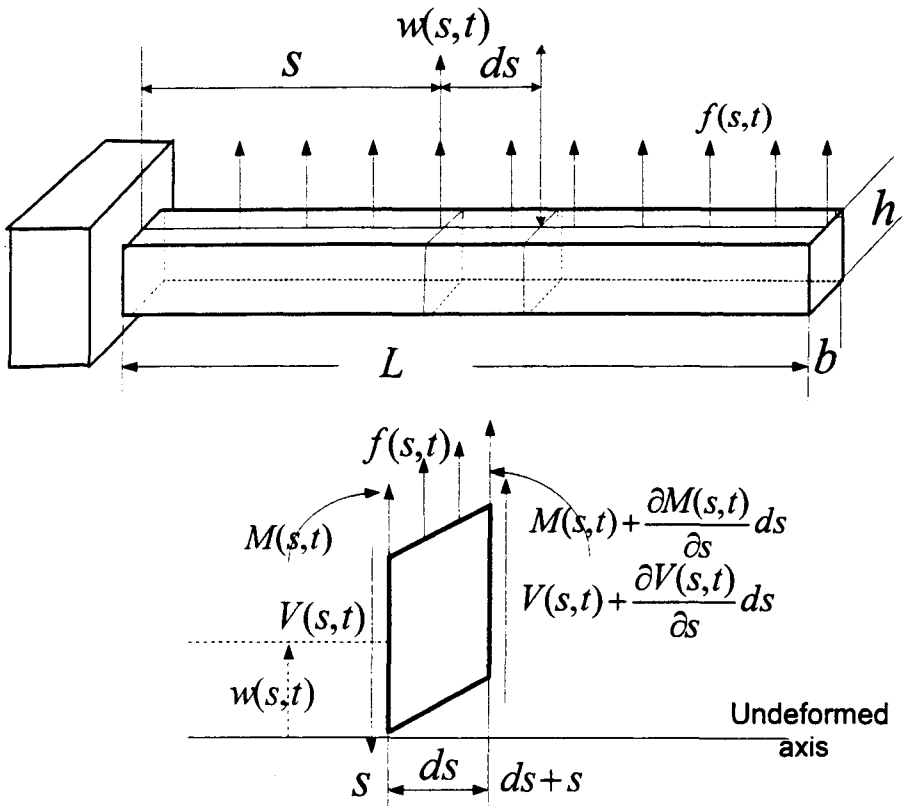

Figure 3.3.1 Lateral vibration of the cantilever beam and a free-body diagram of the beam element

To simplify the problem, the following assumptions are made:

(1) The beam is uniform along its longitudinal direction, both in mass distribution and elastic properties.

(2) Rotary inertia and shear deformation can be neglected.

(3) The beam is composed of a linear, homogeneous, isotropic, elastic material without axial load such that plane sections remain plane and the plane of symmetry of the beam is also the plane of vibration so that rotation and translation are decoupled.

The beam that satisfies the above assumptions is referred to as the Euler-Bernoulli beam.

If a physical damping γ (kg/m.s) exists in the system, a partial differential equation governing the motion of the beam element is given as [28]

$$m\frac{\partial^2 w(s,t)}{\partial t^2} + \gamma\frac{\partial w(s,t)}{\partial t} + EI\frac{\partial^4 w(s,t)}{\partial s^4} = f(s,t) \tag{3-1-1}$$

where m (kg/m) is the length density of the beam, or $m = \rho A_b$, A_b (m^2) is the cross-section area of the beam, ρ (kg/m^3) is the density of the beam material, E (N/m^2) is Young's modulus of elasticity for the beam, I (m^4) is the moment of inertia for the cross-sectional area, and $f(s,t)$ (N/m) is the applied external force per unit length of the beam.

To transform the partial differential equation (3-1-1) into a set of ordinary differential equations, it is assumed that the deflection $w(s,t)$ can be expressed as

$$w(s,t) = \Phi(s)q(t) = \sum_{j=1}^{n} \Phi_j(s)q_j(t) \tag{3-1-2}$$

where $q(t) = [q_1(t) \quad q_2(t) \quad \ldots \quad q_n(t)]^T$ is a column vector of the generalized coordinates, $\Phi(s) = [\Phi_1(s) \quad \Phi_2(s) \quad \ldots \quad \Phi_n(s)]$ is a row vector of mode shape functions, and n is the number of the vibratory modes considered.

The mode shape function is expressed as

$$\Phi_j(s) = \cosh(\beta_j s) - \cos(\beta_j s) - \sigma_j(\sinh(\beta_j s) - \sin(\beta_j s)) \tag{3-1-3}$$

where $\sigma_j = [\sinh(\beta_j L) - \sin(\beta_j L)] \,/\, [\cosh(\beta_j L) + \cos(\beta_j L)]$ [28]. The values of the constants $\beta_j L$ and σ_j for the first four modes are listed in Table 3.1.

Table 3.1 $\beta_j L$ and σ_j of the first four modes

mode $\mathcal{N}o$	1	2	3	4
$\beta_j L$	1.8751	4.69409	7.8547	10.9955
σ_j	0.7341	1.0185	0.9992	1.0000

The natural frequency of the jth mode is given as

$$f_j = \frac{1}{2\pi}\left(\frac{(\beta_j L)}{L}\right)^2 \sqrt{\frac{EI}{\rho A}}. \tag{3-1-4}$$

3.1.2 Response to a Concentrated Force

If a concentrated force $F(t)$ is applied at s_{in}, $f(s,t)$ can be expressed by

$$f(s,t) = F(t)\delta(s - s_{in}) \tag{3-1-5}$$

where $\delta(s - s_{in})$ is a Dirac Delta function.

Substituting equation (3-1-2) and (3-1-5) into equation (3-1-1) results in

$$m\Phi(s)\,\ddot{q}\,(t) + \gamma\Phi(s)\,\dot{q}\,(t) + EI\Phi''''(s)q(t) = F(t)\delta(s - s_{in}) \tag{3-1-6}$$

where dots denote derivatives with respect to time t and primes derivatives with respect to s, or

$$\ddot{q}\,(t) = \frac{\partial^2 q(t)}{\partial t^2} \quad \dot{q}\,(t) = \frac{\partial q(t)}{\partial t} \quad \Phi''''(s) = \frac{\partial^4 \Phi(s)}{\partial s^4}$$

Premultiplying the above equation by $\Phi^T(s)$ and integrating it with respect to s from 0 to L results in

$$\int_0^L \Phi^T\Phi ds\,\ddot{q}\,(t) + \frac{\gamma}{m}\int_0^L \Phi^T\Phi ds\,\dot{q}\,(t) + \frac{EI}{m}\int_0^L \Phi^T\Phi''''ds\;q(t) = \frac{F(t)}{m}\int_0^L \Phi^T\delta(s - s_{in})ds.$$

Using the orthogonality of the mode shape functions, the following relations exist

$$\int_0^L \Phi^T\Phi ds = \mathbf{I} \quad \text{and} \quad \mathbf{\Lambda} = \int_0^L \Phi^T\Phi''''ds = \mathbf{diag}\,[(\beta_1 L)^4, (\beta_2 L)^4, ..., (\beta_n L)^4] \tag{3-1-7}$$

where $\mathbf{I}$ is an $n \times n$ identity matrix and $\mathbf{\Lambda}$ an $n \times n$ diagonal matrix.

Equation (3-1-6) becomes

$$\ddot{q}\,(t) + \frac{\gamma}{m}\mathbf{I}\,\dot{q}\,(t) + \frac{EI}{m}\mathbf{\Lambda}q(t) = \frac{\Phi^T(s_{in})}{m}F(t). \tag{3-1-8}$$

The above equation can be rewritten into a state-space representation

$$\dot{x}\,(t) = Ax(t) + Bu(t) \tag{3-1-9}$$

where the state vector is

$$x(t) = \begin{bmatrix} q(t) \\ \dot{q}\,(t) \end{bmatrix}, \tag{3-1-10}$$

the system matrix is

$$A = \begin{bmatrix} \mathbf{0}_{n\times n} & \mathbf{I} \\ -(\frac{EI}{m})\mathbf{\Lambda} & -\frac{\gamma}{m}\mathbf{I} \end{bmatrix}, \tag{3-1-11}$$

and the input matrix is

$$B = \begin{bmatrix} \mathbf{0}_{n\times 1} \\ \frac{1}{m}\Phi^T(s_{in}) \end{bmatrix}, \tag{3-1-12}$$

and the input

$$u(t) = F(t). \tag{3-1-13}$$

Here the convention $\mathbf{0}_{i\times j}$ is adopted to denote an $i \times j$ matrix of zeros.

It is noted that the number of state variables is $n_x = 2n$. Several different responses or outputs can be obtained, depending upon the means of measurement. If a strain gauge sensor located at s_{out} is used, the output will be a voltage signal proportional to the magnitude of the strain at s_{out}. In this case, the output is given as

$$y = K_{sg}\Phi''(s_{out})q(t) \tag{3-1-14}$$

where K_{sg} is the gain of the strain gauge measurement system. If the deflection at s_{out} can be measured, the output is

$$y = K_d\Phi(s_{out})q(t) \tag{3-1-15}$$

where K_d is the gain of the deflection measurement system. If the velocity at s_{out} can be measured, the output is

$$y = K_v\,\dot{w}\,(s_{out},t) = K_v\Phi(s_{out})\,\dot{q}\,(t) \tag{3-1-16}$$

where K_v is the gain of the velocity measurement system. If the acceleration at s_{out} can be measured, the output is

$$y = K_a \ddot{w}(s_{out}, t) = K_a \Phi(s_{out}) \ddot{q}(t) \tag{3-1-17}$$

where K_a is the gain of the acceleration measurement system.

Substituting $\ddot{q}(t)$ solved from equation (3-1-8) into equation (3-1-17) results in

$$y = K_a \left[-\frac{EI}{m} \Phi(s_{out}) \Lambda q(t) - \frac{\gamma}{m} \Phi(s_{out}) \mathbf{I} \dot{q}(t) + \frac{1}{m} \Phi(s_{out}) \Phi^T(s_{in}) F(t) \right]. \tag{3-1-18}$$

In general, the output vector is expressed as

$$y = Cx + Du \tag{3-1-19}$$

where C is the output matrix and D is the direct transmission matrix. For example, the use of a strain sensor at s_{out1}, a displacement sensor at s_{out2}, a velocity sensor at s_{out3} and an accelerometer at s_{out4} results in

$$C = \begin{bmatrix} K_{sg} \Phi''(s_{out1}) & \mathbf{0}_{1\times n} \\ K_d \Phi(s_{out2}) & \mathbf{0}_{1\times n} \\ \mathbf{0}_{1\times n} & K_v \Phi(s_{out3}) \\ -K_a \frac{EI}{m} \Phi(s_{out4}) \Lambda & -K_a \frac{\gamma}{m} \Phi(s_{out4}) \mathbf{I} \end{bmatrix} \tag{3-1-20}$$

and

$$D = \begin{bmatrix} 0 \\ 0 \\ 0 \\ K_a \frac{1}{m} \Phi(s_{out4}) \Phi^T(s_{in}) \end{bmatrix}. \tag{3-1-19}$$

3.1.3 Observability and Controllability of the System

The controllability matrix of the system with the system order n_x is given by [36, 37]

$$Q = \begin{bmatrix} B & AB & A^2B & . & . & A^{n_x-1}B \end{bmatrix}. \tag{3-1-20}$$

The system is controllable if the matrix Q has full rank, i.e., rank[Q] = n_x.

The observability matrix of the system with the system order n_x is given by [36, 37]

$$P = \begin{bmatrix} C \\ CA \\ CA^2 \\ . \\ . \\ CA^{n_x-1} \end{bmatrix}. \tag{3-1-21}$$

The system is observable if the matrix P has full rank, i.e., rank[P] = n_x.

To understand these two important matrices, it is assumed that the system is excited by a concentrated force at s_{in} and two strain gauge outputs are observed at s_{out1} and s_{out2} positions, respectively. The Q and P matrices are given by

$$Q = \frac{1}{m}\begin{bmatrix} 0_{n\times 1} & \Phi^T(s_{in}) & \Phi^T(s_{in}) & . & . & \Phi^T(s_{in}) \\ \Phi^T(s_{in}) & -\frac{\gamma}{m}\Phi^T(s_{in}) & (-\frac{\gamma}{m})^2\Phi^T(s_{in}) & . & . & (-\frac{\gamma}{m})^{n_x-1}\Phi^T(s_{in}) \end{bmatrix} \tag{3-1-22}$$

and

$$P = \begin{bmatrix} K_{sg}\Phi''(s_{out1}) & 0_{1\times n} \\ K_{sg}\Phi''(s_{out2}) & 0_{1\times n} \\ 0_{1\times n} & K_{sg}\Phi''(s_{out1}) \\ 0_{1\times n} & K_{sg}\Phi''(s_{out2}) \\ . & . \\ . & . \\ 0_{1\times n} & K_{sg}\Phi''(s_{out1}) \\ 0_{1\times n} & K_{sg}\Phi''(s_{out2}) \end{bmatrix}. \tag{3-1-23}$$

The controllability depends on the mode shape function values at s_{in}, and the observability depends on the values of the second derivatives of the mode shape functions at s_{out1} and s_{out2}.

Figure 3.1.2 shows the first three mode shape functions. It can be seen that if the force is applied at one of the node points, such as $s/L = 0.5, 0.755$ or 0.864 where the mode shape

functions become zero, the system is uncontrollable.

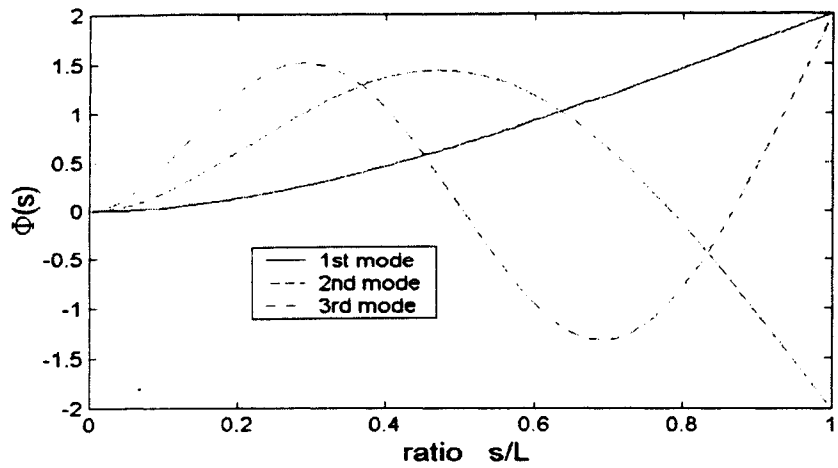

Figure 3.1.2 The first three mode shape functions

Figure 3.1.3 shows the second derivatives of the mode shape functions. It is noted that to ensure the system to be observable, the strain gauge sensors cannot be placed at the location where $\Phi_i''(s_{out})$ is zero.

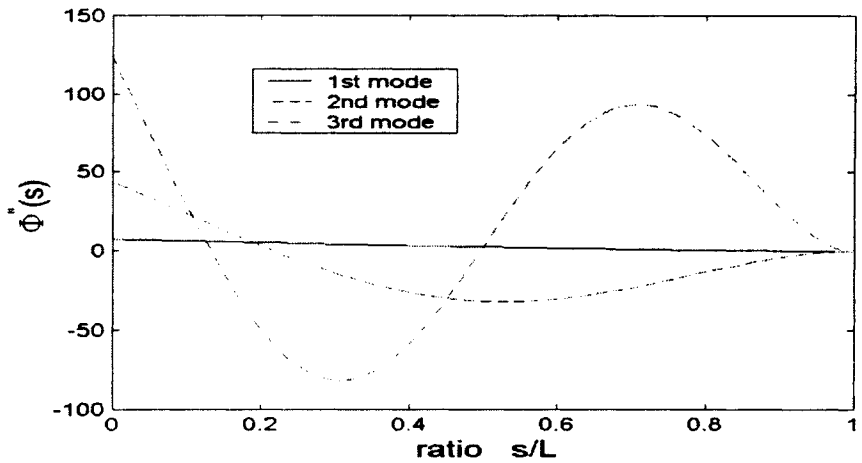

Figure 3.1.3 The second derivatives of the first three mode shape functions

3.2 Modeling of an Axially Moving Cantilever Beam

The apparatus of the axially-moving cantilever beam is shown in Figure 3.2.1.

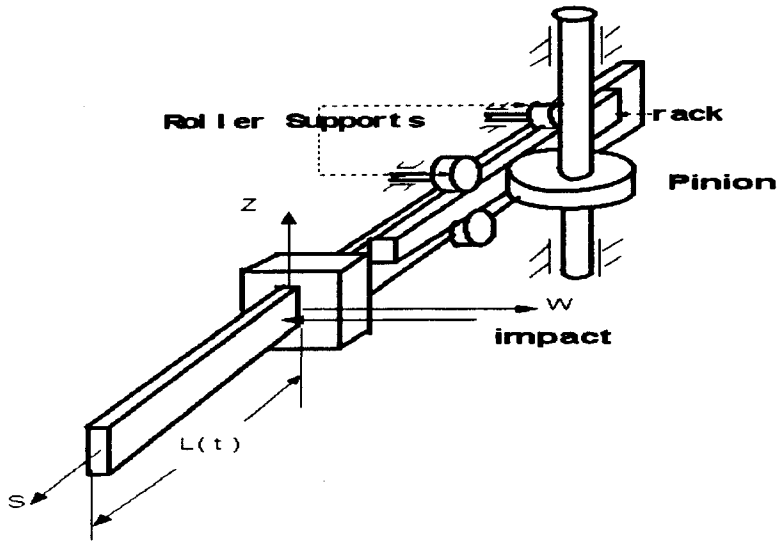

Figure 3.2.1 The apparatus of the axially-moving cantilever beam

It is noted that the lateral motion takes place on the horizontal plane such that gravity has little effect on the motion. The beam is assumed to be an Euler-Bernoulli beam. In addition, it is assumed that the axial motion of the beam is a function of time only.

Two modeling cases are considered: case one includes the contribution of the axial force to the lateral vibration of the beam and case two does not. Each case is further divided into two subcases. Subcase one considers the physical damping and subcase two does not.

3.2.1 Modeling: the Contribution of the Axial Force Considered

The following development is based on the work presented in [4]. Figure 3.2.2 (a) shows the beam that is laterally deflected by $w(s,t)$. Figure 3.2.2 (b) shows the free-body diagram of a beam element Δs and Figure 3.2.2 (c) shows the remaining part of the beam, where V and M are the shear force and bending moment respectively, T is the axial force acting on the beam element Δs at s perpendicular to the face of the cross section, T_1 is the axial force acting at the beam section at $(s+\Delta s)$, $\theta = \partial w/\partial x$ is the slope of the beam with respect to the undeformed

elastic axis.

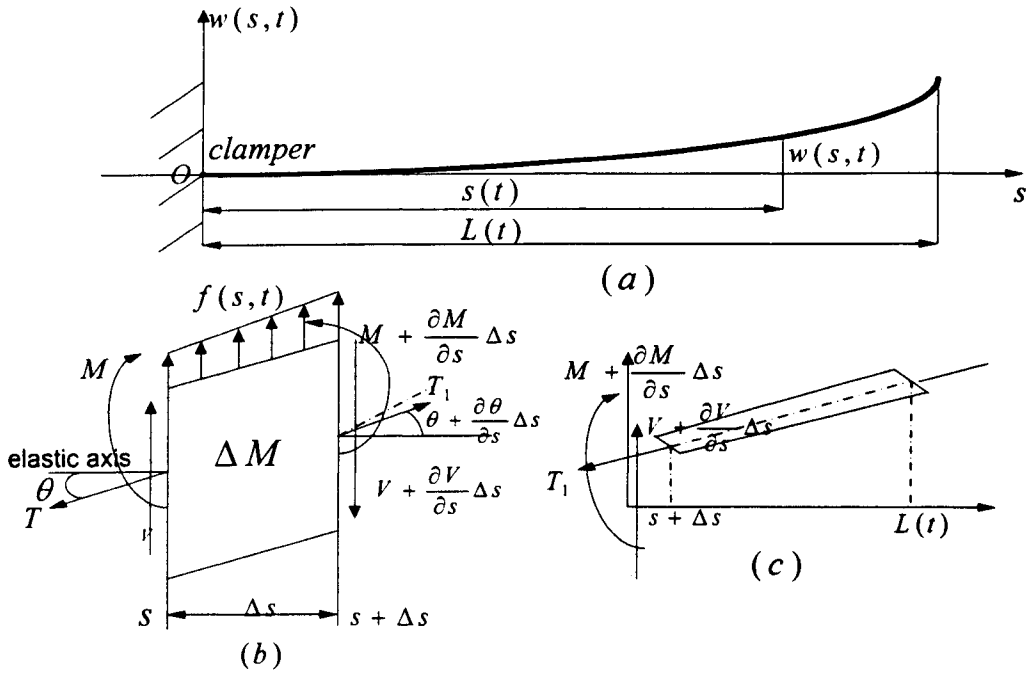

Figure 3.2.2 (a) deformaion; (b) free-body diagram of Δs; (c) remaining part of the beam

Applying Newton's second law to the element Δs in the lateral direction gives

$$m\Delta s\frac{d^2w(s,t)}{dt^2} = V - (V + \frac{\partial V}{\partial s}\Delta s) + T_1\sin(\theta + \frac{\partial \theta}{\partial s}\Delta s) - T\sin\theta + f(s,t)\Delta s. \qquad (3\text{-}2\text{-}1\text{-}1)$$

It is assumed that $\theta, \partial\theta/\partial s$, and Δs are very small,

$$\sin(\theta + \frac{\partial \theta}{\partial s}\Delta s) \approx (\theta + \frac{\partial \theta}{\partial s}\Delta s) \quad \text{and} \quad \sin\theta \approx \theta.$$

Equation (3-2-1-1) can be changed into

$$m\Delta s\frac{d^2w(s,t)}{dt^2} = -\frac{\partial V}{\partial s}\Delta s + (T_1 - T)\theta + T_1\frac{\partial \theta}{\partial s}\Delta s + f(s,t)\Delta s. \qquad (3\text{-}2\text{-}1\text{-}2)$$

Applying Newton's second law to the element Δs in the axial direction gives

$$m\Delta s\,\ddot{L} = T_1 - T. \qquad (3\text{-}2\text{-}1\text{-}3)$$

If the rotatory inertia can be neglected, the summation of the moments induced by all external forces and moment about any point equals zero, i.e.,

$$(M + \frac{\partial M}{\partial s}\Delta s) - M - V\Delta s = 0 \quad \text{or} \quad V = \frac{\partial M}{\partial s}. \tag{3-2-1-4}$$

Applying Newton's second law to the remaining beam $(L - s)$ in the axial direction gives

$$\rho A(L - s)\ \ddot{L} = -T_1. \tag{3-2-1-5}$$

It is noted that

$$M = EI\frac{\partial^2 w}{\partial s^2} \quad \text{and} \quad \theta = \frac{\partial w}{\partial s} \tag{3-2-1-6}$$

where EI is the flexural rigidity of the beam.

Substituting equations (3-2-1-3), (3-2-1-4), (3-2-1-5), and (3-2-1-6) into equation (3-2-1-2) gives

$$m\Delta s\frac{d^2w(s,t)}{dt^2} = -EI\frac{\partial^4 w(s,t)}{\partial s^4}\Delta s + m\Delta s\ \ddot{L}\ \frac{\partial w}{\partial s} - m(L - s)\ \ddot{L}\ \frac{\partial^2 w}{\partial s^2}\Delta s + f(s,t)\Delta s.$$

Thus, the dynamic model, when damping is neglected, is expressed as

$$\frac{d^2w(s,t)}{dt^2} + \frac{EI}{m}\frac{\partial^4 w(s,t)}{\partial s^4} - \ddot{L}\ \frac{\partial w}{\partial s} + (L - s)\ \ddot{L}\ \frac{\partial^2 w}{\partial s^2} = \frac{f(s,t)}{m}. \tag{3-2-1-7}$$

If the system damping γ $(kg/m.s)$ is considered, the vibration equation in lateral direction is given as

$$\frac{d^2w(s,t)}{dt^2} + \frac{\gamma}{m}\frac{dw(s,t)}{dt} + \frac{EI}{m}\frac{\partial^4 w(s,t)}{\partial s^4} - \ddot{L}\ \frac{\partial w}{\partial s} + (L - s)\ \ddot{L}\ \frac{\partial^2 w}{\partial s^2} = \frac{f(s,t)}{m}. \tag{3-2-1-8}$$

To transform the above partial differential equation into a set of ordinary differential equations, let

$$s = \alpha L \quad 0 \leq \alpha \leq 1. \tag{3-2-1-9}$$

Thus, the mode shape functions in terms of equation (3-1-3) becomes

$$\Phi_j(\alpha) = \cosh(\beta_j L\alpha) - \cos(\beta_j L\alpha) - \sigma_j(\sinh(\beta_j L\alpha) - \sin(\beta_j L\alpha))$$

and the value $\beta_j L$ and σ_j are given in Table 3.1.

Now the beam deflection becomes

$$w(\alpha,t) = \sum_{j=1}^{n} \Phi_j(\alpha) q_j(t) = \Phi(\alpha) q(t) \qquad \text{(3-2-1-10)}$$

where $\Phi(\alpha) = [\Phi_1(\alpha) \quad \Phi_2(\alpha) \ldots \quad \Phi_n(\alpha)]$ is the row vector of the mode shape functions in terms of α .

The following relations exist

$$\begin{aligned}
\frac{dw(s,t)}{dt} &= \Phi(\alpha)\,\dot{q}\,(t) + \Phi'(\alpha) q(t)\,\dot{\alpha} \\
\frac{d^2w(s,t)}{dt^2} &= \frac{d}{dt}\left(\Phi(\alpha)\,\dot{q}\,(t) + \Phi'(\alpha) q(t)\,\dot{\alpha}\right) \\
&= \Phi(\alpha)\,\ddot{q}\,(t) + 2\Phi'(\alpha)\,\dot{q}\,(t)\,\dot{\alpha} + \Phi''(\alpha) q(t)\,\dot{\alpha}^2 + \Phi'(\alpha) q(t)\,\ddot{\alpha} \\
\dot{\alpha} &= \frac{\dot{L}}{L}(1-\alpha) \qquad \text{(3-2-1-11)} \\
\ddot{\alpha} &= (1-\alpha)\left(\frac{\ddot{L}}{L} - 2\frac{\dot{L}^2}{L^2}\right)
\end{aligned}$$

where dots denote derivatives with respect to time t and primes represent derivatives with respect to variable α.

Assume that the force acting laterally $F(t)$ is concentrated at $s_{in} = \alpha_{in} L$

$$f(s,t) = F(t)\delta(\alpha - \alpha_{in}) \qquad \text{(3-2-1-12)}$$

where $\delta(\alpha - \alpha_{in})$ is a Dirac Delta function. It is noted that s_{in} is the axial distance between the concentrated force and the clamp (see Figures 3.2.1 and 3.2.2) and it is a function of time. The following relation exists

$$s_{in} + r_{in} = L \qquad \text{(3-2-1-13)}$$

where r_{in} is a constant axial distance between the concentrated force and the tip of the beam. Thus, the variable α_{in} can be expressed as

$$\alpha_{in} = 1 - \frac{r_{in}}{L}. \tag{3-2-1-14}$$

Substituting equations (3-2-1-11), (3-2-1-12), (3-2-1-13) into equation (3-2-1-8) , and rearranging results in

$$\Phi(\alpha)\,\ddot{q}\,(t) + \left[2\frac{\dot{L}}{L}(1-\alpha)\Phi^{'}(\alpha) + \frac{\gamma}{m}\Phi(\alpha)\right]\dot{q}\,(t) + \left[\frac{\dot{L}^{2}}{L^{2}}(1-\alpha)^{2} + (1-\alpha)\frac{\ddot{L}}{L}\Phi^{''}(\alpha)\right]q(t) +$$

$$\frac{EI}{mL^{4}}\Phi^{''''}(\alpha)q(t) + \left[(1-\alpha)(\frac{\ddot{L}}{L} - 2\frac{\dot{L}^{2}}{L^{2}} + \frac{\gamma}{m}\frac{\dot{L}}{L}) - \frac{\ddot{L}}{L}\right]\Phi^{'}(\alpha)q(t) = \frac{F(t)\delta(\alpha-\alpha_{in})}{m}\ . \tag{3-2-1-15}$$

Premultiplying both sides of the above equation by term $\Phi^{T}(\alpha)$ and integrating it from 0 to 1 with respect to the variable α results in

$$A_1\,\ddot{q}\,(t) + (\frac{2\,\dot{L}}{L}A_2 + \frac{\gamma}{m}A_1)\,\dot{q}\,(t) +$$

$$\left[(\frac{\ddot{L}}{L} - 2\frac{\dot{L}^{2}}{L^{2}} + \frac{\gamma}{m}\frac{\dot{L}}{L})A_2 - \frac{\ddot{L}}{L}A_3 + \frac{\dot{L}^{2}}{L^{2}}A_4 + \frac{\ddot{L}}{L}A_5 + \frac{EI}{mL^{4}}A_6\right]q(t) = \frac{F(t)}{m}A_7 \tag{3-2-1-16}$$

where

$$\begin{aligned}
A_1 &= \int_0^1 \Phi^{T}(\alpha)\Phi(\alpha)d\alpha & A_2 &= \int_0^1 (1-\alpha)\Phi^{T}(\alpha)\Phi^{'}(\alpha)d\alpha \\
A_3 &= \int_0^1 \Phi^{T}(\alpha)\Phi^{'}(\alpha)d\alpha & A_4 &= \int_0^1 (1-\alpha)^{2}\Phi^{T}(\alpha)\Phi^{''}(\alpha)d\alpha \\
A_5 &= \int_0^1 (1-\alpha)\Phi^{T}(\alpha)\Phi^{''}(\alpha)d\alpha & A_6 &= \int_0^1 \Phi^{T}(\alpha)\Phi^{''''}(\alpha)d\alpha \\
A_7 &= \int_0^1 \Phi^{T}(\alpha)\delta(\alpha-\alpha_{in})d\alpha = \Phi^{T}(\alpha_{in})\ .
\end{aligned} \tag{3-2-1-17}$$

Using the orthogonality of the mode shape functions $\Phi(\alpha)$, it can be proven that

$$A_1 = \mathbf{I} \qquad A_6 = \mathbf{diag}\ \left[(\beta_1 L)^4 \cdots (\beta_n L)^4\right].$$

A compact form of equation (3-2-1-16) is given

$$\ddot{q}(t) + D_d(t)\,\dot{q}(t) + K(t)q(t) = B_1(t)u(t) \qquad \text{(3-2-1-18)}$$

where the time-varying parameter matrices $D_d(t)$, $B_1(t)$ and $K(t)$ are defined as

$$\begin{aligned} D_d(t) &= \frac{2\dot{L}}{L}A_2 + \frac{\gamma}{m}A_1 \qquad B_1(t) = \frac{1}{m}\Phi^T(\alpha_{in}) \\ K(t) &= (\frac{\ddot{L}}{L} - 2\frac{\dot{L}^2}{L^2} + \frac{\gamma}{m}\frac{\dot{L}}{L})A_2 - \frac{\ddot{L}}{L}A_3 + \frac{\dot{L}^2}{L^2}A_4 + \frac{\ddot{L}}{L}A_5 + \frac{EI}{mL^4}A_6\ . \end{aligned} \qquad \text{(3-2-1-19)}$$

If the system is free of damping, the $D_d(t)$ and $K(t)$ matrices become

$$D_d(t) = \frac{2\dot{L}}{L}A_2 \quad K(t) = (\frac{\ddot{L}}{L} - 2\frac{\dot{L}^2}{L^2})A_2 - \frac{\ddot{L}}{L}A_3 + \frac{\dot{L}^2}{L^2}A_4 + \frac{\ddot{L}}{L}A_5 + \frac{EI}{\rho AL^4}A_6\ . \qquad \text{(3-2-1-20)}$$

3.2.2 Modeling: the Contribution of the Axial Force Neglected

If the effect of the axial force is not considered, the lateral motion of the system is expressed as follows (see equation 3-2-1-7)

$$\frac{d^2w(s,t)}{dt^2} + \frac{\gamma}{m}\frac{dw(s,t)}{dt} + \frac{EI}{m}\frac{\partial^4 w(s,t)}{\partial s^4} = \frac{f(s,t)}{m}\ . \qquad \text{(3-2-2-1)}$$

The same equation as equation (3-2-1-18) is derived using the same procedure mentioned above. However the $D_d(t), B_1(t)$ and $K(t)$ parameter matrices are different, as shown in the following

$$\begin{aligned} D_d(t) &= \frac{2\dot{L}}{L}A_2 + \frac{\gamma}{m}A_1 \qquad B_1(t) = \frac{1}{m}\Phi^T(\alpha_{in}) \\ K(t) &= (\frac{\ddot{L}}{L} - 2\frac{\dot{L}^2}{L^2} + \frac{\gamma}{m}\frac{\dot{L}}{L})A_2 + \frac{\dot{L}^2}{L^2}A_4 + \frac{EI}{mL^4}A_6\ . \end{aligned} \qquad \text{(3-2-2-2)}$$

If the system is free of damping, the $D_d(t)$ and $K(t)$ matrices become

$$D_d(t) = \frac{2\dot{L}}{L}A_2 \quad K(t) = (\frac{\ddot{L}}{L} - 2\frac{\dot{L}^2}{L^2})A_2 + \frac{\dot{L}^2}{L^2}A_4 + \frac{EI}{mL^4}A_6\ . \qquad \text{(3-2-2-3)}$$

3.2.3 Continuous-Time State Space Representation of the System

Let $F(t) = u(t)$. The state space representation can be obtained from equation (3-2-1-18) as follows

$$\dot{x}\,(t) = A(t)x(t) + B(t)u(t) \tag{3-2-3-1}$$

where

$$A(t) = \begin{bmatrix} \mathbf{0}_{n\times n} & \mathbf{I} \\ -K(t) & -D_d(t) \end{bmatrix} \qquad B(t) = \begin{bmatrix} \mathbf{0}_{n\times 1} \\ B_1(t) \end{bmatrix}.$$

and $x(t) = [q^T(t) \quad \dot{q}^T(t)]^T$ is the state variable vector.

The output signals depend on the means of measurements. If a strain gauge sensor located at $s_{out} = \alpha_{out}L$ is used, the output is a voltage signal proportional to the magnitude of the strain:

$$y(t) = K_{sg}\Phi''(\alpha_{out})q(t)/L^2 = \begin{bmatrix} K_{sg}\Phi''(\alpha_{out})/L^2 & \mathbf{0}_{1\times n} \end{bmatrix} \begin{bmatrix} q(t) \\ \dot{q}\,(t) \end{bmatrix}. \tag{3-2-3-2}$$

If a deflection sensor located at $s_{out} = \alpha_{out}L$ is used, the output is a voltage signal proportional to the magnitude of the deflection:

$$y(t) = K_d\Phi(\alpha_{out})q(t) = \begin{bmatrix} K_d\Phi(\alpha_{out}) & \mathbf{0}_{1\times n} \end{bmatrix} \begin{bmatrix} q(t) \\ \dot{q}\,(t) \end{bmatrix}. \tag{3-2-3-3}$$

If a velocity sensor located at $s_{out} = \alpha_{out}L$ is used, the output is a voltage signal proportional to the magnitude of the velocity:

$$\begin{aligned} y(t) &= K_v \left[\Phi'(\alpha_{out})\frac{\dot{L}}{L}(1-\alpha_{out})q(t) + \Phi(\alpha_{out})\,\dot{q}\,(t) \right] \\ &= K_v \begin{bmatrix} \Phi'(\alpha_{out})\frac{\dot{L}}{L}(1-\alpha_{out}) & \Phi(\alpha_{out}) \end{bmatrix} \begin{bmatrix} q(t) \\ \dot{q}\,(t) \end{bmatrix}. \end{aligned} \tag{3-2-3-4}$$

If an acceleration sensor located at $s_{out} = \alpha_{out}L$ is used, the output is voltage signal proportional to the magnitude of the acceleration. Using the equation (3-2-1-11), the aceleration output is

expressed as

$$y(t) = \frac{d^2w(s,t)}{dt^2} = \Phi(\alpha)\,\ddot{q}\,(t) + 2\Phi^{'}(\alpha)\,\dot{q}\,(t)\,\dot{\alpha} + \Phi^{''}(\alpha)q(t)\,\dot{\alpha}^2 + \Phi^{'}(\alpha)q(t)\,\ddot{\alpha} \qquad (3\text{-}2\text{-}3\text{-}5)$$

Substituting $\dot{\alpha}$ and $\ddot{\alpha}$ in equation (3-2-1-11) and $\ddot{q}\,(t)$ solved from equantion (3-2-1-18) into (3-2-3-5) results in

$$y(t) = K_a \left[\; C_k(\alpha_{out}) \quad C_d(\alpha_{out}) \;\right] \left[\begin{array}{c} q(t) \\ \dot{q}\,(t) \end{array}\right] + \frac{K_a}{m}\Phi(\alpha_{out})\Phi^T(\alpha_{in})u(t) \qquad (3\text{-}2\text{-}3\text{-}5)$$

where

$$\begin{aligned} C_k(\alpha_{out}) &= \Phi^{''}(\alpha_{out})\,\dot{\alpha}_{out}^2 + \Phi'(\alpha_{out})\,\ddot{\alpha}_{out} - \Phi(\alpha_{out})K(t) \qquad (3\text{-}2\text{-}3\text{-}6) \\ C_d(\alpha_{out}) &= 2\Phi'(\alpha_{out})\,\dot{\alpha}_{out} - \Phi(\alpha_{out})D_d(t). \end{aligned}$$

It is noted that α_{out} can also be expressed as

$$\alpha_{out} = 1 - \frac{r_{out}}{L} \qquad (3\text{-}2\text{-}3\text{-}7)$$

where r_{out} is the axial distance between the sensor and the tip of the beam and a constant. If there are one strain gauge sensor at α_{out1}, one deflection sensor at α_{out2}, a velocity sensor at α_{out3},and a acceleration sensor at α_{out4}, the output matrix and the direct transmission matrix are given as

$$C(t) = \left[\begin{array}{cc} K_{sg}\Phi^{''}(\alpha_{out1})/L^2 & \mathbf{0}_{1\times n} \\ K_d\Phi(\alpha_{out2}) & \mathbf{0}_{1\times n} \\ K_v\Phi^{'}(\alpha_{out3})\frac{\dot{L}}{L}(1-\alpha_{out3}) & K_v\Phi(\alpha_{out3}) \\ K_aC_k(\alpha_{out4}) & K_aC_d(\alpha_{out4}) \end{array}\right] \text{ and } D(t) = \left[\begin{array}{c} 0 \\ 0 \\ 0 \\ K_a\Phi(\alpha_{out4})\Phi^T(\alpha_{in})/m \end{array}\right] \qquad (3\text{-}2\text{-}3\text{-}8)$$

Generally, the output can be given as

$$y(t) = C(t)x(t) + D(t)u(t) \qquad (3\text{-}2\text{-}3\text{-}9)$$

where $C(t)$ is a time-varying output matrix and $D(t)$ a time-varying direct transmission matrix.

3.2.4 "Frozen" Modal Parameters

The concept of the modal parameters, including natural frequencies and damping ratios, is no longer valid for the time-varying system. Instead, the concept of the "frozen" modal parameters can be used [14, 16]. If the system is considered to be frozen at a time instant t, the eigendecompositon of $A(t)$ becomes

$$A(t) = \overline{V}(t)\overline{\mathbf{\Lambda}}(t)\overline{V}^{-1}(t) \tag{3-2-4-1}$$

where $\overline{V}(t)$ is a "frozen" eigenvector matrix at the time instant t, $\overline{\mathbf{\Lambda}}(t) = \mathbf{diag}\left[\overline{\lambda}_1(t), \overline{\lambda}_2(t), \cdots, \overline{\lambda}_{n_x}(t)\right]$ is a "frozen" diagonal eigenvalues matrix at the time instant t. A pair of complex "frozen" eigenvalues can be expressed as

$$\overline{\lambda}_i(t) = -\overline{\zeta}_i(t)\overline{\omega}_i(t) \pm j\overline{\omega}_i(t)\sqrt{1-\overline{\zeta}_i^2(t)} \tag{3-2-4-2}$$

where $\overline{\omega}_{n_i}(t)$ is defined to be the ith "frozen" natural frequency at the time instant t, $\overline{\zeta}_i(t)$ is defined to be the ith "frozen" damping ratio at the time instant t, and $j = \sqrt{-1}$.

3.2.5 Controllability and Observability of the System

The controllability and observability of a time-varying system is no longer defined by the ranks of the Q and P matrices in (3-1-20) and (3-1-21) respectively. However, for an approximate analysis, the concept of the "frozen" system can be used again. The controllability matrix of the time-varying system that is "frozen" at a time instant t is defined as

$$\overline{Q}(t) = \left[\begin{array}{ccccccc} B(t) & B(t)A(t) & B(t)A^2(t) & . & . & B(t)A^{n_x-1}(t) \end{array}\right] \tag{3-2-5-1}$$

The "frozen" system is controllable if the matrix $\overline{Q}(t)$ has a full rank at the time instant t , i.e., $\mathbf{rank}\left[\ \overline{Q}(t)\ \right] = n_x$.

Similarly, the observability matrix of the time-varying system that is "frozen" at time instant

t is defined as

$$\overline{P}(t) = \begin{bmatrix} C(t) \\ C(t)A(t) \\ C(t)A^2(t) \\ \cdot \\ \cdot \\ C(t)A^{n_x-1}(t) \end{bmatrix} \qquad (3\text{-}2\text{-}5\text{-}2)$$

The "frozen" system is observable if the matrix $\overline{P}(t)$ has a full rank at the time instant t, i.e., $\mathbf{rank}[\ \overline{P}(t)\ ] = n_x$.

To understand these two important matrices, an example is used. In this example, the first three vibratory modes are considered, or $n = 3$. Thus, the system order is 6, or $n_x = 6$. The trapezoid velocity profiles are used as axial motion profiles, as shown in Figure 3.2.3. Two kinds of scenarios are considered. Scenario A: axial extension in which the beam length varies from $L_{\min}$ to $L_{\max}$; Scenario B: axial retraction in which the beam length varies from $L_{\max}$ to $L_{\min}$. In either case, $L_{\min}$= 0.66 m and $L_{\max}$ = 1.09 m.

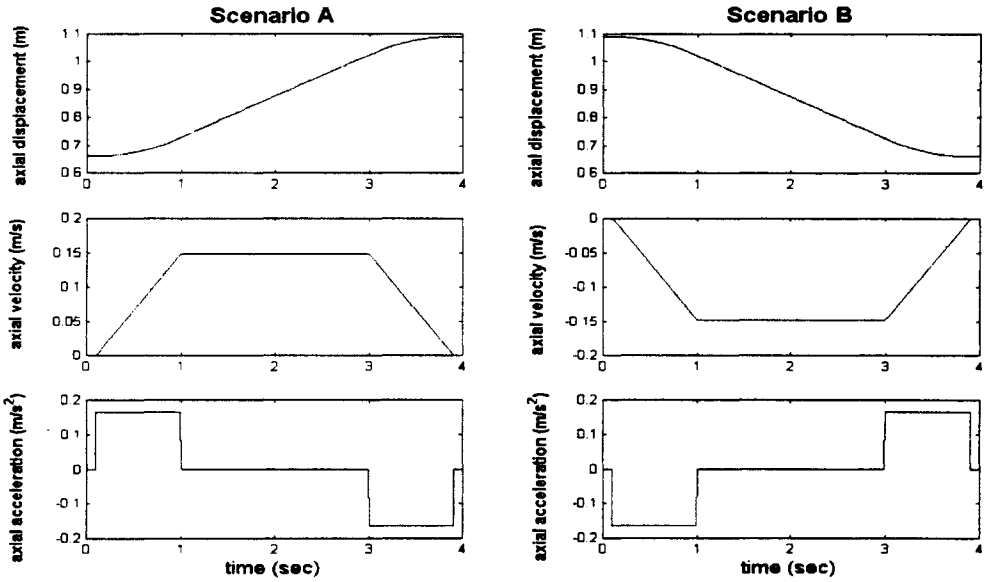

Figure 3.2.3 Axial motion profiles

The input is applied at r_{in} = 0.528 m in scenario A and r_{in} = 0.875 m in scenario B respectively.

The locations of two strain gauge sensors r_{out1} and r_{out2} are assumed to be 0.60 m and 0.30 m respectively with respect to the tip of the beam, or $r_{out1} = 0.60$ m and $r_{out2} = 0.30$ m. The $C(t)$, $Q(t)$ and $P(t)$ matrices are of the forms

$$C(t) = \begin{bmatrix} K_{sg}\Phi''(\alpha_{out1})/L^2 & \mathbf{0}_{1\times 3} \\ K_{sg}\Phi''(\alpha_{out2})/L^2 & \mathbf{0}_{1\times 3} \end{bmatrix}, \tag{3-2-5-3}$$

$$Q(t) = \frac{1}{m}\begin{bmatrix} \mathbf{0}_{3\times 1} & \Phi^T(\alpha_{in}) & \Phi^T(\alpha_{in}) & \cdots & \Phi^T(\alpha_{in}) \\ \Phi^T(\alpha_{in}) & -2(\frac{\dot{L}}{L})\Phi^T(\alpha_{in}) & \left(-2(\frac{\dot{L}}{L})\right)^2\Phi^T(\alpha_{in}) & \cdots & \left(-2(\frac{\dot{L}}{L})\right)^5\Phi^T(\alpha_{in}) \end{bmatrix}, \tag{3-2-5-4}$$

and

$$P(t) = \begin{bmatrix} K_{sg}\Phi''(\alpha_{out1})/L^2 & \mathbf{0}_{1\times 3} \\ K_{sg}\Phi''(\alpha_{out2})/L^2 & \mathbf{0}_{1\times 3} \\ \mathbf{0}_{1\times 3} & K_{sg}\Phi''(\alpha_{out1})/L^2 \\ \mathbf{0}_{1\times 3} & K_{sg}\Phi''(\alpha_{out2})/L^2 \\ \mathbf{0}_{1\times 3} & K_{sg}\Phi''(\alpha_{out1})/L^2 \\ \mathbf{0}_{1\times 3} & K_{sg}\Phi''(\alpha_{out2})/L^2 \end{bmatrix}. \tag{3-2-5-5}$$

Obviously, the "frozen" controllability depends on the mode shape function values $\Phi^T(\alpha_{in})$. The "frozen" observability depends on the values of $\Phi''(\alpha_{out1})/L^2, \Phi''(\alpha_{out2})/L^2$. Figure 3.2.4 shows $\Phi_i(\alpha_{in})$ versus time. Figure 3.2.5 shows $\Phi_i''(\alpha_{out1})/L^2$ and $\Phi_i''(\alpha_{out2})/L^2$ versus time. In these figures, a solid line represents the first mode, a dashed line the second mode, and a

dashdot line the third mode.

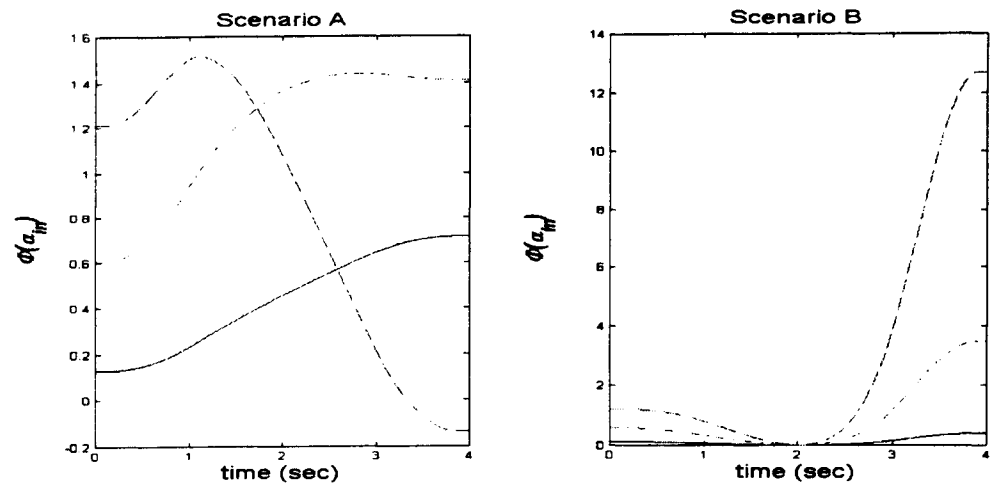

Figure 3.2.4 Varying magnitudes of $\Phi(\alpha_{in})$

It can be seen from Figure 3.2.4 that in scenario A, the "frozen" system is temporarily uncontrollable at one time instant.

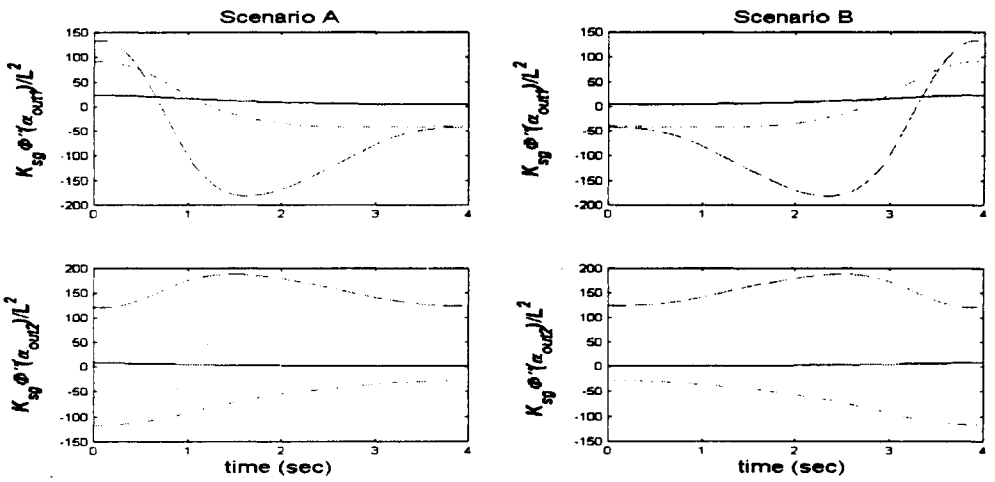

Figure 3.2.5 Varying magnitudes of $\Phi''(\alpha_{out1})/L^2$ and $\Phi''(\alpha_{out2})/L^2$

It can be seen from Figure 3.2.5 that for the two scenarios, the "frozen" system becomes temporarily unobservable at two time instants . It is interesting that such temporary unobservability occurs at the first sensor location, indicating that the axial position of the strain sensor influences the "frozen" observability of the system. The closer to the clamp the strain sensor,

the more unobservable the "frozen" system.

3.3 Simulation of the Axially-Moving Cantilever Beam

To understand how the axial motion influences the dynamics of the axially-moving cantilever beam system, it is necessary to simulate the dynamic responses of the system. In the simulation, the density ρ and the modulus E of elasticity of the beam material are 2800 kg/m^3 and 70.9 GPa respectively. The thickness b and height h of the cross-section of the beam are 3.175 mm and 50.6 mm respectively. The beam length varies from $L_{\min} = 0.66$ m to $L_{\max} = 1.09$ m. The axial motion profiles used in the simulation are the same as those in subsection 3.2.4. The first three flexible modes are considered in the simulation, i.e. the system order n_x is 6. Since the highest frequency $f_{\max}$ is 110.66 Hz when $L = L_{\min}$, the time step Δt is chosen to be 0.0005 second in order to capture the dynamics of the system.

The beam responses are observed at three locations. Location one is at $r_{out1} = 0.6435$ m and referred to as base location. Location two is at $r_{out2} = 0.335$ m and referred to as middle location. Location three is at $r_{out3} = 0.0$ m and referred to as tip location.

An impact with the magnitude of 10N is applied for a duration of 0.1 second. The beam is forced to move axially after the impact, i.e., $x(0) = \mathbf{0}_{6\times 1}$. To ensure that $\alpha_{in} = 0.25$ for both scenarios, the impact is applied at $r_{in} = 0.495$ m for scenario A, and at $r_{in} = 0.8175$ m for scneario B. The Runge-Kutta method is used to solve the equation numerically. The physical damping γ is not considered.

3.3.1 Influence of the Axial Force

In Section 3.2.1, two models are derived. Equation (3-2-1-7) is the model that considers the contribution of the axial force. Equation (3-2-2-1) is the model that does not consider the contribution of axial force. A natural question is how much the two models differ. To answer this question, the "frozen" modal parameters of the two models are evaluated and compared. Figures 3.3.1 and 3.3.2 show the "frozen" natural frequencies $\overline{f}$ and damping ratios $\overline{\zeta}$ based on the two models in scenario A and scenario B respectively. In the figures, the solid lines denote the "frozen" modal parameters based on the model without considering the contribution of the

axial force; and the dotted lines denote the "frozen" modal parameters based on the model with considering the contribution of the axial force.

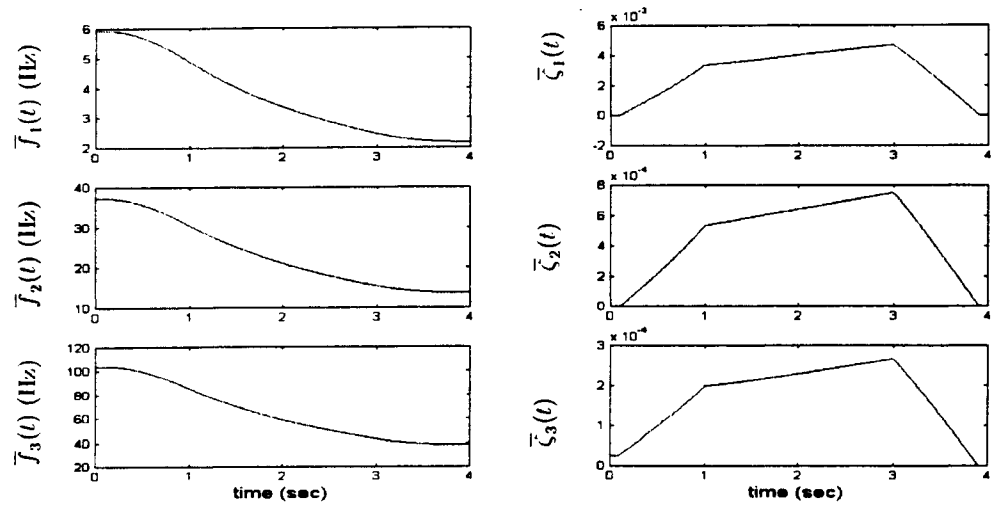

Figure 3.3.1 "Frozen" natural frequencies $\overline{f}$ and damping ratios $\overline{\zeta}$ for scenario A

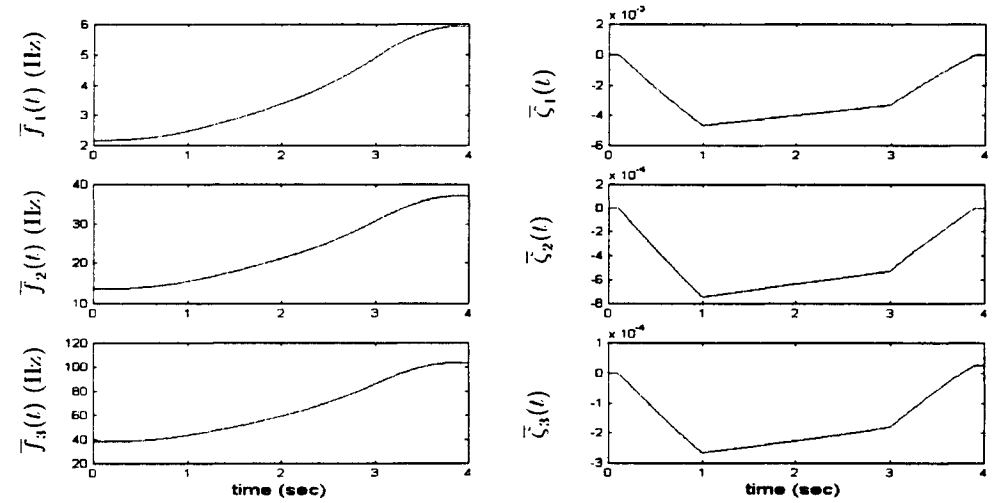

Figure 3.3.2 "Frozen" natural frequencies $\overline{f}$ and damping ratios $\overline{\zeta}$ for scenario B

From the figures, the following observations can be drawn:

(1) The axial force has little influence on the "frozen" modal parameters, as the two curves in each figure overlap each other. Thus, the model not considering the contribution of the axial force can be chosen in the following simulation, including the generalized coordinates

and derivatives, transient responses, true "pseudo" modal paremeters and identified "pesudo" modal parameters.

(2) The axial extension makes the "frozen" natural frequencies decrease and the axial retraction makes the "frozen" natural frequencies increase. Such behaviors are expected as the variations of stiffness and mass of the beam. The stiffness of the beam decreases and the mass of the beam increases as the beam extends. The stiffness of the beam increases and the mass of the beam decreases as the beam retracts.

(3) The axial extension induces positive "frozen" damping ratios, and the axial retraction induces negative "frozen" damping ratios. The reason for this is the sign of the damping matrix $D_d(t) = 2\,\dot{L}\,A_2/L$ that depends on the sign of the axial velocity. Therefore, the axial extension makes the system stable because of the positive damping effects, and the axial retraction make the system unstable because of the negative damping effects.

3.3.2 Generalized Coordinates and Velocities

Figure 3.3.3 and Figure 3.3.4 show the generalized coordinates and velocities for the axial extension and the axial retraction, respectively.

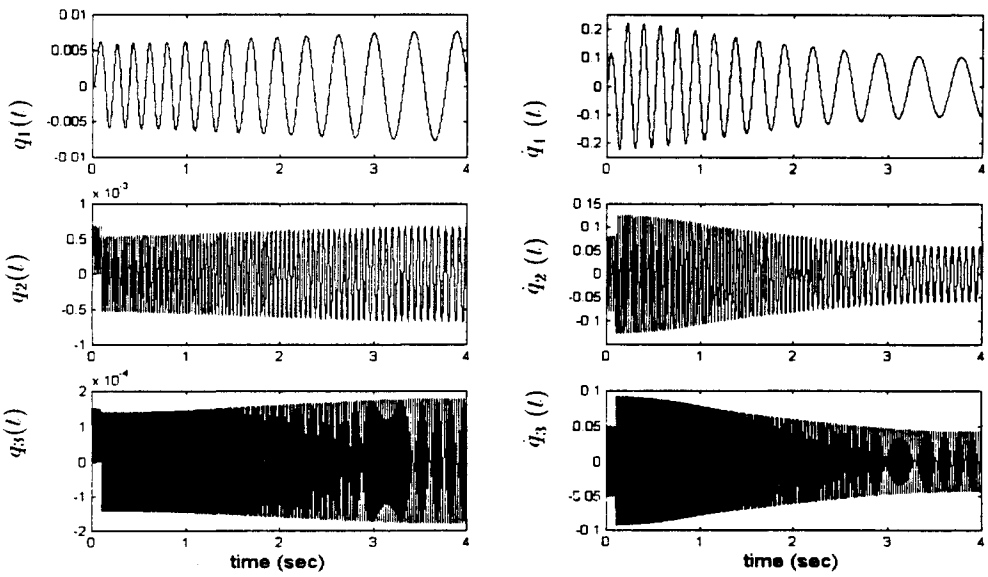

Figure 3.3.3 The generalized coordinates and velocities for the axial extension

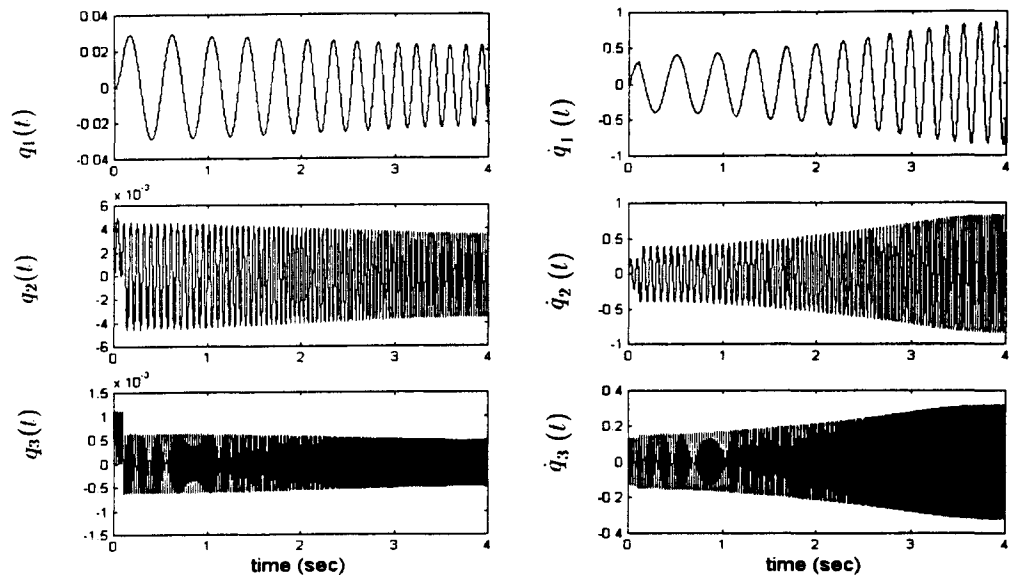

Figure 3.3.4 The generalized coordinates and velocities for the axial retraction

From the figures, the following observations can be drawn.

(1) The magnitudes of the generalized coordinates and velocities in scenario B are greater than those in scenario A. The reason for this is that the initial stiffness of the beam in scenario B is smaller than that in scenario A, because the initial length of the beam in scenario B is longer than that in scenario A.

(2) An axial extension results in an increase of the magnitude of the generalized coordinates and a decrease of the magnitude of the generalized velocities. An axial retraction results in a decrease of the generalized coordinates and an increase of the magnitude of the generalized velocities. This can be explained by the variation of the beam stiffness $K(t)$. The axial extension reduces the stiffness of the beam, which makes the beam's flexing easier. The axial retraction increases the stiffness of the beam, which makes the beam's flexing more difficult.

(3) The magnitude of the first mode is much greater than the magnitudes of the second and the third modes in the generalized coordinates. The magnitude of the third mode is smaller than the magnitudes of the first and second modes in the generalized velocities.

3.3.3 Transient Responses

In the following, the simulation results of transient responses, including strain, deflection, velocity and acceleration signals at the three output positions namely the base location, the middle location and the tip location are presented. In this case, the output matrix can be given as

$$y(t) = C(t)x(t) + D(t)u(t) \tag{3-4-1}$$

where $u(t)$ is the distributed impact force, the output matrix $C(t)$ with the dimension 12×6 is shown as

$$C(t) = \begin{bmatrix} K_{sg}\Phi''(\alpha_{out1})/L^2 & \mathbf{0}_{1\times 3} \\ K_{sg}\Phi''(\alpha_{out2})/L^2 & \mathbf{0}_{1\times 3} \\ K_{sg}\Phi''(\alpha_{out3})/L^2 & \mathbf{0}_{1\times 3} \\ K_d\Phi(\alpha_{out1}) & \mathbf{0}_{1\times 3} \\ K_d\Phi(\alpha_{out2}) & \mathbf{0}_{1\times 3} \\ K_d\Phi(\alpha_{out3}) & \mathbf{0}_{1\times 3} \\ K_v\Phi'(\alpha_{out1})\frac{\dot{L}}{L}(1-\alpha_{out1}) & K_v\Phi(\alpha_{out1}) \\ K_v\Phi'(\alpha_{out2})\frac{\dot{L}}{L}(1-\alpha_{out2}) & K_v\Phi(\alpha_{out2}) \\ K_v\Phi'(\alpha_{out3})\frac{\dot{L}}{L}(1-\alpha_{out3}) & K_v\Phi(\alpha_{out3}) \\ K_aC_k(\alpha_{out1}) & K_aC_d(\alpha_{out1}) \\ K_aC_k(\alpha_{out2}) & K_aC_d(\alpha_{out2}) \\ K_aC_k(\alpha_{out3}) & K_aC_d(\alpha_{out3}) \end{bmatrix} = [C_{ij}] \tag{3-4-2}$$

$$D(t) = \begin{bmatrix} 0 \\ 0 \\ 0 \\ 0 \\ 0 \\ 0 \\ 0 \\ 0 \\ 0 \\ K_a\Phi(\alpha_{out1})\Phi^T(\alpha_{in})/m \\ K_a\Phi(\alpha_{out2})\Phi^T(\alpha_{in})/m \\ K_a\Phi(\alpha_{out3})\Phi^T(\alpha_{in})/m \end{bmatrix} = [D_{ij}] \qquad (3\text{-}4\text{-}3)$$

and the output vector is given as

$$y(t) = [\ y_1(t)\quad y_2(t)\quad y_3(t)\quad y_4(t)\quad y_5(t)\quad y_6(t)\quad y_7(t)\quad y_8(t)\quad y_9(t)\quad y_{10}(t)\quad y_{11}(t)\quad y_{12}(t)\ ]^T \qquad (3\text{-}4\text{-}4)$$

where $y_1(t)$, $y_2(t)$ and $y_3(t)$ are the strain gauge outputs at the base location, the middle location and the tip location, respectively; $y_4(t)$, $y_5(t)$ and $y_6(t)$ are the deflection outputs at the base location, the middle location and the tip location, respectively; $y_7(t)$, $y_8(t)$ and $y_9(t)$ are the velocity outputs at the base location, the middle location and the tip location, respectively; and $y_{10}(t)$, $y_{11}(t)$ and $y_{12}(t)$ are acceleration outputs at the base location, the middle location and the tip location, respectively.

In order to understand how the vibratory modes, the generalized coordinates, and/or generalized velocities make the contribution to the transient responses, the outputs can be expressed as

$$y_j(t) = \sum_{i=1}^{n_x} C_{ji}(t)x_i(t) = \sum_{i=1}^{n_x} y_{ji}(t)$$

In the following simulation, the gains of output measurements are $K_{sg} = 1000$ (V), $K_d = 1$ (V/m), $K_v = 1$ (V/m.s^{-1}), and $K_a = 0.01$ (V/m.s^{-2}).

1) Strain Gauge Outputs

Figure 3.3.5 shows the strain outputs for motion scenario A and B respectively.

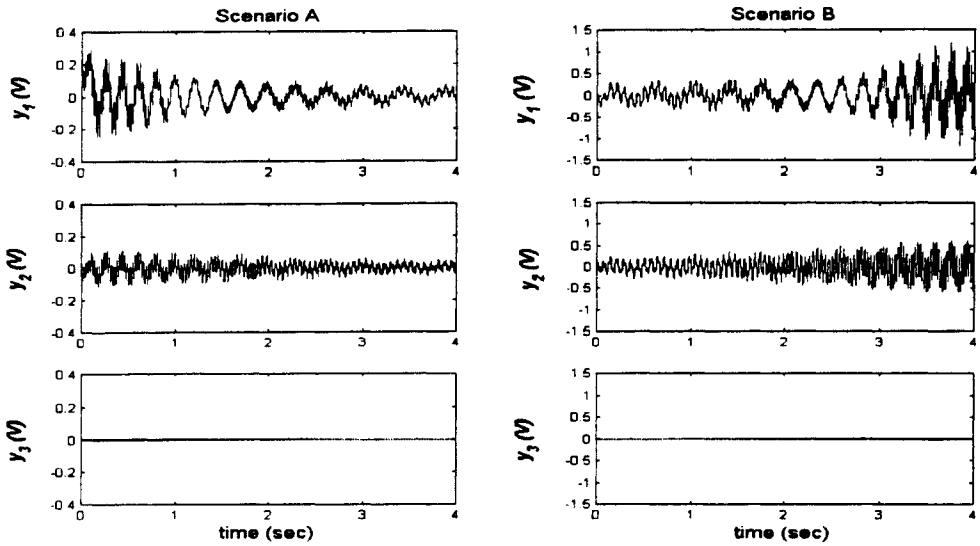

Figure 3.3.5 Strain outputs for motion scenarios A and B

It can be seen that for the base and middle locations, the axial extension results in a decrease of the magnitudes of the strain outputs while the axial retraction results in an increase of the magnitudes of the strain outputs. The behavior can be explained by the variations of $\Phi_i''(\alpha_{out})/L^2$ and generalized coordinates $q(t)$. As the beam length increases, the term $\Phi_i''(\alpha_{out})/L^2$ and $q(t)$ becomes smaller. And as the beam length decreases, the term $\Phi_i''(\alpha_{out})/L^2$ and $q(t)$ becomes larger. For the tip location, the strain signals remain at zero as $\Phi_i''(\alpha_{out3}) = 0$ $(i = 1, 2, 3)$ because of $\alpha_{out3} = 1$. It is also noted that the magnitude of the strain signal at the base location is greater than that at the middle location.

To see how the vibratory modes contribute to the strain output signals at the base and the middle locations, the strain output components, or y_{1i} and y_{2i} $(i = 1, 2, 3)$, are plotted in the following figures.

Figure 3.3.6 shows three components of the strain output at the base location for the two

motion scenarios.

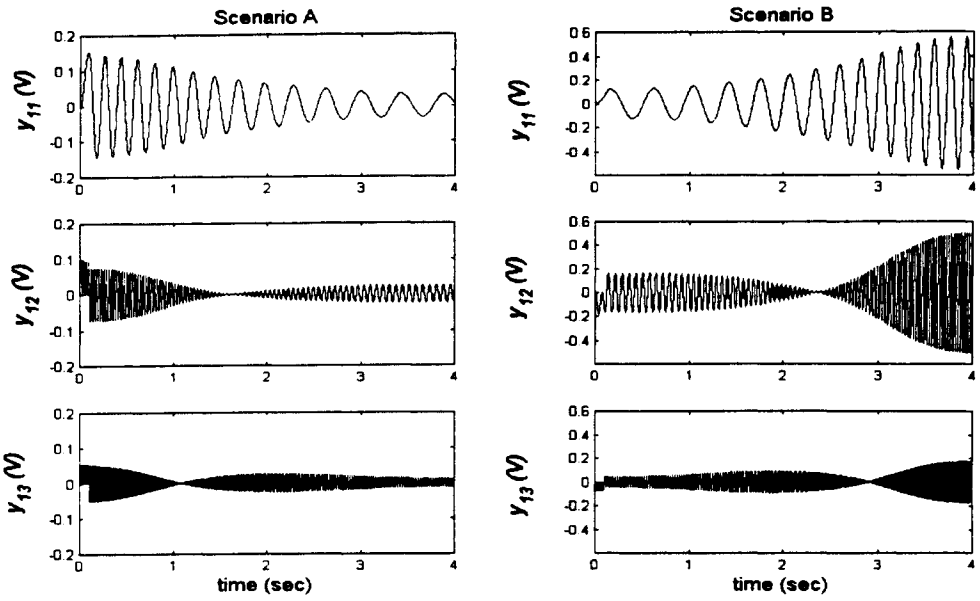

Figure 3.3.6 Strain output components $y_{1i}(i = 1, 2, 3)$ at the base location

It can be seen that the higher the mode index, the less it contributes to the total response. The response components from the second and third modes become zero when the sensor location coincides with the points where $\Phi_i''(\alpha_{out}) = 0$. The axial extension decreases the magnitude of the first mode component y_{11} while the axial retraction increases the magnitude of the first mode component y_{11}.

Figure 3.3.7 shows the three components of the strain outputs at the middle location for the two motion scenarios. It can be seen that the total response is dominated by the contribution of the second mode. Only the third mode component experiences the instantaneous zero point of $\Phi_3''(\alpha_{out}) = 0$. The response components of the first mode and the second mode, or y_{21} and y_{22}, decrease during the axial extension and increase during the axial retraction. However, it seems that the component of the third mode, or y_{23}, increases during the axial extension and decreases during the axial retraction.

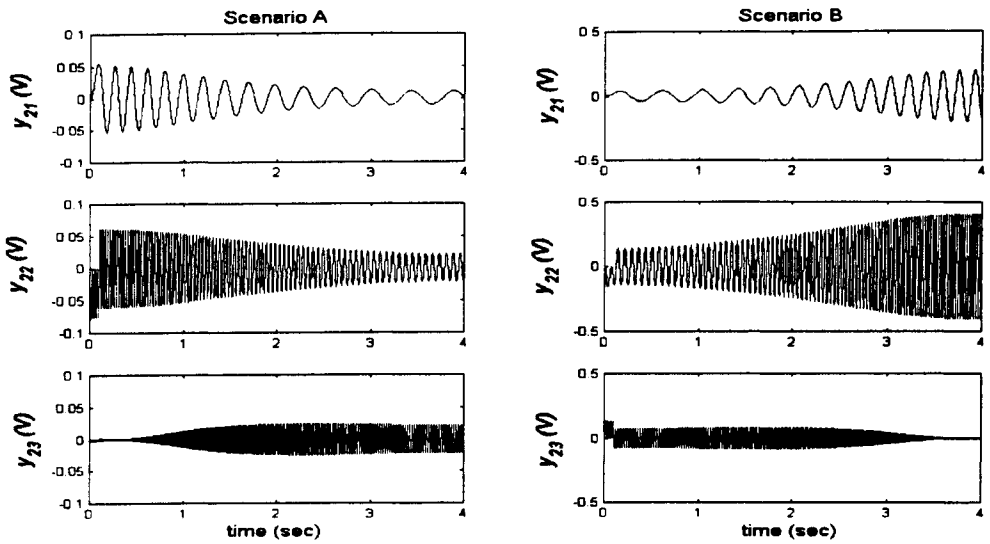

Figure 3.3.7 Strain output components $y_{2i}(i = 1, 2, 3)$ at the middle location

2) Deflection Outputs

Figure 3.3.8 shows the deflection outputs at the three locations for the axial extension and the axial retraction.

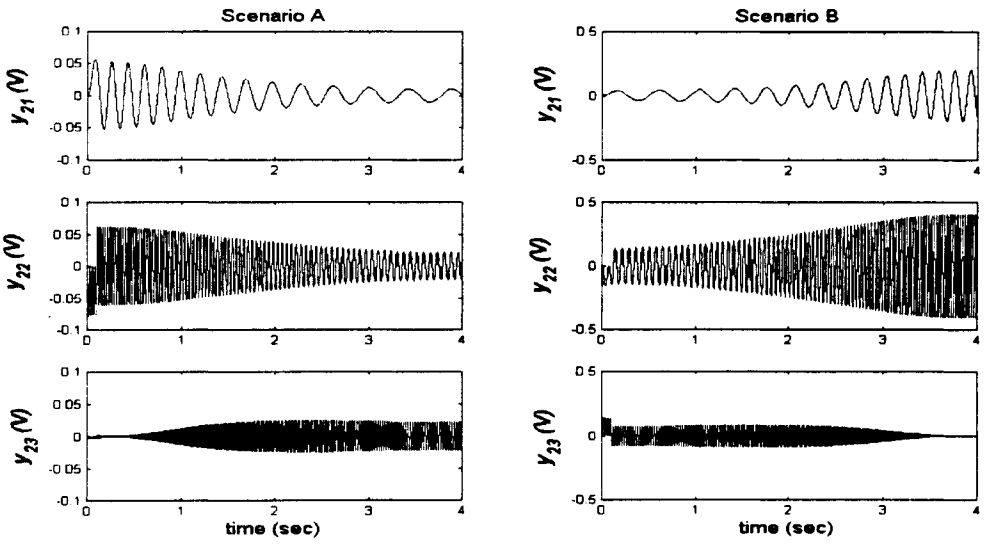

Figure 3.3.8 Deflection outputs for motion scenarios A and B

The figure shows that the axial extension results in an increase of the deflection responses and axial retraction results in a decrease of the deflection responses. The further the observation location away from the clamper, the larger the response magnitude. It should be pointed out that the deflection outputs behave differently from the strain outputs. The former diverges as the beam extends while the latter diverges as the beam retracts. The behavior of the deflection can be explained by the variation of the stiffness of the beam. The stiffness of the beam decreases as the beam extends and increases as the beam retracts..

To evaluate how the vibratory modes contribute to the transient responses of deflections, the magnitudes of deflection output components, or y_{4i}, y_{5i} and y_{6i} $(i = 1, 2, 3)$ are plotted in Figures 3.3.9, 3.3.10, and 3.3.11, showing the deflection output components at the base location, the middle location and the tip location respectively.

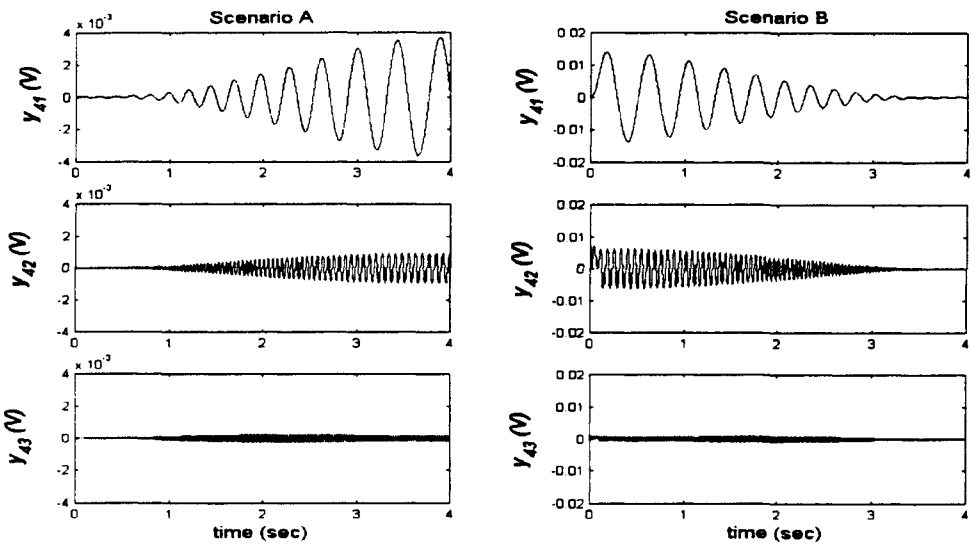

Figure 3.3.9 Deflection output components $y_{4i}(i = 1, 2, 3)$ at the base location

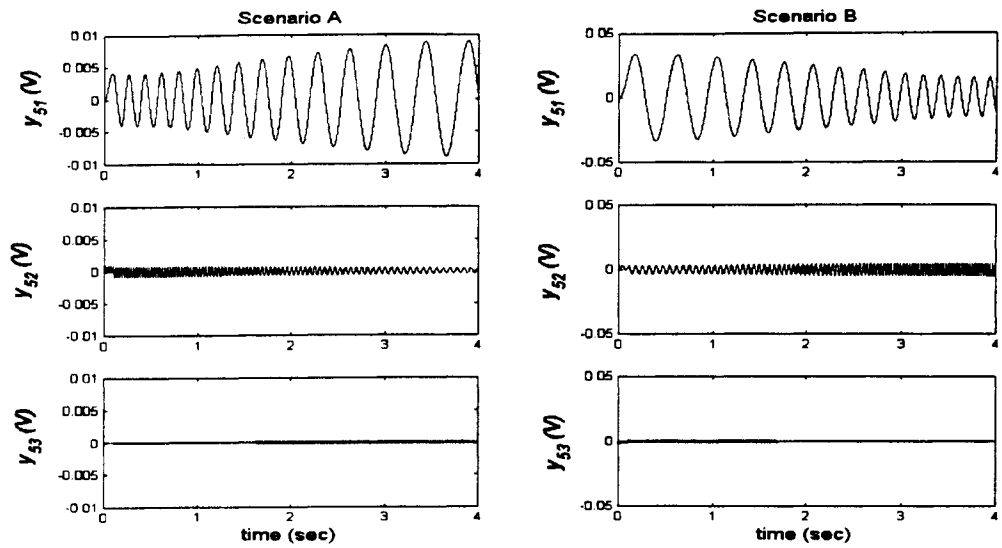

Figure 3.3.10 Deflection output components $y_{5i}(i = 1, 2, 3)$ at the middle location

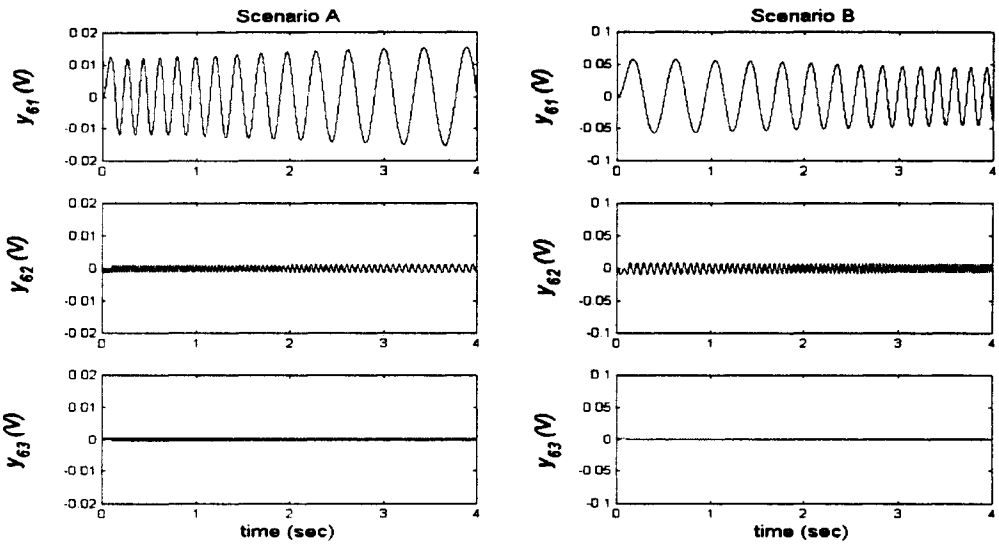

Figure 3.3.11 Deflection output components $y_{6i}(i = 1, 2, 3)$ at the tip location

As expected, it can be seen that the higher the mode index, the less it contributes to the total response. The contribution of the first mode is dominant in the three deflection output components. The further the observation location from the clamp, the greater the magnitudes of the deflection output components. It can be explained that the magnitude of $\Phi_1(\alpha_{out3})q_1(t)$ at the tip location is much larger than those of $\Phi_1(\alpha_{out2})q_1(t)$ and $\Phi_1(\alpha_{out1})q_1(t)$.

3) Velocity Outputs

Figure 3.3.12 shows velocity outputs for the two motion scenarios.

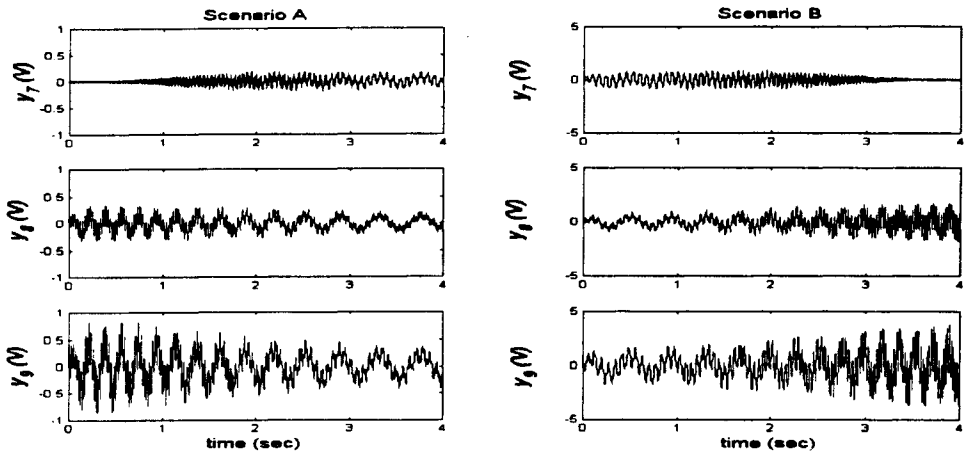

Figure 3.3.12 Velocity outputs for motion scenarios A and B

It can be seen that the further the observation from the clamp, the larger the magnitudes of velocity responses. To see how the vibratory modes contribute to the velocity signals at the base location, the middle loction and the tip location, the velocity output components, or y_{7i}, y_{8i} and y_{9i} $(i = 1, 2, 3, 4, 5, 6)$, are plotted in the following figures.

Figure 3.3.13 and Figure 3.3.14 show the velocity output components y_{7i} $(i = 1, 2, 3)$ and the velocity output components y_{7i} $(i = 4, 5, 6)$ at the base location, respectively.

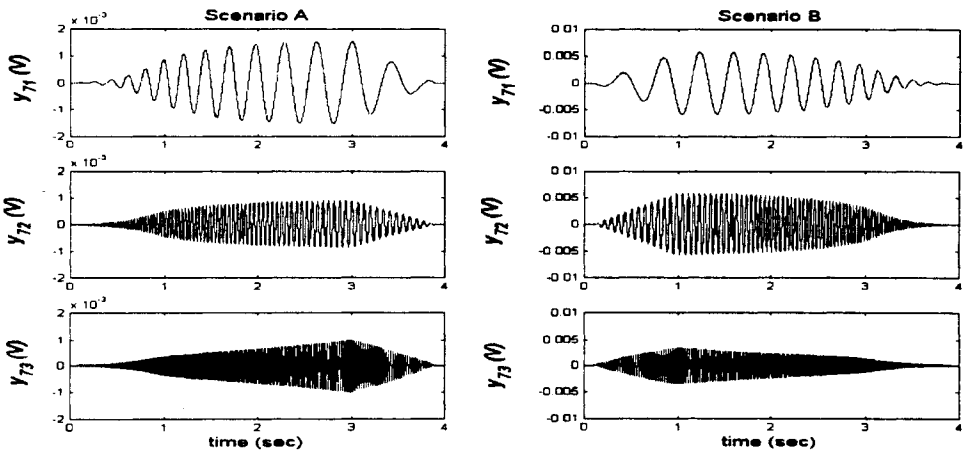

Figure 3.3.13 Velocity output components $y_{7i}(i = 1, 2, 3)$ at the base location

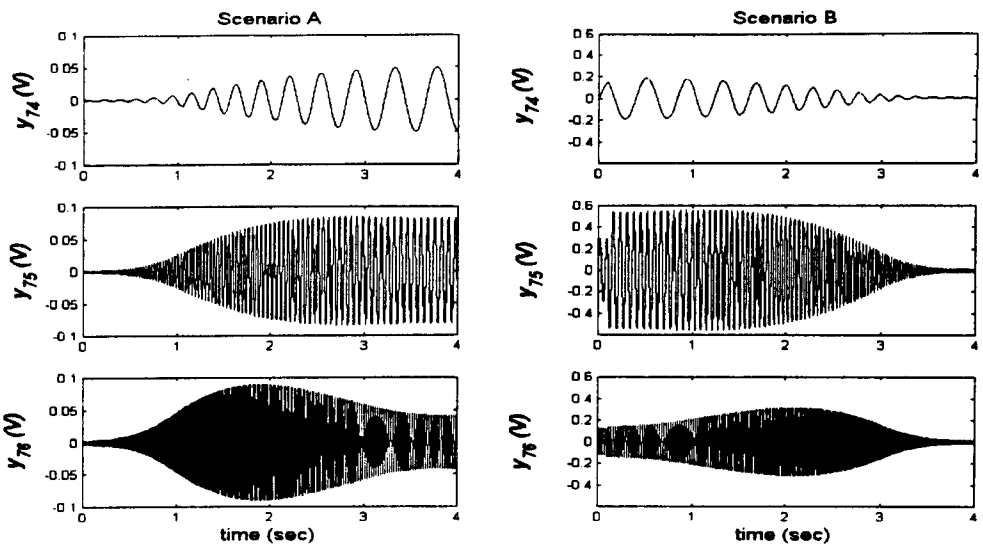

Figure 3.3.14 Velocity output components $y_{7i}(i = 4, 5, 6)$ at the base location

It is noted that the components y_{7i} $(i = 1, 2, 3)$ are induced by the axial motion and such terms may be referred to as motion-induced terms. Compared with the components y_{7i} $(i = 4, 5, 6)$ that associated with the mode shape functions and generalized velocities, the motion-induced terms have much smaller magnitudes.

Figure 3.3.15 and Figure 3.3.16 show the velocity components y_{8i} $(i = 1, 2, 3)$ and the velocity components y_{8i} $(i = 4, 5, 6)$ at the middle location respectively.

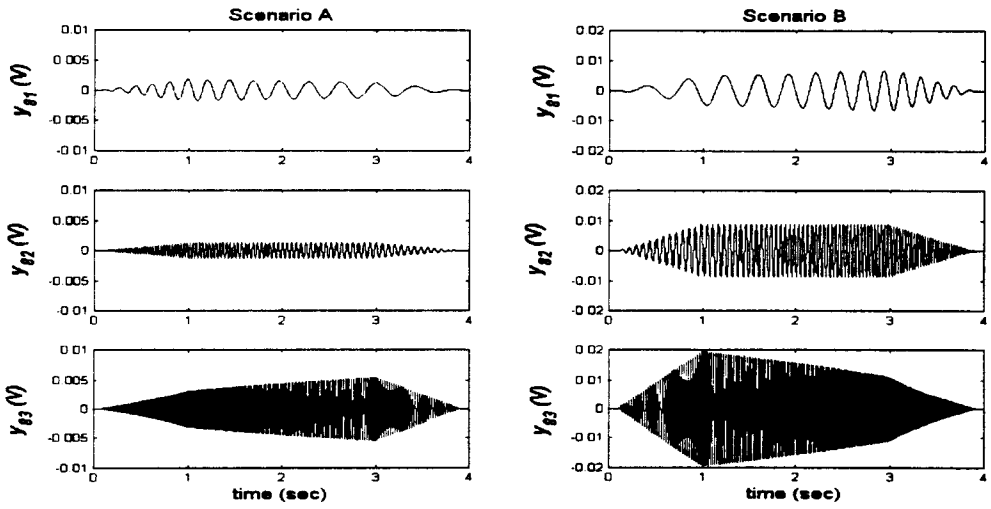

Figure 3.3.15 Velocity output components $y_{8i}(i = 1, 2, 3)$ at the middle location

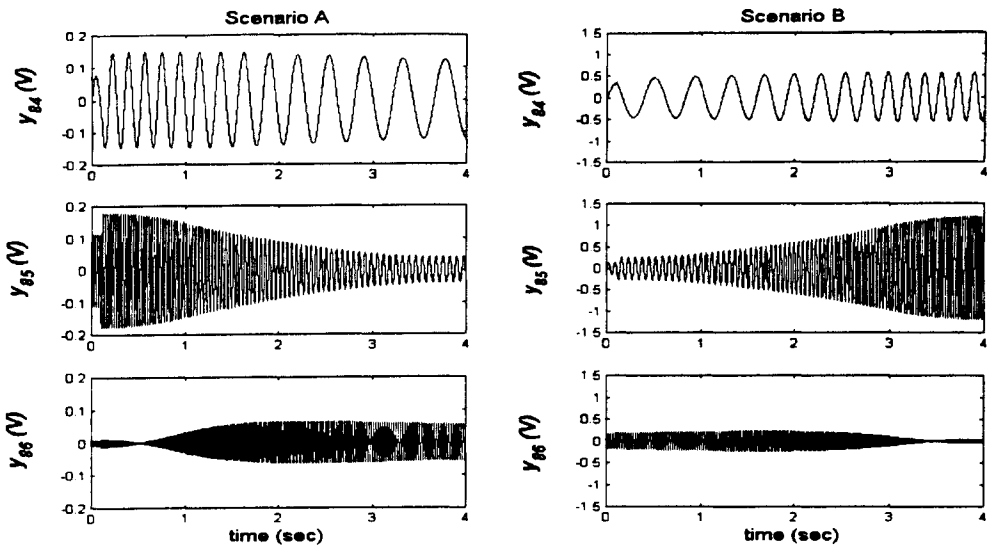

Figure 3.3.16 Velocity output components $y_{8i}(i = 4, 5, 6)$ at the middle location

Similarly, the magnitudes of motion-induced response components y_{8i} $(i = 1, 2, 3)$ are much smaller than those of the components y_{8i} $(i = 4, 5, 6)$ associated with the generalized velocities and mode shape functions. For the motion-induced terms, the third mode makes larger contribution to the responses than the first mode and the second mode do. For the components y_{8i} $(i = 4, 5, 6)$ associated with generalized velocities, the contributions of the first mode and second mode are dominant in the two scenarios. The third mode components experience a temporary vanishing.

When $\alpha_{out3} = 1$,the motion-induced velocity response components is zero due to fact that $\phi_i'(\alpha_{out3})\frac{\dot{L}}{L}(1 - \alpha_{out3}) = 0$, and the components y_{9i} $(i = 4, 5, 6)$ associated with combination between the generalized velocities and the mode shape function is constant. or $\Phi(\alpha_{out3}) = [2 \quad -2 \quad 2]$. Figure 3.3.17 shows such components. It is noted that none of them vanishes

temporarily.

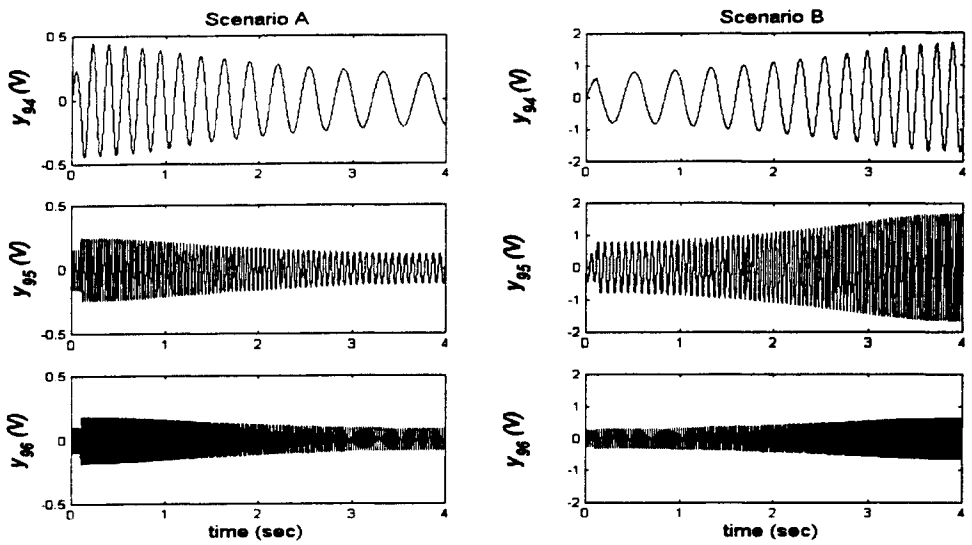

Figure 3.3.17 Velocity output components $y_{9i}(i = 4, 5, 6)$ at the tip location

4) Acceleration Outputs

Figure 3.3.18 shows the acceleration outputs for the two scenarios.

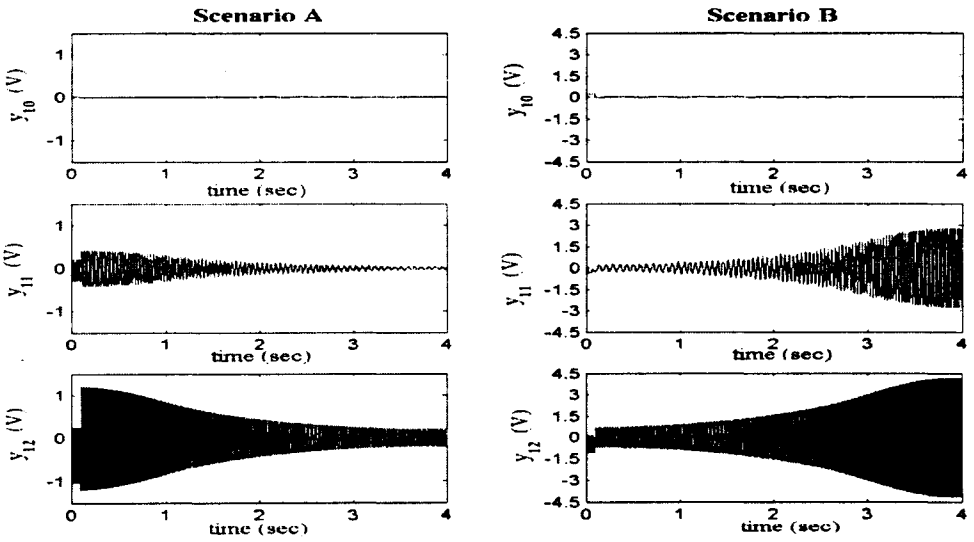

Figure 3.3.18 Acceleration outputs for motion scenarios A and B

It can be seen that the further the observation location from the clamp, the larger the magnitudes of the acceleration responses. To evaluate how the vibratory modes contribute to the acceleration signals at the base location, the middle loction and the tip location, the acceleration output components, or y_{10i}, y_{11i} and y_{12i} $(i = 1, 2, 3, 4, 5, 6)$, are plotted in the following figures.

Figure 3.3.19 and Figure 3.3.20 show the acceleration output components y_{10i} $(i = 1, 2, 3)$ and y_{10i} $(i = 4, 5, 6)$ at the base location, respectively.

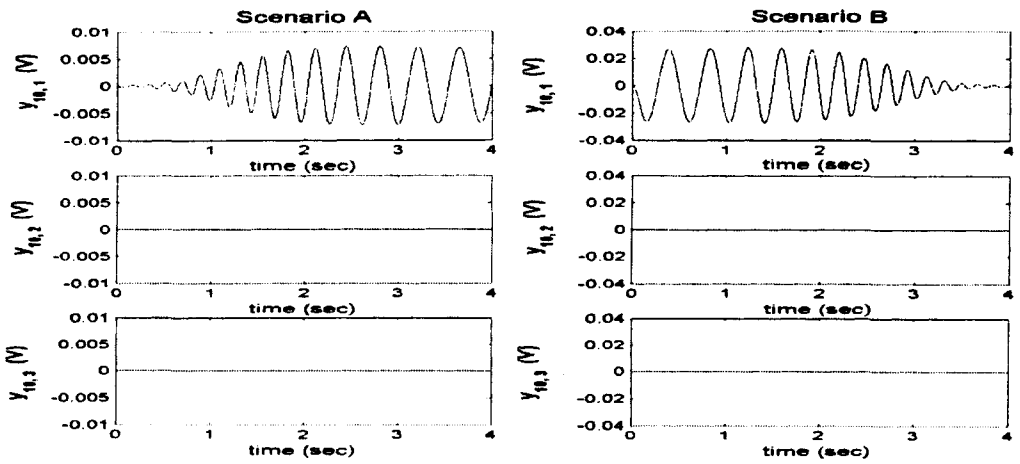

Figure 3.3.19 Acceleration output components $y_{10i}(i = 1, 2, 3)$ at the base location

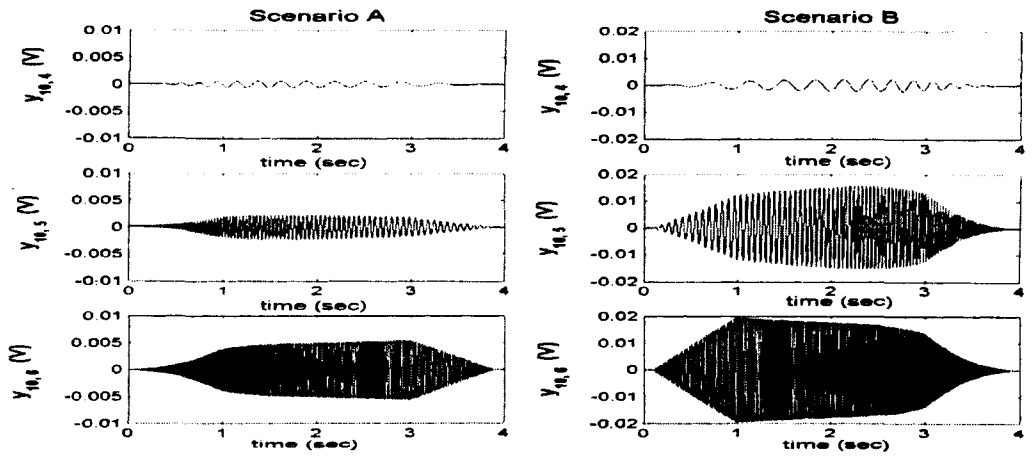

Figure 3.3.20 Acceleration output components $y_{10i}(i = 4, 5, 6)$ at the base location

Obviously, under scenarios A and B, for the components y_{10i} $(i = 1, 2, 3)$ associated with the

generalized coordinates, the first mode makes a larger contribution to the response than the second and third modes do; for the components y_{10i} $(i = 4, 5, 6)$ associated with the generalized velocities, the contribution of the third mode to the response is the most dominant, and the contribution of the first mode is the least dominant.

Figure 3.3.21 and Figure 3.3.22 show the acceleration components y_{11i} $(i = 1, 2, 3)$ and y_{11i} $(i = 4, 5, 6)$ at the middle locations.

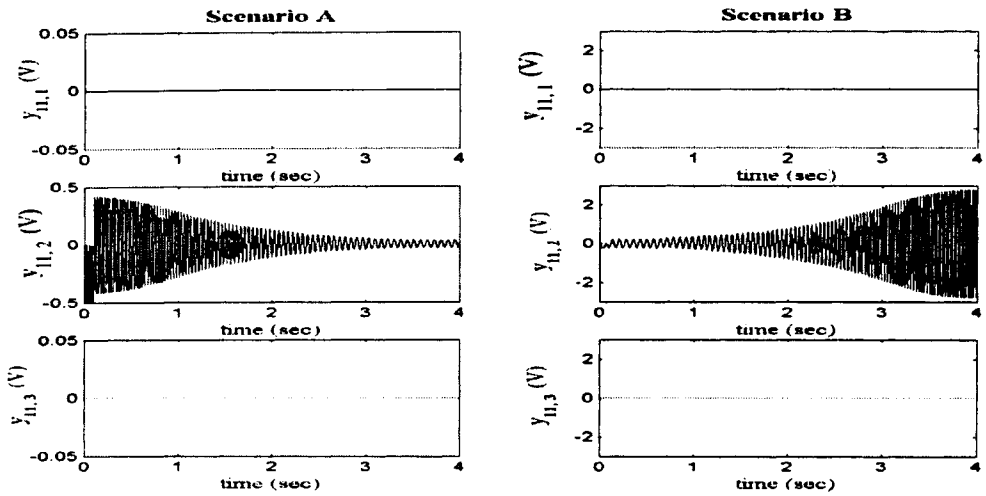

Figure 3.3.21 Acceleration output components $y_{11i}(i = 1, 2, 3)$ at the middle location

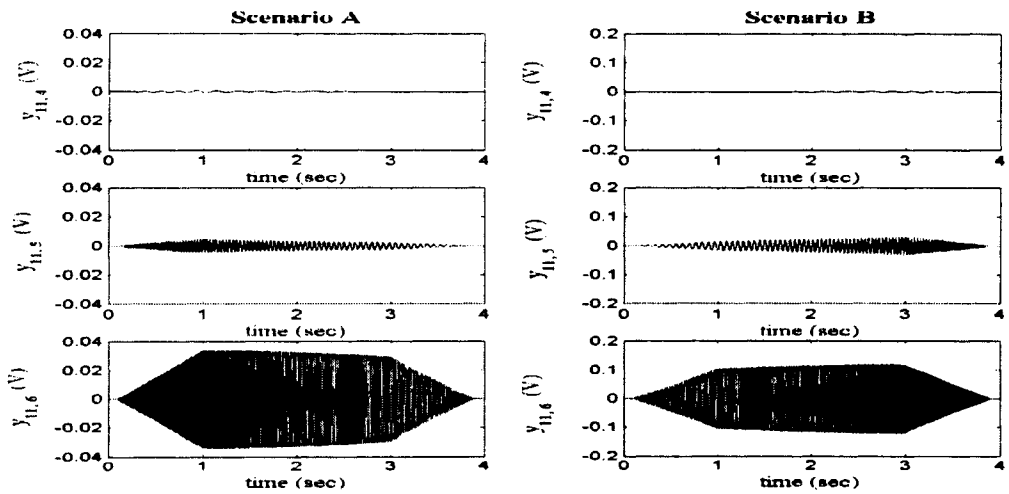

Figure 3.3.22 Acceleration output components $y_{11i}(i = 4, 5, 6)$ at the middle location

For the components y_{11i} $(i = 1, 2, 3)$ associated with the generalized coordinates, the magnitude

of the second one is the larger than those of the first and third ones. For the components y_{11i} $(i = 4, 5, 6)$ associated with the generalized velocities, the magnitude of the third one is larger than those of the first and second ones. It should be pointed out the magnitude of the second component associated with the generalized coordinates is much larger than the any other components associated with the generalized coordinates and velocities. Thus, the second mode associated with the generalized coordinates is dominant in the response.

Figure 3.3.23 and Figure 3.3.24 shows acceleration components y_{12i} $(i = 1, 2, 3)$ and y_{12i} $(i = 4, 5, 6)$ at the tip location, respectively.

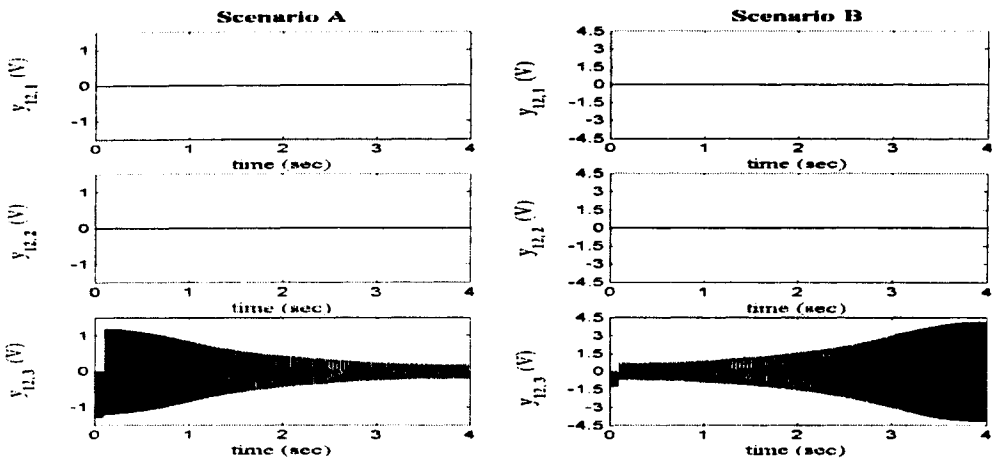

Figure 3.3.23 Acceleration output components $y_{12i}(i = 1, 2, 3)$ at the tip location

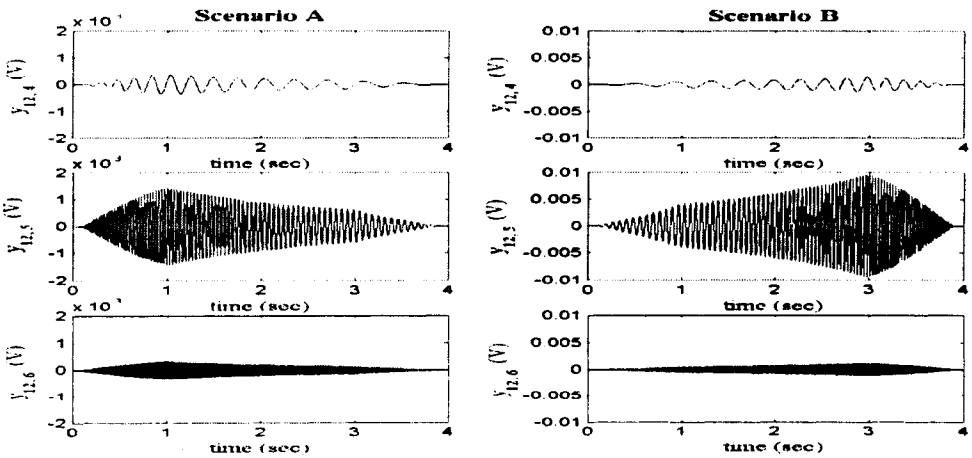

Figure 3.3.24 Acceleration output components $y_{12i}(i = 4, 5, 6)$ at the tip location

Similarly, for the components y_{12i} $(i = 1, 2, 3)$ associated with the generalized coordinates, the magnitude of the third one is much larger than those of the first and second ones; for the components y_{12i} $(i = 4, 5, 6)$ associated with the generalized coordinates, the magnitude of the second one is larger than those of the first and the third ones. Apparently, the magnitude of the third component associated with the generalized coordinates is also much larger than that of any other components associated with the generalized coordinates and velocities. Thus, the third mode associated with the generalized coordinates is dominant in the response.

3.4 Evaluation of Varying Discrete-Time State Transition Matrix

The concept of the "pseudo" modal parameters was proposed to characterize the global properties of a time-varying system in [14,16]. The "pseudo" modal parameters are based on the eigenvalues of the discrete-time state transition matrix. This section defines the "pseudo" modal parameters and evaluates them numerically for the model under study. A comparison between the "pseudo" modal parameters and the "frozen" modal parameters is presented.

3.4.1 Discrete-Time State Transition Matrix and " Pseudo" Modal Parameters

A discrete-time state-space representation of a time-varying system under an initial condition is given as [14]

$$x(k+1) = G(k+1,k)x(k), \quad x(0); \quad y(k) = C(k)x(k) \tag{3-4-1-1}$$

where $G(k+1,k)$ is an $n_x \times n_x$ discrete-time state transition matrix. $x(0)$ is the initial condition. $C(k)$ is an $n_y \times n_x$ output matrix. Note that the two important properties of $G(k+1,k)$ are

$$G(k+1,h) = G(k+1,k)G(k,h), \quad k > h; \quad G(h,h) = \mathbf{I} \tag{3-4-1-2}$$

If the varying discrete-time state transition matrix $G(k+1,k)$ is non-singular, the corre-

sponding eigendecomposition exists, i.e.,

$$G(k+1,k) = V(k)\Lambda(k)V^{-1}(k) \tag{3-4-1-3}$$

where. $V(k)$ is the eigenvector matrix and $\Lambda(k) = \mathbf{diag}\,[\lambda_1(k), \lambda_2(k), \ldots, \lambda_n(k)]$ is the eigenvalue matrix. Since the elements of the $G(k+1,k)$ are real, the complex eigenvalues occur in pairs. If the ith eigenvalue is complex, then the following relation can be used

$$\lambda_i(k) = \lambda^*_{i+n_x/2}(k) = \exp\left[\left(-\zeta_i(k)\omega_i(k) \pm j\omega_i(k)\sqrt{1-\zeta_i^2(k)}\right)\Delta t\right] \tag{3-4-1-4}$$

where $\zeta_i(k), \omega_i(k)$ are defined as the ith "pseudo" damping ratio and "pseudo" natural frequency respectively.

3.4.2 Numerical Evaluation of the Discrete-Time State Transition Matrix

The varying discrete-time state transition matrix $G(k+1,k)$ can be found using an ensemble of n_x sets of states since it satisfies a matrix equation given by

$$X(k+1) = G(k+1,k)X(k) \tag{3-4-2-1}$$

where

$$X(k) = [x^1(k) \quad x^2(k), ..., x^{n_x}(k)]$$

is the state matrix at time instant k and

$$X(k+1) = [x^1(k+1) \quad x^2(k+1), ..., x^{n_x}(k+1)]$$

is the state matrix at time instant $k+1$. Note that $x^j(k)$ is generated by an initial condition $x^i(0)$. The transition matrix can be found by

$$G(k+1,k) = X(k+1)X^{-1}(k). \tag{3-4-2-2}$$

To ensure the existence of $X^{-1}(k)$, the n_x states must be independent of one another. The n_x state sequences are numerically found by the Runge-Kutta algorithm.

3.4.3 Comparison between the "Frozen" and "Pseudo" Modal Parameters

To obtain "pseudo" modal parameters, including natural frequencies and damping ratios, the true varying discrete-time state transition matrices are evaluated using an ensemble of n_x sets of states. The two scenarios mentioned in subsection 3.2.4 are used. The n_x sets of initial states are generalized randomly in order to ensure independence of the sets of initial states. The parameters used in the simulation, including the duration of the axial motion, time step, and system order n_x etc., are the same as those used previously for the comparison. The n_x sets of states were numerically obtained using the Runge-Kutta method. The comparisons between the "pseudo" and "frozen" modal parameters are shown in Figure 3.4.1 and Figure 3.4.2 for axial extension and retraction. In these figures, a solid line represents the "pseudo" modal parameters and a dashdot line represents the "frozen" modal parameters.

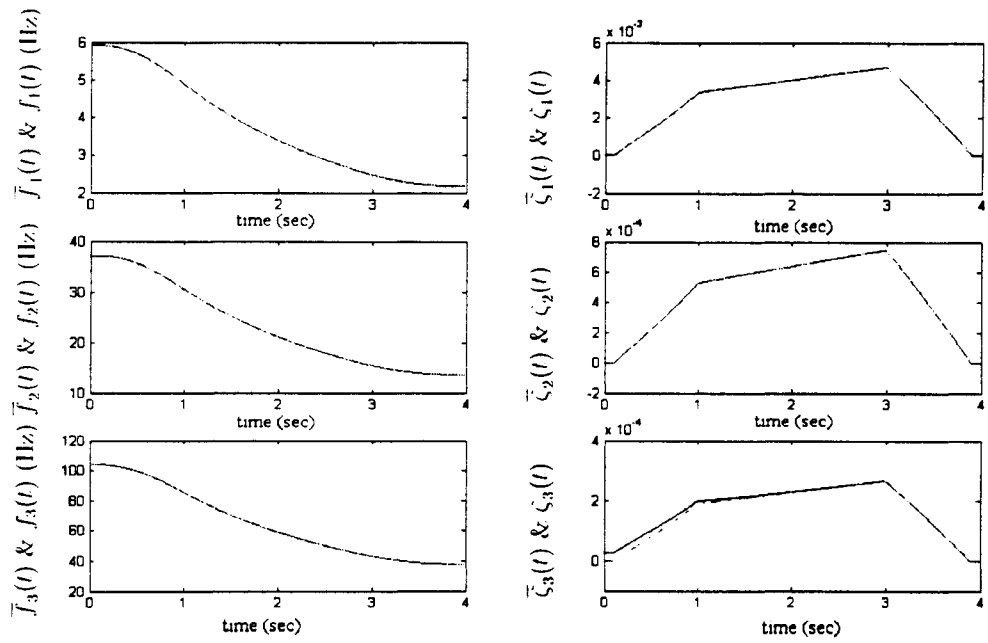

Figure 3.4.1 The "pseudo" and "frozen" modal parameters for axial extension

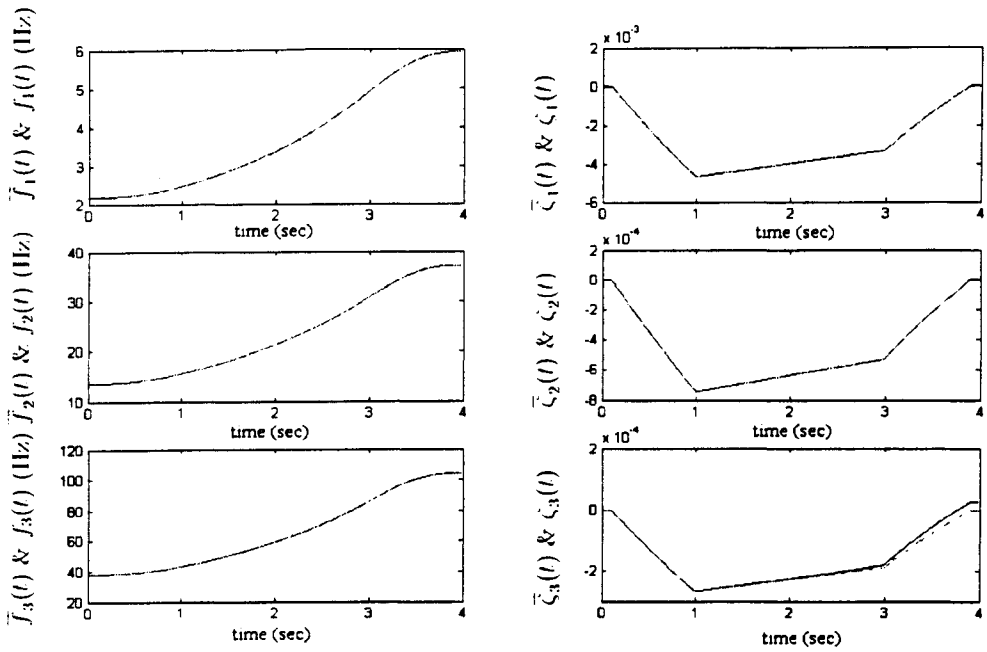

Figure 3.4.2 The "pseudo" and "frozen" modal parameters for axial retraction

The figures show that the curves representing the "pseudo" values and the curves representing the "frozen" values virtually overlap each other except for a small discrepancy in the damping ratios of the third mode. This indicates that the two types of the modal parameters are almost identical for this particular system. The reason that the two types of the modal parameters are identical can be explained by the slow variability of the system matrix $A(t)$ [14]. An approximate form of a general discrete-time state transition matrix can be obtained using a series expansion

$$G(k+1,k) = I+A(k)\Delta t+\frac{1}{2}[A^2(k)+\dot{A}(k)]\Delta t^2+\frac{1}{3!}[A^3(k)+A(k)\dot{A}(k)+2\dot{A}(k)+\ddot{A}(k)]\Delta t^3+... \quad \text{(3-4-3-1)}$$

If the derivatives $\dot{A}(k)$, $\ddot{A}(k)$, ..., are small , the discrete-time state transition matrix $G(k+1,k)$ can be approximated by

$$G(k+1,k) = I + A(k)\Delta t + \frac{1}{2}A^2(k)\Delta t^2 + \frac{1}{3!}A^3(k)\Delta t^3 + .. = \exp(A(k)\Delta t). \quad \text{(3-4-3-2)}$$

Thus, the evaluation of the "pseudo" modal parameters using this approximate transition ma-

trix will result in the "frozen" modal parameters.

3.5 Conclusions

Based on the results presented in this chapter, it is concluded that

1. The model is a linear time-varying system. The contribution by the axial force to the dynamics of the system is negligible.

2. The axial motion influences dynamics of the system, including "frozen" modal parameters, generalized coordinates and velocities, as well as the transient responses. The contributions of individual vibratory modes to the transient responses are different for the different types of sensors and their locations along the beam.

3. To evaluate the varying discrete-time transition state matrix numerically, the system must undergo the same variation and an ensemble of n_x sets of initial states must be generated randomly. The "pseudo" modal parameters are very close to the "frozen" modal parameters for the system under study.

Chapter 4

Identification of the Axially-Moving Cantilever Beam

The third objective of the thesis is to verify an identification algorithm using the axially-moving cantilever beam system. The algorithm was presented in [16]. It identifies the discrete-time state space model of a LTV system using an ensemble of freely vibrating responses. The ensemble of the responses are obtained through multiple experiments on the system while the system undergoes the same change.

The rest of the chapter is organized as follows: Section 4.1 reviews a subspace-based identification algorithm for linear time-invariant (LTI) systems; then, the algorithm was applied to identify the fixed-length cantilever beam system, Section 4.2 briefly reviews the identification algorithm using an ensemble of the responses, Section 4.3 presents the identification results based on the freely vibrating responses from the analytical model, Section 4.4 presents the identification results based on the experimental responses, Section 4.5 presents the identification results of identified "pseudo" natural frequencies based on the experimental responses, and Section 4.6 contains the conclusions.

4.1 A Subspace-Based Identification Algorithm

4.1.1 State Space Representation of LTI Systems

The state space representation of an $n_x/2$-degree-of-freedom freely vibrating LTI system is given by

$$\dot{x}(t) = Ax(t), \quad x(0); \quad y(t) = Cx(t) \tag{4-1-1}$$

where $x(t)$ is a vector of n_x state variables, $x(0)$ is the initial condition, A is an $n_x \times n_x$ constant system matrix, C is an $n_y \times n_x$ output matrix, and $y(t)$ is a vector of n_y responses. The corresponding discrete-time state space is expressed as

$$x(k+1) = Gx(k) \quad x(0); \quad y(k) = Cx(k) \tag{4-1-2}$$

where G is an $n_x \times n_x$ state transition matrix given by

$$G = \exp(A\Delta t) \tag{4-1-3}$$

where Δt is the sampling interval. The solution of equation (4-1-2) is

$$y(k) = Cx(k) = CG^k x(0). \tag{4-1-4}$$

It is noted that the description of equation (4-1-2) is not unique. Let T be an $n_x \times n_x$ non-singular matrix and define a new state vector $z = Tx$. Replacing x by $T^{-1}z$ in equation (4-1-2) results in

$$z(k+1) = \overline{G}z(k), \quad y(k) = \overline{C}(k)z(k) \tag{4-1-5}$$

where

$$\overline{G} = TGT^{-1} \quad \text{and} \quad \overline{C} = CT^{-1}. \tag{4-1-6}$$

Equation (4-1-5) is another representation of the system defined by equation (4-1-2). Such operation is referred to as similarity transformation. One of the important properties of the similarity transformation is that G and $\overline{G}$ share the same eigenvalue, i.e.,

$$G = \Psi\Lambda\Psi^{-1} \quad \text{or} \quad \overline{G} = (T\Psi)\Lambda(T\Psi)^{-1} \tag{4-1-7}$$

where $\Lambda = \mathbf{diag}\ (\lambda_1, \lambda_2, ..., \lambda_{n_x})$ is the diagonal eigenvalue matrix and Ψ is the eigenvector matrix. Note that for an underdamped vibratory system, the n_x eigenvalues and eigenvectors occur in complex conjugate pairs. Thus, the eigenvalues can be arranged as

$$\lambda_i = \lambda^*_{i+n_x/2} = \exp\left[\left(-\zeta_i\omega_i + j\omega_i\sqrt{1-\zeta_i^2}\right)\Delta t\right] \tag{4-1-8}$$

where $j = \sqrt{-1}$, ζ_i is the ith damping ratio, and ω_i is the ith natural frequency.

4.1.2 Hankel Matrix and Observability Matrix

(1) Hankel Matrix

Using a series of freely vibrating responses $y(k)$, $k = 0, 1, 2, ...K_s - 1$, and K_s is data length, a block Hankel matrix is formed as

$$H = \begin{bmatrix} y(0) & y(1) & . & . & . & y(N-1) \\ y(1) & y(2) & . & . & . & y(N) \\ . & . & . & . & . & . \\ . & . & . & . & . & . \\ . & . & . & . & . & . \\ y(M-1) & y(M) & . & . & . & y(M+N-2) \end{bmatrix} \tag{4-1-9}$$

where M is the block row number, and N is the column number. Using the relation of equation (4-1-4), the Hankel matrix can be factored as

$$H = \Gamma X$$

where

$$\Gamma = \begin{bmatrix} C \\ CG \\ CG^2 \\ \vdots \\ CG^{M-1} \end{bmatrix} \tag{4-1-10}$$

is the observability matrix of the system, and

$$X = \begin{bmatrix} x(0) & x(1) & \cdots & x(N-1) \end{bmatrix} \tag{4-1-11}$$

is the state matrix. Define two matrices Γ_1 and Γ_2 which are obtained by retaining the first $(M-1)$ blocks and the last $(M-1)$ blocks of the observability matrix Γ, i.e.,

$$\Gamma_1 = \begin{bmatrix} C \\ CG \\ CG^2 \\ \vdots \\ CG^{M-2} \end{bmatrix} \qquad \Gamma_2 = \begin{bmatrix} CG \\ CG^2 \\ CG^3 \\ \vdots \\ CG^{M-1} \end{bmatrix}. \tag{4-1-12}$$

Therefore an estimate of the G matrix can be obtained by solving

$$G = [\Gamma_1]^+ \Gamma_2 \tag{4-1-13}$$

where $(.)^+$ denotes the Moore-Penrose pseudo inverse.

(2) Extraction of the Range Space of the Observability Matrix

A matrix $\overline{\Gamma}$ is said to have the same range space as Γ, or i.e.,

$$\overline{\Gamma} = \Gamma T^{-1} = \begin{bmatrix} \overline{C} \\ \overline{C}\,\overline{G} \\ \overline{C}\,\overline{G}^2 \\ \vdots \\ \overline{C}\,\overline{G}^{M-1} \end{bmatrix} \tag{4-1-14}$$

if T is an $n_x \times n_x$ non-singular transformation matrix. Thus the first block row of $\overline{\Gamma}$ is $\overline{C}$ and $\overline{G}$ is given as

$$\overline{G} = [\overline{\Gamma}_1]^+ \overline{\Gamma}_2 \tag{4-1-15}$$

where

$$\overline{\Gamma}_1 = \begin{bmatrix} \overline{C} \\ \overline{C}\,\overline{G} \\ \overline{C}\,\overline{G}^2 \\ \vdots \\ \overline{C}\,\overline{G}^{M-2} \end{bmatrix} \quad \text{and} \quad \overline{\Gamma}_2 = \begin{bmatrix} \overline{C}\,\overline{G} \\ \overline{C}\,\overline{G}^2 \\ \overline{C}\,\overline{G}^3 \\ \vdots \\ \overline{C}\,\overline{G}^{M-1} \end{bmatrix}. \tag{4-1-16}$$

In practice, the measured responses are contaminated by noise such that

$$\widehat{y}(k) = y(k) + w(k) \qquad k = 1, 2, \ \ldots, \ N \tag{4-1-17}$$

where $\widehat{y}(k)$ is the measured response vector and $w(k)$ is the noise vector. The Hankel matrix formed by the noisy responses becomes

$$\widehat{H} = H + W = \begin{bmatrix} \widehat{y}(0) & \widehat{y}(1) & \ldots & \widehat{y}(N-1) \\ \widehat{y}(1) & \widehat{y}(2) & \ldots & \widehat{y}(N) \\ \cdot & \cdot & \cdots & \cdot \\ \cdot & \cdot & \cdots & \cdot \\ \cdot & \cdot & \cdots & \cdot \\ \widehat{y}(M-1) & \widehat{y}(M) & \ldots & \widehat{y}(M+N-2) \end{bmatrix}. \tag{4-1-18}$$

The singular value decomposition (SVD) is used to extract the observability range space because of its numerical stability. For the case where output measurements are free of noise, it can be proved that [21, 23, 24]

$$\text{Range } [\widehat{H}\widehat{H}^T] = \text{Range } (\Gamma) \tag{4-1-19}$$

where $\widehat{H}\widehat{H}^T$ is a covariance matrix. The above equality shows that the system observability range space can be obtained from the Hankel matrix constructed from the experimental data.

In practice, Range $[\widehat{H}\widehat{H}^T]$ does not exactly equal to Range(Γ) due to the fact that the measured output is contaminated by the noise. To estimate Range(Γ), applying the SVD to $[\widehat{H}\widehat{H}^T]$, i.e.,

$$\widehat{H}\widehat{H}^T = \begin{bmatrix} \overline{U}_{n_x} & \overline{U}_{n_w} \end{bmatrix} \begin{bmatrix} \overline{\Sigma}_{n_x} & \mathbf{0} \\ \mathbf{0} & \overline{\Sigma}_{n_w} \end{bmatrix} \begin{bmatrix} \overline{U}_{n_x} & \overline{U}_{n_w} \end{bmatrix}^T$$

where $\overline{U}_{n_x}$ is an $Mn_y \times n_x$ matrix and $\overline{U}_{n_w}$ is an $Mn_y \times (Mn_y - n_x)$ matrix , $\overline{\Sigma}_{n_x} = \text{diag}\,[\overline{\sigma}_i]$ is an $n_x \times n_x$ diagonal matrix of singular values σ_i, for $i = 1, 2, ..n_x$, $\overline{\Sigma}_{n_w}$ is an $(Mn_y - n_x)$ $\times(Mn_y - n_x)$ diagonal matrix of singular values $\overline{\sigma}_{n_x+i}$, for $i = 1, 2, .., Mn_y - n_x$. Thus, the identified system order n_x can be estimated by the following criteria,

$$\begin{aligned} \overline{\sigma}_i &\geqslant \overline{\sigma}, \quad i = 1, 2, ..., n_x \\ \overline{\sigma}_{n_x+i} &< \overline{\sigma}, \quad i = 1, 2, ..., Mn_y - n_x \end{aligned} \tag{4-1-20}$$

where $\overline{\sigma}$ is a prespecified threshold. The estimation of the observability matrix Γ of the system is given as

$$U_{n_x} \approx \overline{\Gamma} = \Gamma T^{-1} = \begin{bmatrix} \overline{C} \\ \overline{C}\,\overline{G} \\ \overline{C}\,\overline{G}^2 \\ \vdots \\ \overline{C}\,\overline{G}^{M-1} \end{bmatrix}. \tag{4-1-21}$$

4.1.3 The Computation Procedure

1. Form the Hankel matrices $\widehat{H}$ according to equation (4-1-18) using freely vibrating responses;

2. Apply the SVD to the covariance matrix $\widehat{H}\widehat{H}^T$, obtain an estimate of the system order n_x by comparing the singular values to a prespecified threshold $\overline{\sigma}$;

3. Partition U_{n_x} into $\overline{\Gamma}_1$ and $\overline{\Gamma}_2$ according to equation (4-1-16);

4. Obtain $\overline{C}$. Compute $\overline{G}$ using equation (4-1-15).

4.1.4 Experimental Results

The experimental setup is shown in the Figure 4.1.1.

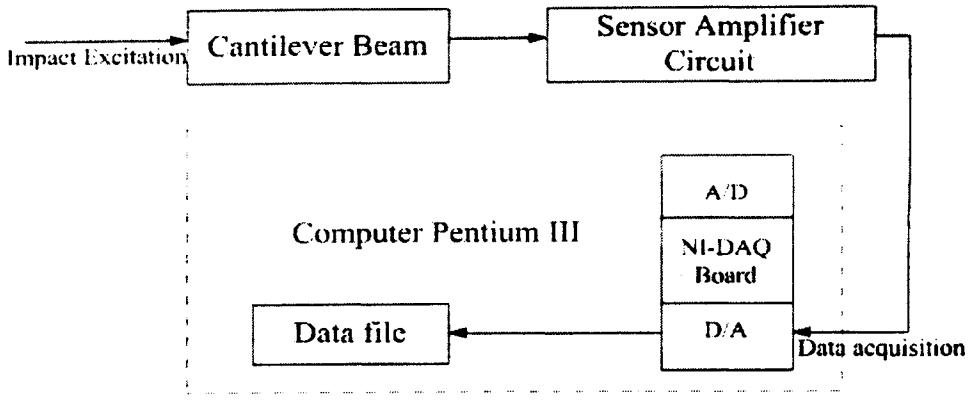

Figure 4.1.1 The experimental setup for a fixed-length cantilever beam

The outputs are two strain gauge outputs and one acceleration output, namely BSG (Base Strain Gauge), MSG (Middle Strain Gauge), and TAC (Tip Accelerometer). The BSG and MSG sensors are located at the positions of 0.642 m and 0.335 m with respect to the tip of the beam, or i.e., $r_{out1} = 0.642$ m and $r_{out2} = 0.335$ m, respectively. The TAC sensor is located near the tip of beam, or $r_{out3} = 0.003$ m. The BSG, MSG and TAC signals are acquired through channel 1, channel 2, and channel 3 of the NI-DAQ board. The six fixed lengths of the cantilever beam are considered. The impact acts at $s_{in} = 0.105$ m from the clamp for all the beam lengths. The sampling interval is $\Delta t = 0.001$ (sec). The data length is selected to be $K_s = 6000$. The block row number is chosen as $M = 100$ and the column number $N = K_s - M + 1 = 5901$. The experimental results are given below.

A. Identified Modal Parameters

The identified system order $n_x = 8$ is used for lengths of 0.66 m, 0.746 m and 0.832 m and $n_x = 10$ for lengths of 0.918 m, 1.004 m and 1.10 m, respectively. The modal parameters, including the natural frequencies and damping ratios of vibratory modes are identified and listed in Table 4.1. For each beam length, nine experiments were conducted. The results in Table 4.1 are the average values of the nine experiments. The relative error between the

identified and analytical natural frequencies is given as

$$\Delta_i = \left| \frac{f_i - f_i^{true}}{f_i^{true}} \right| \times 100 \ (\ \%\ ) \qquad (4\text{-}1\text{-}23)$$

where f_i is the ith identified natural frequency and f_i^{true} is the ith analytical natural frequency. The analytical natural frequencies are evaluated using equation (3-1-4).

Figure 4.1 The identified natural frequencies and damping ratios

Mode *No.*	Parameters	Fixed length (m)					
		0.6600	0.7460	0.8320	0.9180	0.1.004	1.0900
The first mode	ζ_1	0.0100	0.0053	0.0064	0.0135	0.0105	0.0153
	f_1 (Hz)	4.9350	3.9610	3.2157	2.6615	2.2656	2.1723
	f_1^{true} (Hz)	5.9250	4.6376	3.7284	3.0625	2.5604	2.1723
	Δ_1 (%)	16.704	14.6010	13.7550	13.0950	11.5130	9.6137
The second mode	ζ_2	0.0100	0.0092	0.0082	0.0070	0.0063	0.0060
	f_2 (Hz)	31.535	25.190	20.470	17.006	14.400	12.389
	f_2^{true} (Hz)	37.130	29.063	23.365	19.190	16.046	13.613
	Δ_2 (%)	15.068	13.325	12.343	11.383	10.261	8.9885
The third mode	ζ_3	0.0096	0.0093	0.0079	0.0063	0.0069	0.0052
	f_3 (Hz)	87.660	70.017	62.576	48.068	40.810	35.016
	f_3^{true} (Hz)	103.97	81.377	65.424	53.740	44.928	38.118
	Δ_3 (%)	15.687	12.731	4.3541	10.5545	9.1669	8.1364
The fourth mode	ζ_4	N / A	N / A	N / A	0.0076	0.0072	0.0065
	f_4 (Hz)	N / A	N / A	N / A	99.553	80.810	68.449
	f_4^{true} (Hz)	203.73	159.48	128.41	105.31	88.041	74.496
	Δ_4 (%)	N / A	N / A	N / A	9.265	11.689	8.363

Based on the table, some observations can be drawn:

(1) As expected, the magnitudes of the natural frequencies decrease as the beam lengths increase. Figure 4.1.2 shows a comparison between the identified natural frequencies and the analytical ones, where "o" represents the identified values and "*" the true values. The relative errors between the analytical and identified natural frequencies ranges from 4.58 to 16.7 percent. It is noted that the identified natural frequencies are lower than the theoretical ones. Such

discrepancies may be due to the fact that the actual beam does not have an ideal clamp boundary condition since there is a clearance needed between the beam and the guiding slot.

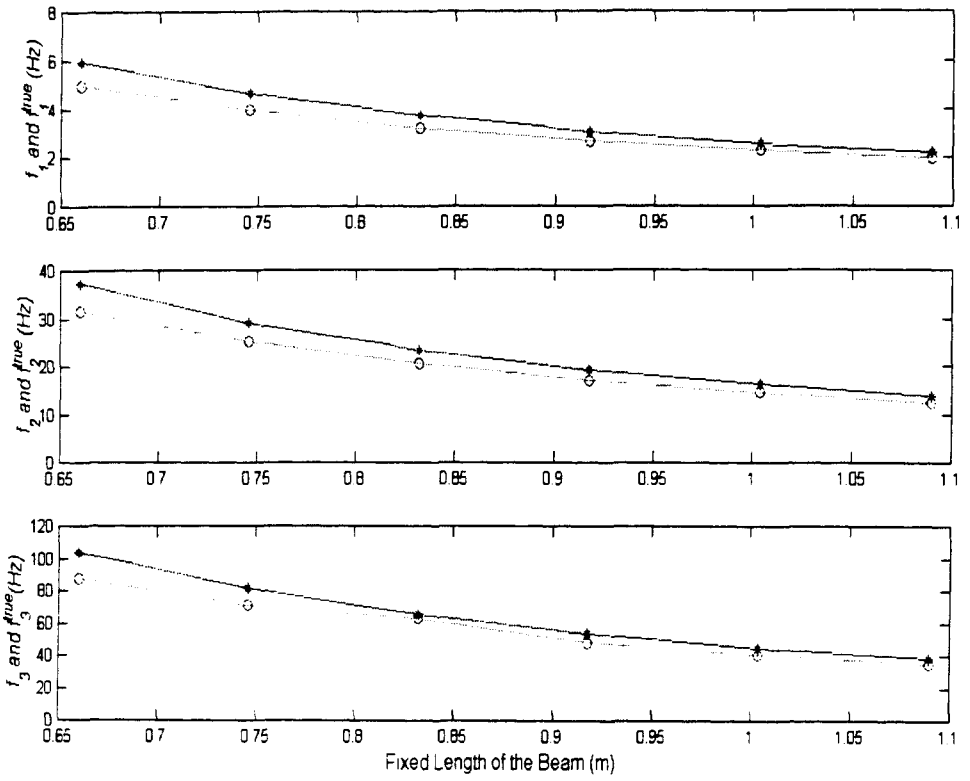

Figure 4.1.2 Comparison of analytical and identified natural frequencies

(2) The identified damping ratios ranges from 0.005 to 0.01. The beam is lightly damped.

(3) The longer the beam length, the more the vibratory modes can be excited while the shorter the beam length, the fewer the vibratory modes are excited.

B. Simulated Responses

The identified model, i.e., $\overline{G}$ and $\overline{C}$ can be used to generate responses. Such responses are referred to as simulated responses. Figure 4.1.3 shows the FFT results of the measured and the simulated responses when the beam is at the shortest length and longest length, respectively. Figure 4.1.4 shows a comparison between the simulated and the measured responses for the

shortest and the longest beam lengths.

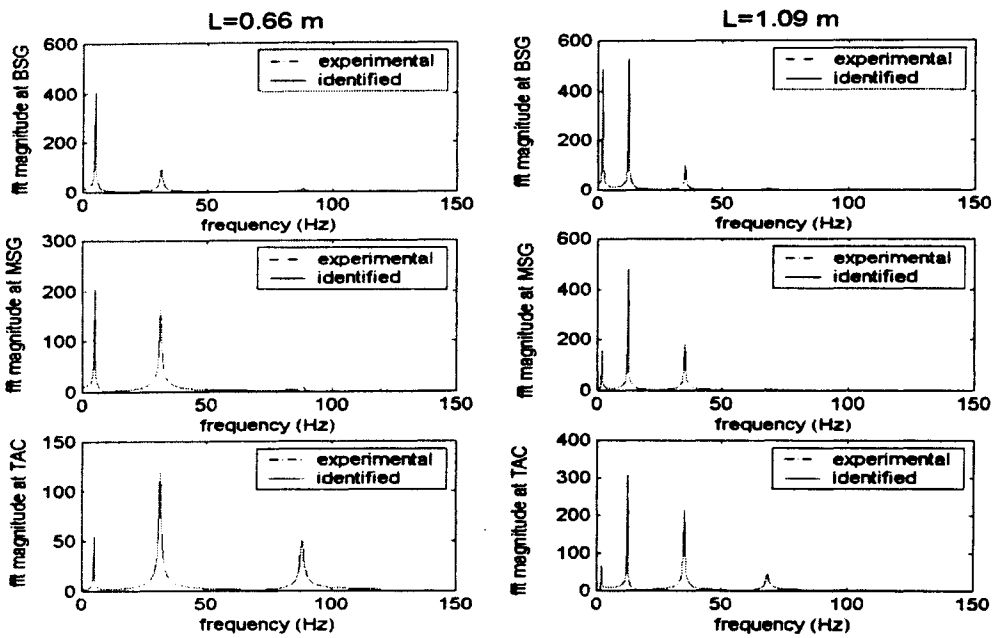

Figure 4.1.3 FFT plots of the transient responses at the three observed positions

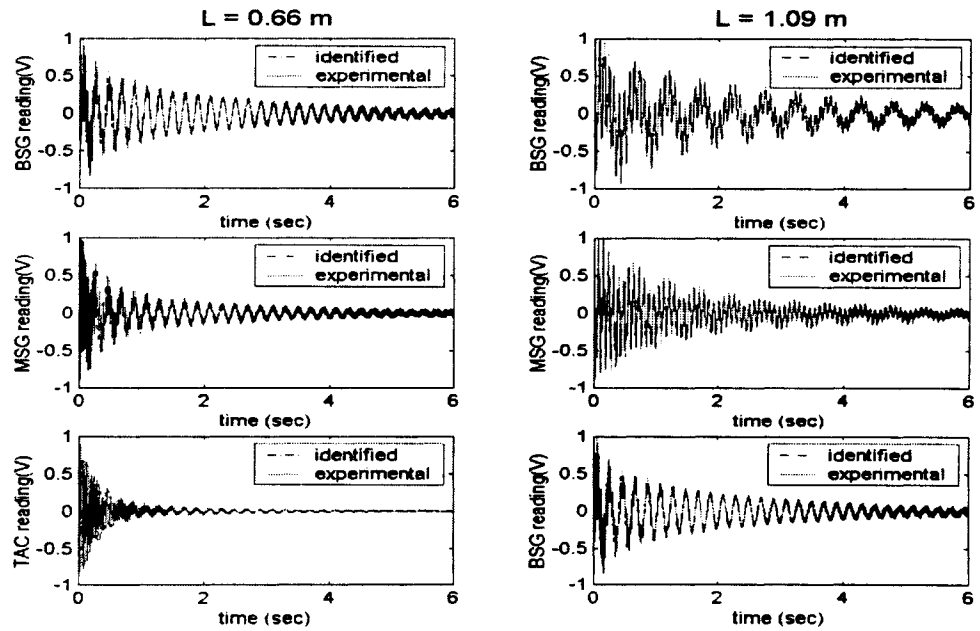

Figure 4.1.4 Comparison between the measured and simulated responses

From these two sets of figures, it can be seen that

(1) At the shortest length, from the BSG and MSG outputs, the first two modes can be observed, but the third mode is very weak. From the TAC output, all the three modes can be observed.

2) At the longest length, from the BSG and MSG outputs, the first three modes can be observed, but the fourth mode is hardly observable. From the TAC output, the first four modes can be observed.

3) The simulated responses agree well with the measured responses. However, there are some phase shifts near the tail of the responses, shown in Figure 4.1.5. It is noted that the solid lines represent the measured responses and the dashdot line represents the simulated responses. The main reason is that the responses near the tails of the data records have a low SNR (signal-to-noise ratio) as the response magnitudes decay toward the end of the data record. The poor SNR responses used in identification result in a large error between the simulated responses and the measured responses.

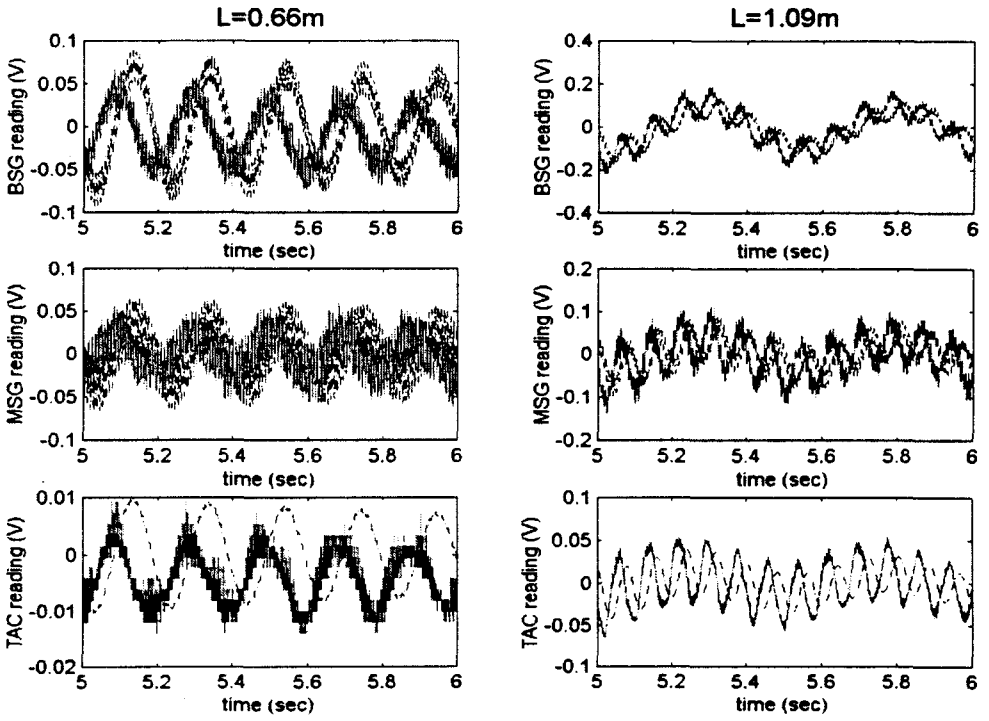

Figure 4.1.5 Responses near the tail of the data records

4.2 Identification Algorithms

4.2.1 Transition Matrix

The discrete-time state space representation of a LTV system subject to an initial condition is given in equation (3-4-1) of subsection 3.4.1. The solution of equation (3-4-1) is given by

$$y(k) = C(k)G(k,0)x(0), \tag{4-2-1}$$

where $G(k,0)$ is the initial state transition matrix. The similarity transformation matrix is no longer constant for the LTV systems. If the non-singular matrices $T(k+1)$ and $T(k)$ exist, the similarity transformation is defined as

$$\overline{G}(k+1,k) = T(k+1)G(k+1,k)T^{-1}(k) \quad \overline{C}(k) = C(k)T^{-1}(k) \tag{4-2-2}$$

where $\overline{G}(k+1,k)$ and $\overline{C}(k)$ represent another realization of the system, $\overline{G}(k+1,k)$ is an $n_x \times n_x$ state transition matrix of another realization of the system, $\overline{C}(k)$ is an $n_y \times n_x$ output matrix of another realization of the system, $T(k+1)$ is an $n_x \times n_x$ transformation matrix at time instant $k+1$, and $T(k)$ is an $n_x \times n_x$ transformation matrix at time instant k. A series of $\overline{G}(k+1,k)$ and $\overline{C}(k)$ can be identified using the algorithm presented in [16] if an ensemble of responses are available. It is noted that $G(k+1,k)$ and $\overline{G}(k+1,k)$ do not share the same eigenvalues. As "pseudo" modal parameters are based on the eigenvalues of the matrix $G(k+1,k)$, identification of the "pseudo" modal parameter presents a challenge. To find the eigenvalues of $G(k+1,k)$, a matrix is defined as

$$\tilde{G}(k+1) = T(k)G(k+1,k)T^{-1}(k) \tag{4-2-3}$$

Thus, $\tilde{G}(k+1,k)$ can guarantee the invariability of the eigenvalues.

Generally, the $\overline{C}(k)$, $\overline{G}(k+1,k)$, and $\tilde{G}(k+1,k)$ cannot be obtained through the data from a single experiment, the identifications of these are conducted by the ensemble method.

4.2.2 Identification of a LTV System Using an Ensemble of Freely Vibrating Responses

It is assumed that N experiments have been conducted on the system whose parameters undergo the same variation. A freely vibrating response vector is denoted by $y^j(k)$, where $j = 1, 2, ...N$ denotes the index of the experiments, $k = 0, 1, 2..., K_s - 1$ denotes time instant k, and K_s is the total length of data.

A general block Hankel matrix is formed using k to $k + M - 1$ successive responses of N experiments, shown as follow

$$H(k) = \begin{bmatrix} y^1(k) & y^2(k) & . \ . \ . & y^N(k) \\ y^1(k+1) & y^2(k) & . \ . \ . & y^N(k+1) \\ . & . & . \ . \ . & . \\ . & . & . \ . \ . & . \\ . & . & . \ . \ . & . \\ y^1(k+M-1) & y^2(k+M-1) & . \ . \ . & y^N(k+M-1) \end{bmatrix}. \qquad (4\text{-}2\text{-}4)$$

The matrix $H(k)$ can be factored as

$$H(k) = \Gamma(k)[x^1(k) \quad x^2(k) \quad x^3(k) \quad ... \quad x^N(k)] \qquad (4\text{-}2\text{-}5)$$

where the observability matrix $\Gamma(k)$ is given as

$$\Gamma(k) = \begin{bmatrix} C(k) \\ C(k+1)G(k+1,k) \\ C(k+2)G(k+2,k) \\ \vdots \\ C(k+M-1)G(k+M-1,k) \end{bmatrix}. \qquad (4\text{-}2\text{-}6)$$

Its corresponding range space becomes

$$\overline{\Gamma}(k) = \Gamma(k)T^{-1}(k) = \begin{bmatrix} \overline{C}(k) \\ \overline{C}(k+1)\overline{G}(k+1,k) \\ \overline{C}(k+2)\overline{G}(k+2,k) \\ \vdots \\ \overline{C}(k+M-1)\overline{G}(k+M-1,k) \end{bmatrix}. \tag{4-2-7}$$

To extract $\overline{G}(k+1,k)$, a successive Hankel matrix $H(k+1)$ is formed using the $k+1$ to $k+M$ successive responses of N experiments. The matrix $H(k+1)$ can be factored as

$$H(k+1) = \Gamma(k+1)[x^1(k+1) \quad x^2(k+1) \quad x^3(k+1) \quad ... \quad x^N(k+1)] \tag{4-2-8}$$

where $\Gamma(k+1)$ has a similar form as equation (4-2-6) and its range space $\overline{\Gamma}(k+1)$ is given by

$$\overline{\Gamma}(k+1) = \Gamma(k+1)T^{-1}(k+1) = \begin{bmatrix} \overline{C}(k+1) \\ \overline{C}(k+2)\overline{G}(k+2,k+1) \\ \overline{C}(k+3)\overline{G}(k+3,k+1) \\ \vdots \\ \overline{C}(k+M)\overline{G}(k+M,k+1) \end{bmatrix}. \tag{4-2-9}$$

Let $\overline{\Gamma}_1(k+1)$ be the first $(M-1)$ block rows of $\overline{\Gamma}(k+1)$, and $\overline{\Gamma}_2(k)$ be the last $(M-1)$ block rows of $\overline{\Gamma}(k)$, i.e.,

$$\overline{\Gamma}_1(k+1) = \begin{bmatrix} \overline{C}(k+1) \\ \overline{C}(k+2)\overline{G}(k+2,k+1) \\ \overline{C}(k+3)\overline{G}(k+3,k+1) \\ \vdots \\ \overline{C}(k+M-1)\overline{G}(k+M-1,k+1) \end{bmatrix} = \Gamma_1(k+1)T^{-1}(k+1) \tag{4-2-10}$$

and

$$\overline{\Gamma}_2(k) = \begin{bmatrix} \overline{C}(k+1)\overline{G}(k+1,k) \\ \overline{C}(k+2)\overline{G}(k+2,k) \\ \overline{C}(k+3)\overline{G}(k+3,k) \\ \vdots \\ \overline{C}(k+M-1)\overline{G}(k+M-1,k) \end{bmatrix} = \Gamma_2(k)T^{-1}(k) \tag{4-2-11}$$

where

$$\Gamma_1(k+1) = \begin{bmatrix} C(k+1) \\ C(k+2)G(k+2,k+1) \\ C(k+3)G(k+3,k+1) \\ \vdots \\ C(k+M-1)G(k+M-1,k+1) \end{bmatrix} \tag{4-2-12}$$

and

$$\Gamma_2(k) = \begin{bmatrix} C(k+1)G(k+1,k) \\ C(k+2)G(k+2,k) \\ C(k+3)G(k+3,k) \\ \vdots \\ C(k+M-1)G(k+M-1,k) \end{bmatrix}. \tag{4-2-13}$$

Thus, the matrix $\overline{G}(k+1,k)$ can be found by

$$\overline{G}(k+1,k) = [\overline{\Gamma}_1(k+1)]^+\overline{\Gamma}_2(k). \tag{4-2-14}$$

In computation, the range space matrices $\overline{\Gamma}(k)$ and $\overline{\Gamma}(k+1)$ are extracted by the SVD of $H(k)$ and $H(k+1)$, i.e.,

$$H(k) = U(k)\Sigma(k)V(k)^T \text{ and } H(k+1) = U(k+1)\Sigma(k+1)V(k+1)^T. \tag{4-2-15}$$

Let $U_{n_x}(k)$ be the first n_x columns of $U(k)$ and $U_{n_x}(k+1)$ the first n_x columns of $U(k+1)$. Use the first $(M-1)$ block rows of $U_{n_x}(k+1)$ as $U_{n_x1}(k+1)$ and the last $(M-1)$ block rows

of $U_{n_x}(k)$ as $U_{n_x 2}(k)$. Invoking equation (4-2-14) results in

$$\overline{G}(k+1,k) = [U_{n_x 1}(k+1)]^{+} U_{n_x 2}(k) = T(k+1)G(k+1,k)T^{-1}(k) \ . \tag{4-2-16}$$

However, since $T(k+1)$ and $T(k)$ are unavailable, the exact solution of $\widetilde{G}(k+1,k)$ cannot be found. An approximate solution for $\widetilde{G}(k+1,k)$ is proposed in [16]. In this study, an alternative solution is used. Instead of forming $U_{n_x 1}(k+1)$ using the first $(M-1)$ block rows of $U_{n_x}(k+1)$, let $U_{n_x 1}(k)$ be the first $(M-1)$ block rows of $U_{n_x}(k)$. Note that

$$U_{n_x 1}(k) = \Gamma_1(k)T^{-1}(k) \quad \text{and} \quad U_{n_x 2}(k) = \Gamma_2(k)T^{-1}(k) \tag{4-2-17}$$

where

$$\Gamma_1(k) = \begin{bmatrix} C(k) \\ C(k+1)G(k+1,k) \\ \vdots \\ C(k+M-2)G(k+M-2,k) \end{bmatrix} \tag{4-2-18}$$

and

$$\Gamma_2(k) = \begin{bmatrix} C(k+1) \\ C(k+2)G(k+2,k+1). \\ \vdots \\ C(k+M-1)G(k+M-1,k+1) \end{bmatrix} G(k+1,k). \tag{4-2-18}$$

The following relation exists

$$\begin{aligned} \widehat{G}(k+1,k) &= [U_{n_x 1}(k)]^{+} U_{n_x 2}(k) = [U_{n_x 1}^T(k)U_{n_x 1}(k)]^{-1} U_{n_x 1}^T(k)U_{n_x 2}(k) \\ &= [T^{-T}(k)\Gamma_1^T(k)\Gamma_1(k)T^{-1}(k)]^{-1} T^{-T}(k)\Gamma_1^T(k)\Gamma_2^T(k)T^{-1}(k) \\ &= T(k)W_1^{-1}(k)W_2(k)G(k+1,k)T^{-1}(k) \end{aligned} \tag{4-2-19}$$

where

$$W_1(k) = \Gamma_1^T(k)\Gamma_1(k) = \left[\sum_{j=1}^{M-1} G^T(k+j-1,k)C^T(k+j-1)C(k+j-1)G(k+j-1,k)\right] \tag{4-2-20}$$

and

$$W_2(k) = \left[\sum_{j=1}^{M-1} G^T(k+j-1,k) C^T(k+j-1) C(k+j) G(k+j-1,k+1) \right]. \qquad (4\text{-}2\text{-}21)$$

If the system variation from moment k to moment $k+1$ is small, i.e., $C(k)$ is close to $C(k+1)$ and $G(k+1,k)$ close to $G(k+2,k+1)$, $W_1(k)$ is close to $W_2(k)$ or $W_1^{-1}(k)W_2(k) \approx \mathbf{I}$. Therefore, an approximate solution of $\widetilde{G}(k+1,k)$ is given by

$$\widetilde{G}(k+1,k) \approx \widehat{G}(k+1,k). \qquad (4\text{-}2\text{-}22)$$

4.2.3 Computational Procedure for the Identification algorithm

To identify $\overline{C}(k), \overline{G}(k+1,k)$ and $\widetilde{G}(k+1,k)$, $k = 1,2,3..., K_s - M - 1$;

1. Form $H(k)$. Conduct the SVD on $H(k)$ to obtain $U(k)$. Form $U_{n_x}(k)$ by using the first n_x columns of $U(k)$;

2. Form $U_{n_x 2}(k)$, $U_{n_x 1}(k)$ by retaining the last $(M-1)$ block rows of $U_{n_x}(k)$ and the first $(M-1)$ block rows of $U_{n_x}(k)$. Form $\overline{C}(k)$ by retaining the first block row of $U_{n_x}(k)$;

3. Obtain $\widehat{G}(k+1,k)$ by using equation (4-2-19);

4. Form $H(k+1)$. Conduct the SVD on $H(k+1)$ to obtain $U(k+1)$. Form $U_{n_x}(k+1)$ by extracting the first n_x columns of the $U(k+1)$. Form $U_{n_x 1}(k+1)$ by retaining the first $(M-1)$ block row of $U(k+1)$;

5. Substitute $U_{n_x 2}(k)$ and $U_{n_x 1}(k+1)$ into equation (4-2-16) to obtain $\overline{G}(k+1,k)$;

6. $U_{n_x}(k+1)$ in $U_{n_x}(k)$. If $k < K_s - M + 1$, increase k by 1 and go to step 2.

4.2.4 Identified "Pseudo" Modal Parameters

The matrix $W_1^{-1}(k)W_2(k)G(k+1,k)$ can be used to evaluate a set of identified "pseudo" modal parameters. The eigendecomposition of the matrix is given as

$$\widehat{G}(k+1,k) = \widehat{\Psi}(k)\widehat{\Lambda}(k)\widehat{\Psi}^{-1}(k) \qquad (4\text{-}2\text{-}23)$$

where $\widehat{\Psi}(k)$ is defined as an identified "pseudo" eigenvector matrix and $\widehat{\Lambda}(k)$ an identified "pseudo" eigenvalue matrix formed by

$$\widehat{\Lambda}(k) = \mathbf{diag}\ [\widehat{\lambda}_1(k),\ \widehat{\lambda}_2(k), ..., \widehat{\lambda}_{n_x}(k)]. \tag{4-2-24}$$

Since the elements of $G(k+1,k)$ are real, the complex eigenvalues occur in pairs. If the ith eigenvalue is complex, then the following relation can be used

$$\widehat{\lambda}_i(k) = \widehat{\lambda}^*_{i+n_x/2}(k) = \exp\left[\left(-\widehat{\zeta}_i(k)\widehat{\omega}_i(k) + j\widehat{\omega}_i(k)\sqrt{1-(\widehat{\zeta}_i(k))^2}\right)\Delta t\right] \tag{4-3-25}$$

where $\widehat{\zeta}_i(k)$ and $\widehat{\omega}_i(k)$ are defined as the ith identified "pseudo" damping ratio and the ith identified "pseudo" natural frequency, respectively.

4.3 Comparison of the True and Identified "Pseudo" Modal Parameters

To compare the modal parameters based on eigendecomposition of $W_1^{-1}(k)W_2(k)G(k+1,k)$ or $\widehat{G}(k+1,k)$ and those based on eigendecomposition of $G(k+1,k)$ or $\widetilde{G}(k+1,k)$, the analytical model developed in the previous chapter is used to compute these modal parameters numerically. Again, two motion scenarios are considered, namely scenario A: axial extension in which the beam length varies from $L_{\min}$ to $L_{\max}$ and scenario B: axial retraction in which the beam length varies from $L_{\max}$ to $L_{\min}$. The values of $L_{\max}$ to $L_{\min}$ are the same as those in chapter 3. The trapezoid velocity profiles are also used as the axial motion profiles. Two strain outputs, namely BSG and MSG whose axial locations with respect to the tip of the beam are 0.643 m and 0.335 m respectively are used. The system order n_x is 6. A series of the matrices $G(k+1,k)$ are computed using an ensemble of n_x sets of states that are generated randomly. A series of the matrices $C(k)$ can be determined in equation (3-2-3-3) according to the prespecified axial motion profiles and strain sensor locations with respect to the tip of the beam. Thus, the matrices $W_1(k)$ and $W_2(k)$ can be found. Figures 4.3.1 and 4.3.2 show a comparison of the true "pseudo" modal parameters and identified "pseudo" ones for scenario A and scenario B, respectively. In computation of $\widehat{G}(k+1,k)$, the block row number $M = 35n_x = 210$ is used. It

is noted that solid lines represent identified "pseudo" modal parameters and dashed lines the true "pseudo" modal parameters.

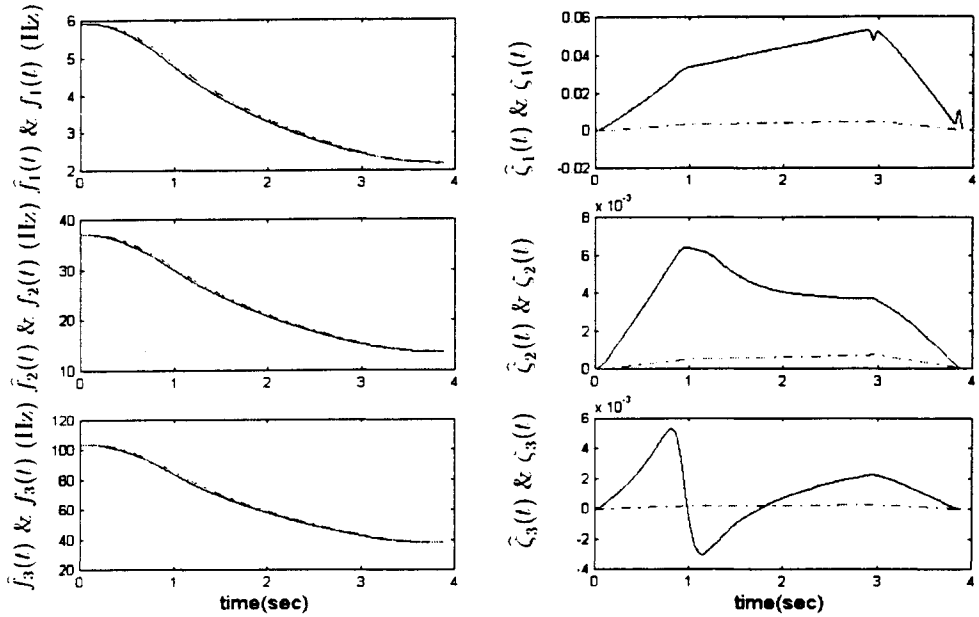

Figure 4.3.1 Compariosn of the true and identified "pseudo" modal parameters under scenario A

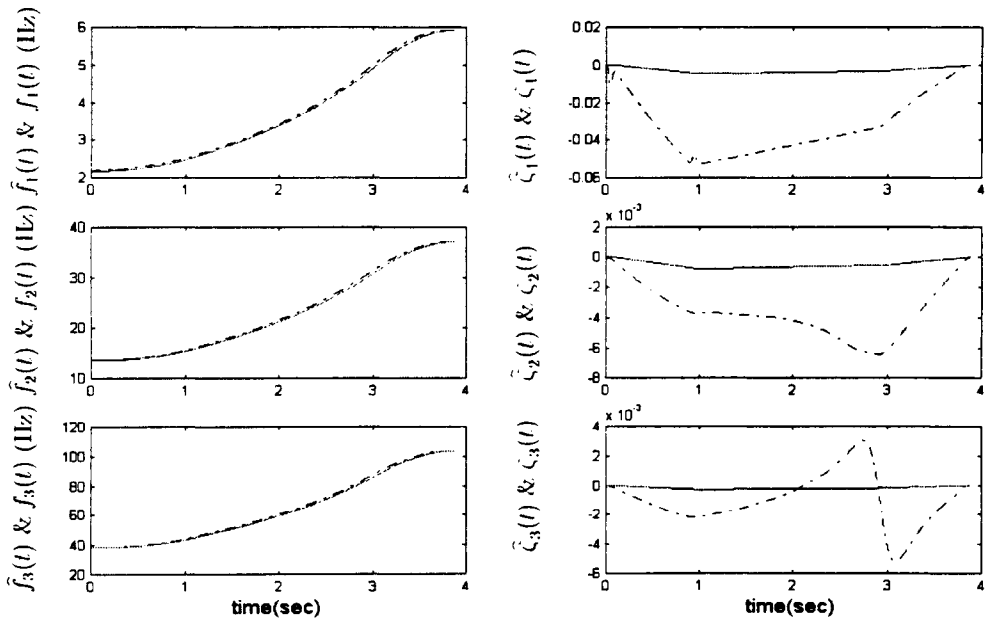

Figure 4.3.2 Comparison of the true and identified "pseudo" modal parameters under scenario B

It can be seen that the identified "pseudo" natural frequencies agree with the true values well and the identified "pseudo" damping ratios deviate from the true values significantly.

A natural question is how the choice of M affects the "pseudo" modal parameters. To evaluate the closeness between the identified "pseudo" modal parameters and true ones, two dimensionless root-mean-square (RMS) error indices are defined as

$$\begin{aligned} \delta_{f_i} &= \sqrt{\frac{\sum_{k=1}^{K_s}\left[f_i(k)-\widehat{f}_i(k)\right]^2}{\sum_{k=1}^{K_s} f_i^2(k)}} \\ \delta_{\zeta_i} &= \sqrt{\frac{\sum_{k=1}^{K_s}\left[\zeta_i(k)-\widehat{\zeta}_i(k)\right]^2}{\sum_{k=1}^{K_s} \zeta_i(k)^2}} \qquad i=1,2,...,n_x/2 \end{aligned} \tag{4-3-1}$$

where δ_{f_i} and δ_{ζ_i} are the RMS error indices of the ith natural frequency and damping ratio respectively, $f_i(k)$ and $\widehat{f}_i(k)$ are the ith true "pseudo" natural frequency and identified "pseudo" one, $\zeta_i(k)$ and $\widehat{\zeta}_i(k)$ are the ith true "pseudo" damping ratio and identified "pseudo" one. Then, two overall indices are defined as

$$\delta_f = \frac{2}{n_x}\sum_{i=1}^{n_x/2}\delta_{f_i} \text{ and } \quad \delta_\zeta = \frac{2}{n_x}\sum_{i=1}^{n_x/2}\delta_{\zeta_i} \tag{4-3-2}$$

where δ_f and δ_ζ are the RMS error indices of the natural frequencies and damping ratios respectively.

Figure 4.3.3 shows the relationship between the defined error indices and M. It can be seen that, for the "pseudo" natural frequencies, the errors between approximate values and the true ones increase with an increase of M; for the "pseudo" damping ratios, the errors between the identified values and the true one decrease with an increase of M. It should be pointed out that the errors between the identified "pseudo" damping ratios and true values are much greater that the errors between the identified "pseudo" natural frequencies and true values. This indicates that the matrix $\widehat{G}(k+1,k)$ can give a good estimate of the "pseudo" natural frequencies, but it cannot give a meaningful estimate of the "pseudo" damping ratios. It seems that the "pseudo"

damping ratios are more sensitive to the modification on the matrix $G(k+1,k)$ caused by the term $W_1^{-1}(k)W_2(k)$ than the "pseudo" natural frequencies.

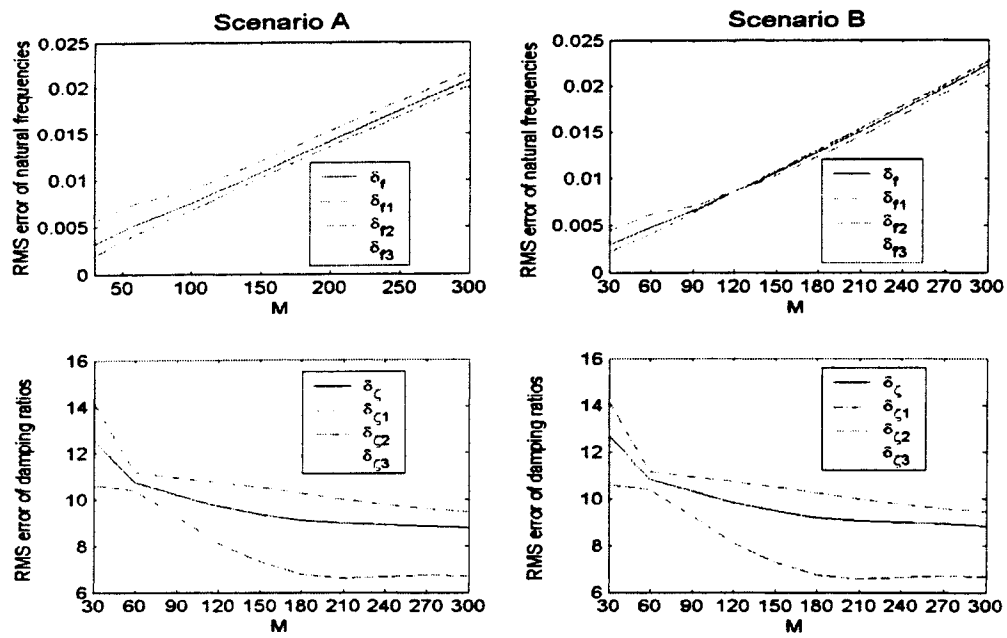

Figure 4.3.3 Relationship between RMS error indices of modal parameters and varying M

4.4 Experimental Identification of the System

This section presents the experimental identification results conducted on the axially-moving cantilever beam apparatus. The experimental setup is shown in Figure 4.4.1.

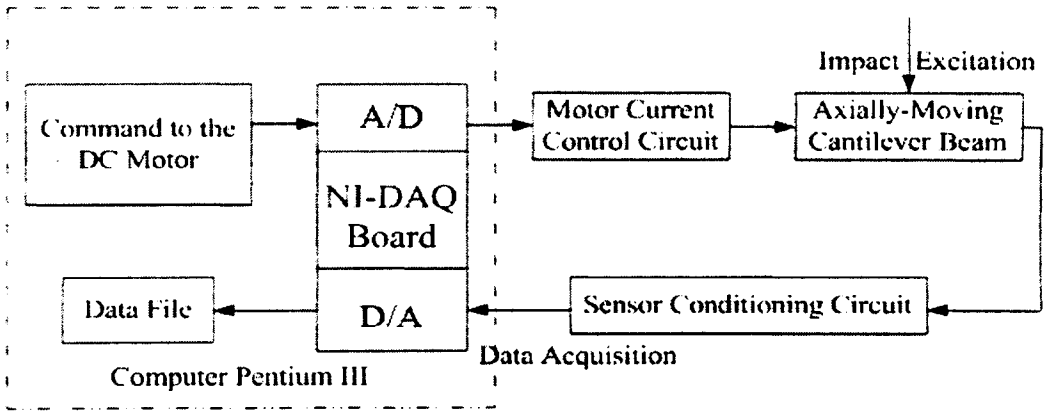

Figure 4.4.1 The experimental setup

Once again, two motion scenarios are considered, namely, scenario A: axial extension and scenario B: axial retraction. To command the DC motor to accomplish the desired axial motion scenarios, a DC motor control strategy needs to be chosen. To this end, the relationship between the command voltage generated by the DAQ board and the motor current was examined by connecting an ampere meter in series to the DC motor and applying a constant voltage input to the motor current control circuit. Thus, the relationship between the command voltage and motor current can be obtained and listed in Table 4.2.

Table 4.2 Relationship between command voltage and motor current

Scenario A		Scenario B	
Command voltage(V)	Peak/Steady motor current (A)	Command voltage (V)	Peak/Steady motor current (A)
0.5	- 0.245 / 0.245	-0.5	0.248 / 0.248
1.0	-0.486 / 0.486	-1.0	0.495 / 0.495
1.5	-0.712 / 0.712	-1.5	0.743 / 0.743
2.0	-0.992 / 0.992	-2.0	1.014 / 1.014
2.5	-1.211 / 1.211	-2.5	1.235 / 1.235
3.0	-1.463 / 1.463	-3.0	1.485 / 1.485
3.5	-1.657 / 1.525	-3.5	1.701 / 1.520
4.0	-1.943 / 1.520	-4.0	1.975 / 1.525
4.5	-2.113 / 1.522	-4.5	2.210 / 1.523
5.0	-2.313 / 1.518	-5.0	2.342 / 1.519
5.5	-2.454 / 1.526	-5.5	2.473 / 1.516
6.0	-2.792 / 1.525	-6.0	2.682 / 1.525
6.5	-2.962 / 1.523	-6.5	3.023 / 1.523
7.0	-3.145 / 1.522	-7.0	3.203 / 1.521

It is noted that a proportional relationship exists between the voltage and the steady current up to 3V. A further increase in the applied voltage does not result in an increase in the steady motor current. However, it was observed that when a voltage greater than 3V was applied, the

motor current had a short-time surge and then quickly settled down at the steady value. Such a surge in the motor current did result in a fast acceleration motion of the motor. It was desired to use two motion speeds in the test. For the fast motion, it is desired that the beam completes its motions in about 4.3 seconds in both scenarios. For the slow motion, the beam completes its motions in about 9 seconds in both scenarios. After trial-and-error tests, a two-step control strategy was employed. The command voltages used are shown in Figure 4.4.2.

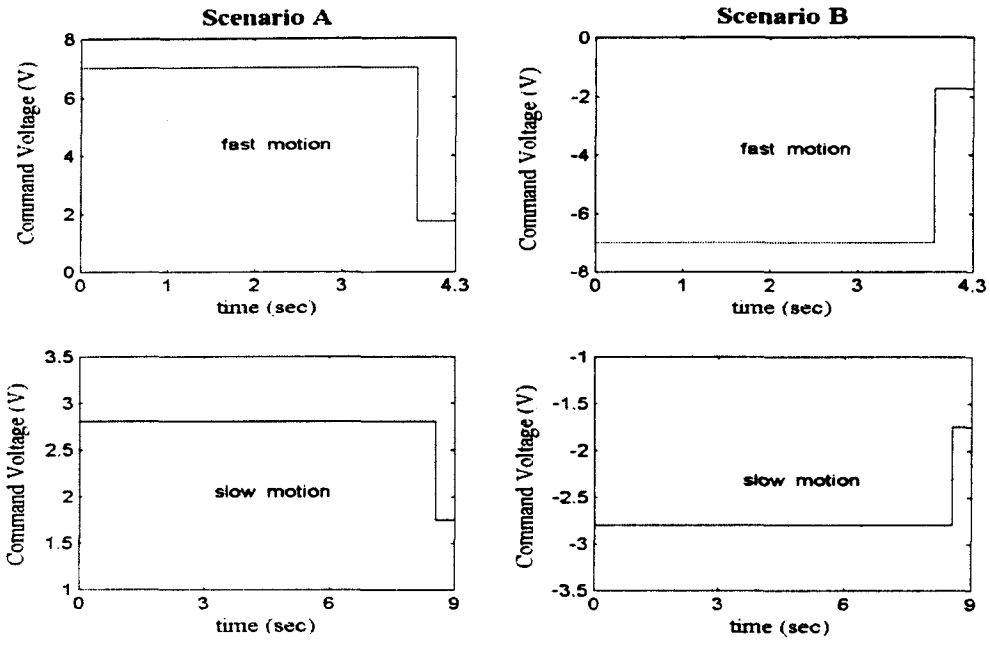

Figure 4.4.2 Command voltage profiles

For scenario A of the fast motion, a voltage of 7V is applied first until the pot voltage reaches 4.3V and then a voltage of 1.5V is applied until the maximum beam length is obtained. For scenario B of the fast motion, a voltage command of -7V is applied first until the pot voltage reaches -4.3V, and then a voltage of -1.5V is applied until the minimum beam length is obtained. For scenario A of the slow motion, a voltage of 2.8V is applied first until the pot voltage reaches 4.3V and then a voltage of 1.75V is applied until the maximum is obtained. For scenario B of the slow motion, a voltage of -2.8V is applied first until the pot voltage reaches -4.3V and then a voltage of -1.75V is applied until the minimum beam length is obtained. A Labview program was used to execute such commands and collect data. Figure 4.4.3 shows the pot signal profiles

obtained by such commands.

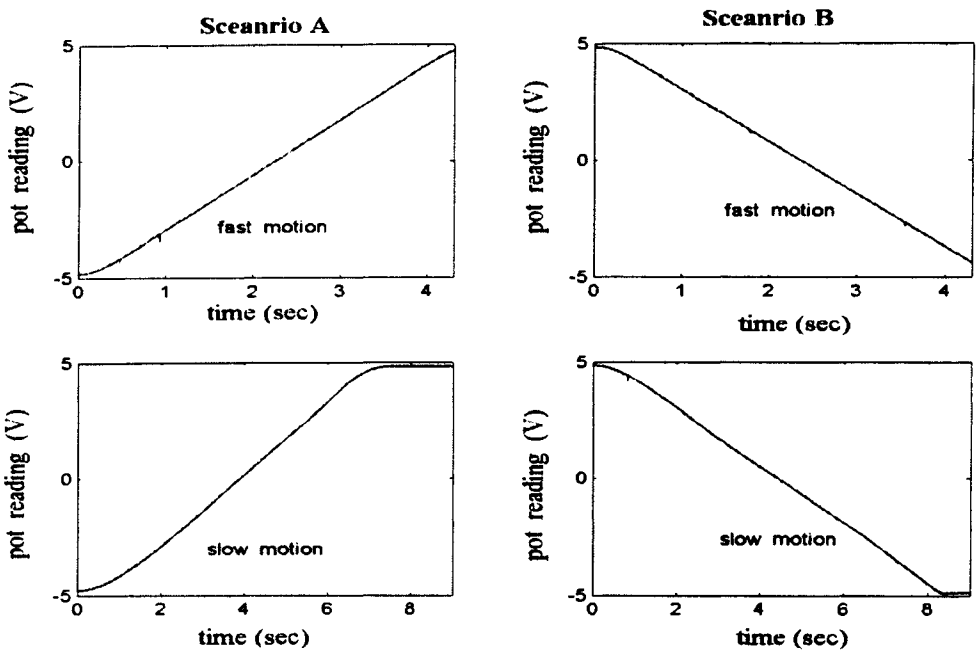

Figure 4.4.3 Pot signal profiles

Three sensors were used. They are the base strain gauge (BSG) sensor located at 0.643 m, the middle accelerometer (MAC) located at 0.335 m, and the tip accelerometer (TAC) located at 0.004 m. All the sensor locations are measured with respect to the tip of the beam.

The accuracy of an identified model is measured by several dimensionless RMS error indices. The indices are defined by comparing the measured responses with simulated responses generated by an identified model $\overline{G}(k+1,k)$ and $\overline{C}(k)$. The closeness between the ith measured response $\widetilde{y}_i^j(k)$ from the jth experiment and its simulated counterpart $\widehat{y}_i^j(k)$ is measured by

$$\delta_i^j = \sqrt{\frac{\sum_{k=1}^{K_s}\left[\widetilde{y}_i^j(k)-\widehat{y}_i^j(k)\right]^2}{\sum_{k=1}^{K_s}\left[\widetilde{y}_i^j(k)\right]^2}},\ i=1,2,\cdots,n_y,\ j=1,2,\cdots N \qquad (4\text{-}4\text{-}1)$$

The closeness between all the measured responses from the jth experiment $\widetilde{y}^j$ and their simu-

lated counterpart $\widehat{y}^j$ is measured by

$$\delta^j = \frac{1}{n_y} \sum_{i=1}^{n_y} \delta_i^j. \tag{4-4-2}$$

The closeness between the ith measured response from all the experiments and their simulated counterparts is measured by

$$\delta_i = \frac{1}{N} \sum_{j=1}^{N} \delta_i^j \tag{4-4-3}$$

where δ_1 denotes the overall measure using the BSG response, δ_2 overall measure using the MAC response, and δ_3 overall measure using TAC response. An overall measure using the total measurement is defined as

$$\delta = \frac{1}{N} \sum_{j=1}^{N} \delta^j. \tag{4-4-4}$$

To generate an ensemble of freely vibrating responses, a proper initial excitation to the beam is very critical. A suitable excitation must excite the system dynamics fully and ensure the responses of current experiment to be independent of the previous ones. Each excitation was produced by tapping the beam at a different location with a different magnitude of force in the two different directions. After the beam was tapped, the Labview program was executed to start the beam motion and the responses of each experiment were displayed and visually examined to determine the suitability of the data.

Numerous experiments were conducted. In what follows, forty experiments are considered for each combination of the motion speeds and the motion scenarios. The data acquired during the experiment are referred to as original ensemble data.

The rest of the section is organized as follows. First, the identification results using original ensemble data are presented in order to estimate the system order n_x, to understand some factors influencing the model accuracy. An ensemble of the responses data of twenty experiments is selected from the original data of the forty experiments in order to reduce the computational time and to improve model accuracies. Second, using the selected ensemble data, the relationship between the system order n_x and the RMS error index are presented in order to understand how the system order n_x affects the model accuracy, and the relationship between the block row number M and model accuracy are also given in order to understand how M

affects the model accuracy. Meanwhile, the comparison between the simulated responses and the measured ones are presented.

4.4.1 Identification Results Using the Original Ensemble Data

The identified model accuracies are influenced by the quality and independency of the measured responses, as well as the used model order n_x and block row number M [16]. Due to the fact that the measured outputs are contaminated by noise or may be affected by the system nonlinearity, the identified model should be overparameterized in order to catch the dynamics of the system [24, 25]. In what follows, using the original ensemble data, first, the variation of singular values obtained by the eigendecomposition of the Hankel matrix in (4-2-4) are discussed for each combination of the motion scenarios and motion speeds, and a proper model order n_x can be estimated; Second, the model accuracies are calculated using the estimated model order for various combinations of outputs used.

The singular values at time instant k are defined based on the SVD (singular value decomposition) of Hankel matrix $H(k)$ in (4-2-15), i.e.,

$$H(k) = U(k)\Sigma(k)V^T(k) \qquad k = 0, 1, \cdots K_s - M - 1 \tag{4-4-1}$$

where $U(k)$ is an $n_xM \times n_xM$ left singular vector matrix , $V(k)$ is an $N \times N$ right singular vector matrix. $\Sigma(k)$ is an $n_xM \times N$ matrix and can be partitioned as

$$\Sigma(k) = \begin{bmatrix} [\Sigma_N(k)]_{N\times N} \\ \mathbf{0}_{(n_xM-N)\times N} \end{bmatrix} \tag{4-4-2}$$

where $\Sigma_N(k) = \text{diag}\ (\sigma_1(k), \sigma_2(k), \cdots, \sigma_N(k))$ with $\sigma_1(k) \geqslant \sigma_2(k) \geqslant \cdots \geqslant \sigma_N(k) \geqslant 0$. The number $\sigma_i(k)$ is called the ith singular value at time instant k. Since the singular values are varying, the average of the ith singular values $\sigma_i(k)$ ranging from $(1 \leqslant k \leqslant K_s - M - 1)$ is used to describe its variation for the time-varying process of the system and defined as

$$\sigma_m^i = \frac{1}{K_s - M - 1} \sum_{k=1}^{K_s-M-1} \sigma_i(k) \tag{4-4-3}$$

Figure 4.4.4 shows the variations of all singular values for each combination of the two motion speeds and scenarios. Figure 4.4.5 shows the comparisons of the first twenty singular values at time instant $t = 0$ (sec), $t = 2$ (sec), $t = 4$ (sec) and their averages for fast motion, at time instant $t = 0$ (sec), $t = 4.5$ (sec), $t = 8.9$ (sec) and their averages for slow motion, for axial extension and retraction.

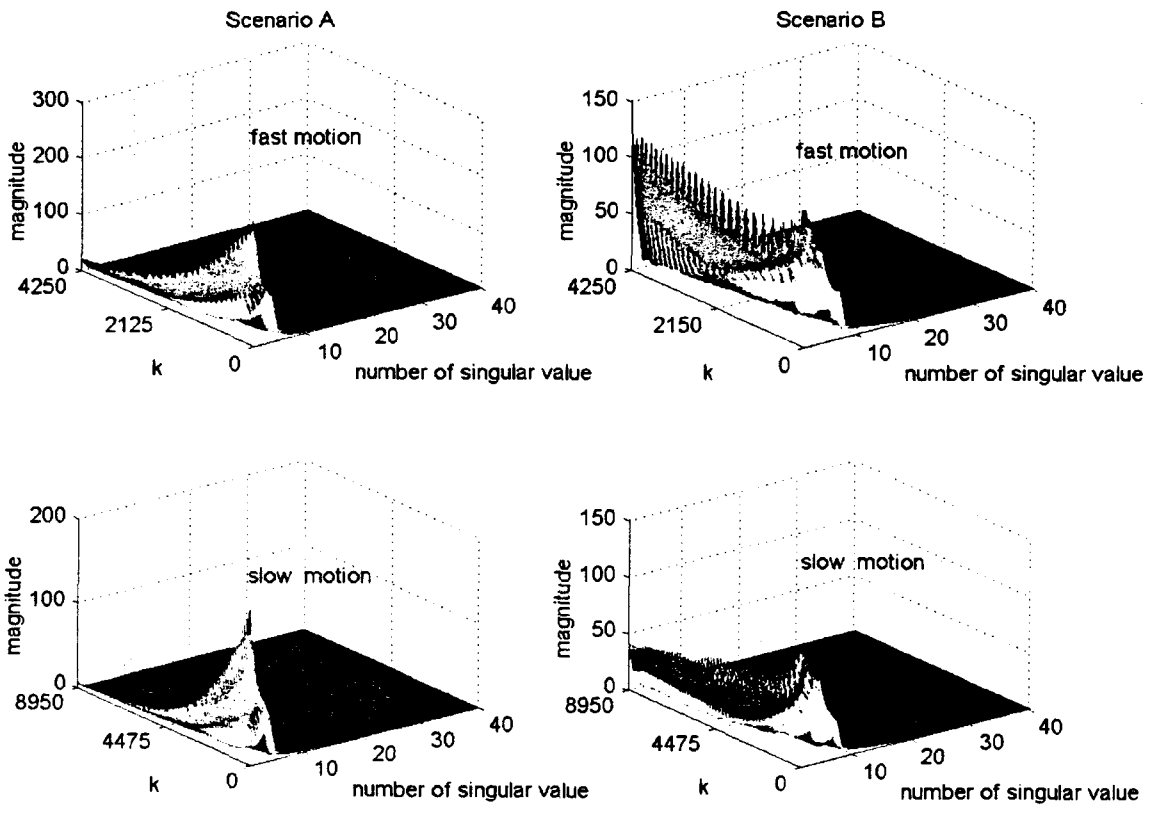

Figure 4.4.4 The singular values for each combination of the motion scenarios and speeds

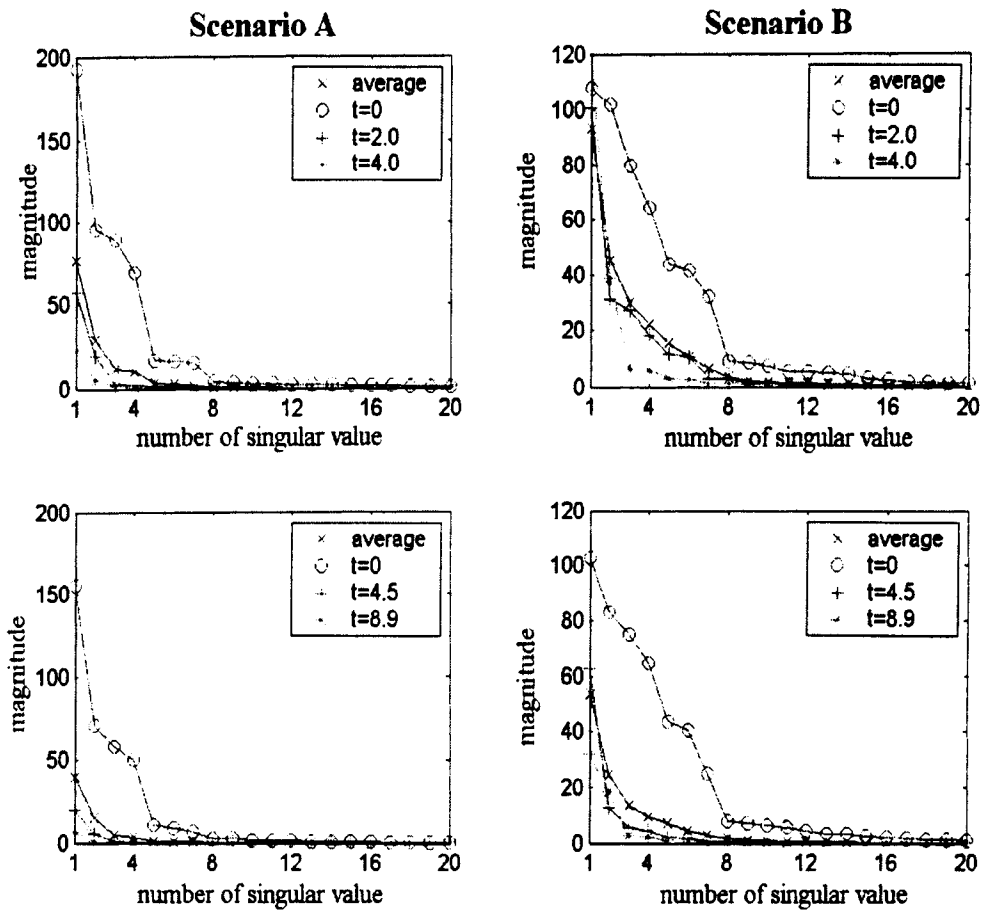

Figure 4.4.5 Comparison of the first twenty singular values at different time instants and average

Obviously, the motion speeds and the motion scenarios affect the variations of singular values. The magnitudes of singular values become small as the beam becomes longer. The singular values for axial extension decrease much faster than those for axial retraction. This indicates that the magnitudes of the modes present in the responses of axial extension reduces faster than those in the responses of axial retractoin toward the end of the axial motion. They reveal that the fewer modes are present in the responses of axial extension than in the responses of axial retraction. Figure 4.4.6 shows the comparison of the first twenty average singular values between scenarios A and B for the two motion speeds. Figure 4.4.7 shows the comparison of magnitudes of the first twenty average singular values between the fast motion and slow motion

under scenarios A and B.

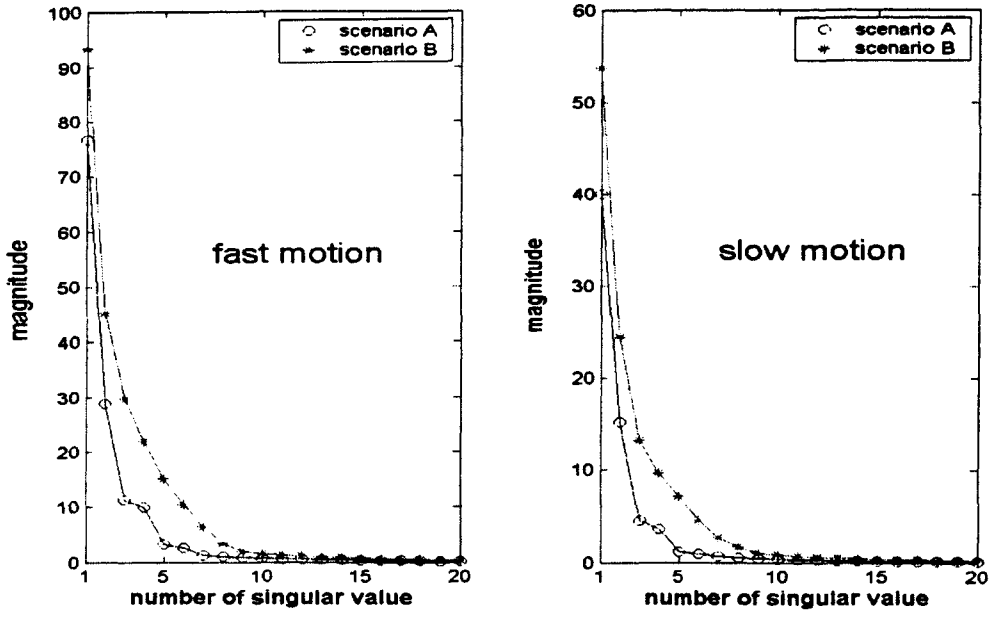

Figure 4.4.6 Comparison of the first twenty average singular values between scenarios A and B

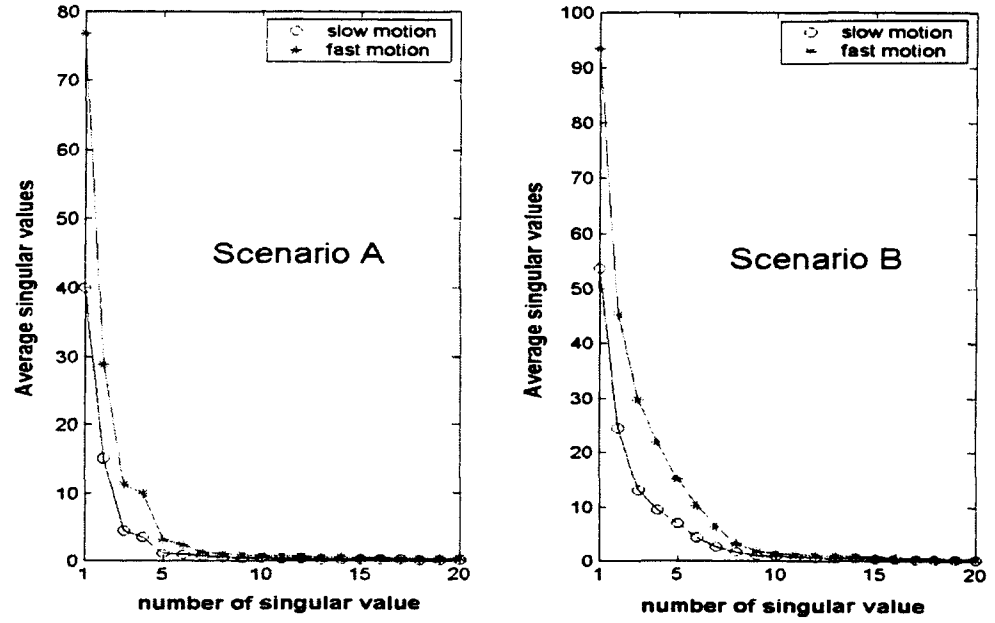

Figure 4.4.7 Comparison of the first twenty average singular values between two motion speeds

From Figures 4.4.6 and 4.4.7, it can also be seen that

1. On the average, the magnitudes of the singular values corresponding to scenario A are smaller than those corresponding to scenario B for slow and fast motion, which indicates that the effects of the vibratory modes in the responses under scenario A are weaker than those under scenario B.

2. On the average, the mangitudes of the singular values corresponding to the slow motion are smaller than those corresponding to the fast motion, which indicates that the effects of vibratory modes in the responses under the slow motion are weaker than those under the fast motion for the two motion scenarios.

However, for all combinations of the two motion speeds and the two scenarios, their model orders are estimated to be $n_x = 14$ because all the rest of the singular values are sufficiently small during the axial motion. Meanwhile, to guarantee a full rank of the Hankel matrix, the block number M must be greater than the upper bound of the system order n_x [16]. Thus, $n_x = 14$ and $M = 50$ are chosen in the following analysis.

Using the original ensemble data, the identification computation was conducted for various situations. Table 4.3 lists the overall RMS error indices δ. Table 4.4 lists the RMS error indices

δ_i based on individual responses.

Table 4.3 RMS error δ for the models identified using the original ensemble data

Output used	Fast motion in scenario A	Slow motion in scenario A	Fast motion in scenario B	Slow motion in scenario B
BSG, MAC, TAC	0.2570	0.3769	0.3287	0.4962
BSG, MAC	0.2466	0.3790	0.3123	0.5386
MAC, TAC	0.2910	0.3880	0.5020	0.4749
BSG, TAC	0.2494	0.3536	0.4643	0.5587
BSG	0.3122	0.3615	0.6479	0.7541
MAC	0.5236	0.4517	0.6155	0.5702
TAC	0.5223	0.3737	0.5398	0.4933

Table 4.4 RMS error δ_i for the models identified using the original ensemble data

Output used	index	Fast motion in scenario A	Slow motion in scenario A	Fast motion in scenario B	Slow motion in scenario B
BSG, MAC, TAC	δ_1	0.1971	0.3497	0.2959	0.6324
	δ_2	0.2977	0.4189	0.3635	0.4347
	δ_3	0.2762	0.3620	0.3568	0.4214
BSG, MAC	δ_1	0.1973	0.3455	0.2631	0.6391
	δ_2	0.2959	0.4126	0.3616	0.4381
MAC, TAC	δ_2	0.3012	0.4145	0.5229	0.4945
	δ_3	0.2808	0.3615	0.4811	0.4554
BSG, TAC	δ_1	0.2144	0.3471	0.5263	0.6909
	δ_3	0.2845	0.3602	0.4022	0.4266
BSG	δ_1	0.3122	0.3615	0.6479	0.7541
MAC	δ_2	0.5236	0.4517	0.6155	0.5702
TAC	δ_3	0.5223	0.3737	0.5398	0.4933

Based on the Table 4.3 and Table 4.4, the following observation can be drawn.

1. The models identified using more than one response have a better accuracy than those identified using only one response. It may be explained that the independencies of Hankel matrix formed using only one response are poorer than those of Hankel matrix formed

using more than one response. Thus, the models identified using only one responses cannot represents the sensible models of the system.

2. Under the condition of using more than one response, the models identified using the data of scenario A have a better accuracy than those identified using the data of scenario B.

3. Under the condition of using more than one response, the models identified using the data of the fast motion have better model accuracies than those identified using the data of slow motion. It may be explained that the models identified using the data of the fast motion have lower accumulative errors between the measured responses and the simulated ones than models identified using the data of the slow motion.

4.4.2 Identification Results Using the Selected Ensemble Data

The identification computation is very time-consuming as it deals with the singular value decomposition of two successive Hankel matrices. The most effective way to reduce the computational time is to reduce the experimental number N or the column number of the Hankel matrix. The number N must be greater than the model order n_x. Based on a prior knowledge on the system dynamics and the plots of the average singular values presented in earlier subsection, a number of 20 was considered to be a proper choice for the number of experiments. The selection of 20 sets of the responses from 40 sets of the original responses was done in the following way. The indices δ^j were arranged in an ascending order. The experimental data sets corresponding to the first 20 δ^j indices were selected for further identification. The data set arranged in the ascending order of the first 20 δ^j indices is referred to as selected ensemble data.

Using this selected ensemble data, the same model order n_x and block row number M, the models were reidentified. The results are given in Table 4.5 and Table 4.6. As expected, the model accuracies are greatly improved. It may be explained that the qualities and independency of the measured responses from the selected ensemble data are better than those obtained from

the original ensemble data.

Table 4.5 RMS error δ for the models identified using the selected ensemble data

Output used	Fast motion in scenario A	Slow motion in scenario A	Fast motion in scenario B	Slow motion in scenario B
BSG, MAC, TAC	0.1583	0.2680	0.2582	0.3337
BSG, MAC	0.1374	0.2491	0.2387	0.3635
MAC, TAC	0.1905	0.2635	0.2617	0.3332
BSG, TAC	0.1443	0.2293	0.2350	0.3961
BSG	0.1069	0.2020	0.4075	0.5985
MAC	0.2479	0.3254	0.4058	0.4042
TAC	0.2097	0.2595	0.3680	0.3640

Table 4.6 RMS error δ_i for the models identified using the selected ensemble data

Output used	index	Fast motion in scenario A	Slow motion in scenario A	Fast motion in scenario B	Slow motion in scenario B
BSG, MAC, TAC	δ_1	0.0944	0.2139	0.2415	0.4352
	δ_2	0.1938	0.3239	0.2789	0.2924
	δ_3	0.1866	0.2660	0.2543	0.2735
BSG, MAC	δ_1	0.0834	0.2075	0.2066	0.4354
	δ_2	0.1914	0.2906	0.2709	0.2916
MAC, TAC	δ_2	0.1923	0.2840	0.2718	0.3413
	δ_3	0.1887	0.2430	0.2516	0.3231
BSG, TAC	δ_1	0.1031	0.2010	0.2248	0.4974
	δ_3	0.1885	0.2575	0.2452	0.2947
BSG	δ_1	0.1069	0.2020	0.4075	0.5985
MAC	δ_2	0.2479	0.3254	0.4058	0.4042
TAC	δ_3	0.2097	0.2595	0.3680	0.3640

To obtain good model accuracies and capture the chacteristics of the dynamics of the system as much as possible, it is necessary to use as many measured outputs as possible in identification, because only one measured output may not reflect the dynamics of the system completely. Thus, the selected ensemble data with three measured outputs are used in the following analysis.

4.4.3 Relationships between the Model Order and Model Accuracy

In previous identification calculation, the model order has been chosen to be $n_x = 14$ for all the cases. This order may be too high for some cases. Meanwhile, to understand how the identified system order n_x affects the model accuracy, the relationship between the model order n_x and the model accuracy is examined.

Using the selected ensemble data with the three measured outputs and a block row number of 50, a series of the models were identified by varying n_x from 2 to 20 in a step size of 2. Figure 4.4.8 plots the overall RMS error indices δ vs the model order n_x for each combination of the two motion speeds and two scenarios. For both motion speeds of scenario A, a threshold order is 4 as the model accuracies change little after $n_x = 4$. Thus, the two vibratory modes are excited in the measured outputs of scenario A; For scenario B, a higher order is needed as more vibratory modes are excited. In the case of the fast motion, a threshold order is 12. In the case of the slow motion, a threshold order is 14.

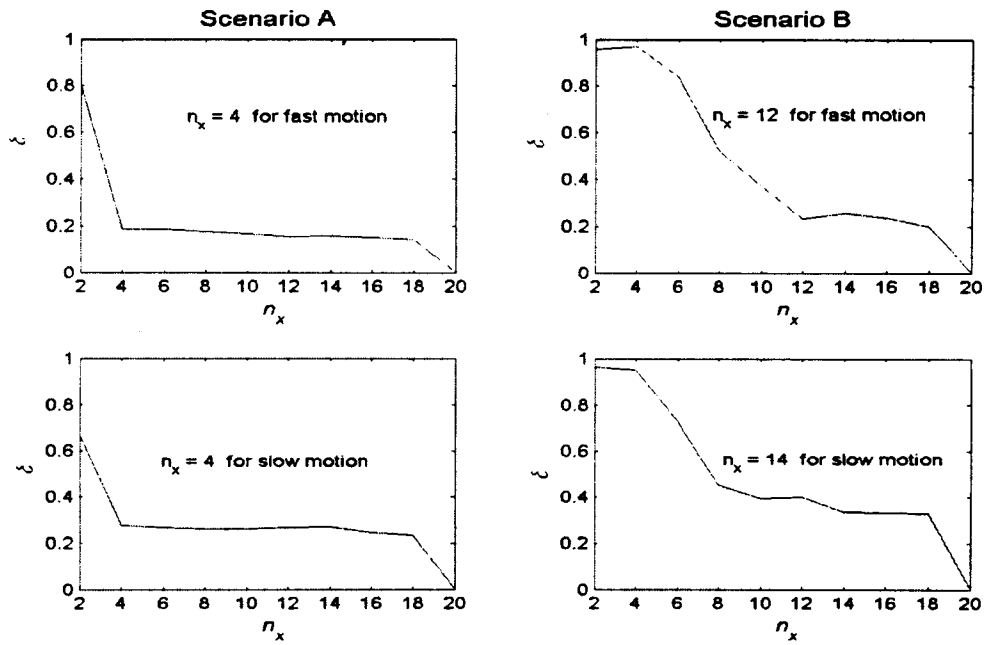

Figure 4.4.8 $(\delta - n_x)$ curves for each combination of the two motion speeds and two scenarios

4.4.4 Relationships between the Block Row Number and Model Accuracy

The row block number M is another important parameter in the identification. To understand how the block row number M influences the model accuracy and output accuracies, the relationships between δ and M are examined. The threshold model orders n_x and selected ensemble data are used in the following analysis.

Figure 4.4.9 shows comparison of the $(\delta - M)$ relationships for each combination of the two motion speeds and two sceanrios.

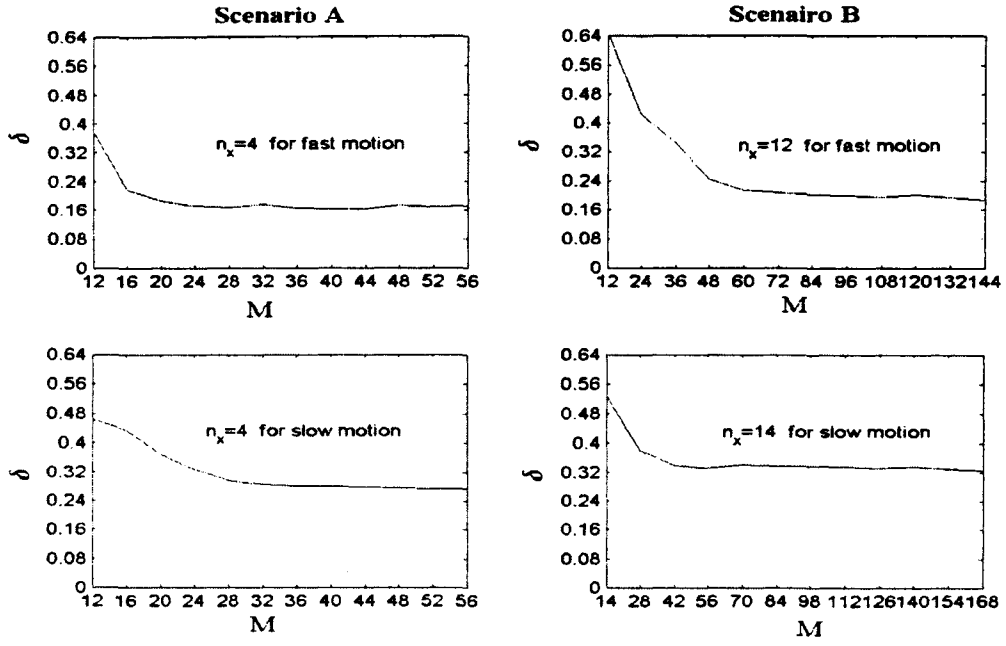

Figure 4.4.9 $(\delta - M)$ curves for each combination of the two motion speeds and two scenarios

The greater the block row number M, the smaller the magnitudes of δ, and the better the model accuracies. However, for their thresholds of model order n_x, the variations of magnitudes of δ are small when the M is greater than 20 for the fast motion and 32 for the slow motion under scenario A, and 60 for the fast motion and 56 for the slow motion under scenario B. Thus, the M has little effect on model accuracies as long as the M is greater than 20 for the fast motion and 32 for the slow motion under scenario A, 60 for the fast motion and 56 for the slow motion under scenario B.

4.4.5 Comparison between the Measured and Simulated Responses

In the previous sections, the degree of agreement between the measured and simulated responses was demonstrated using the defined RMS error indices. To have a visual comparison, Figures 4.4.10 and 4.4.11 display the comparisons between the simulated and measured responses for each case. The selected ensemble data and thresholds model orders n_x mentioned above are used in the following simulations. In addition, the block row number $M = 50$ are used for the fast and slow motions of scenario A. and $M = 60$ for the fast motion of scenario B and $M = 70$ for the slow motion of scenario B respectively. In the figures below, it is noted that a solid line represents the simulated outputs and a dashdot line measured outputs.

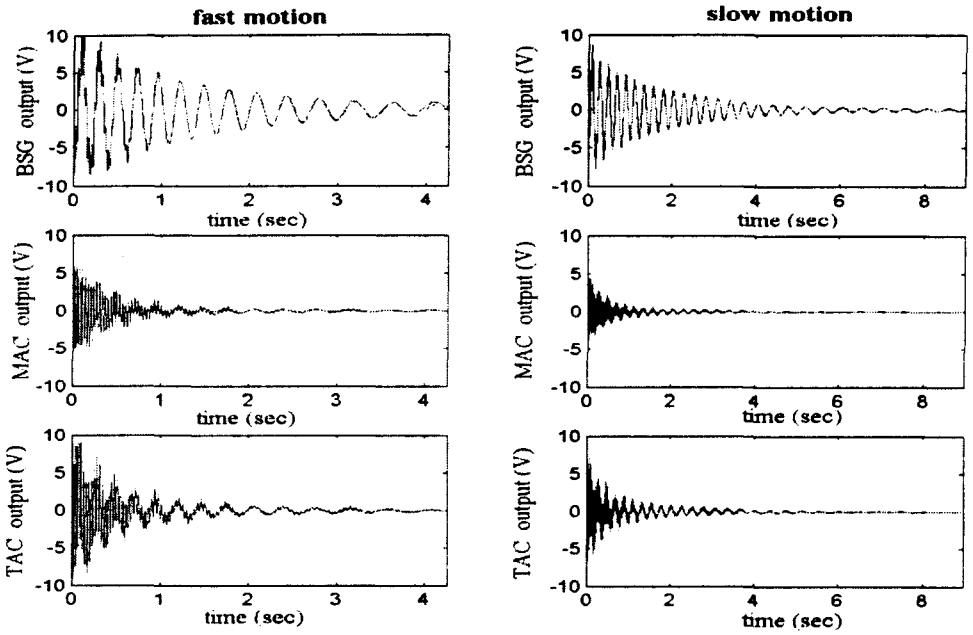

Figure 4.4.10 Comparison between the simulated and measured responses for scenario A

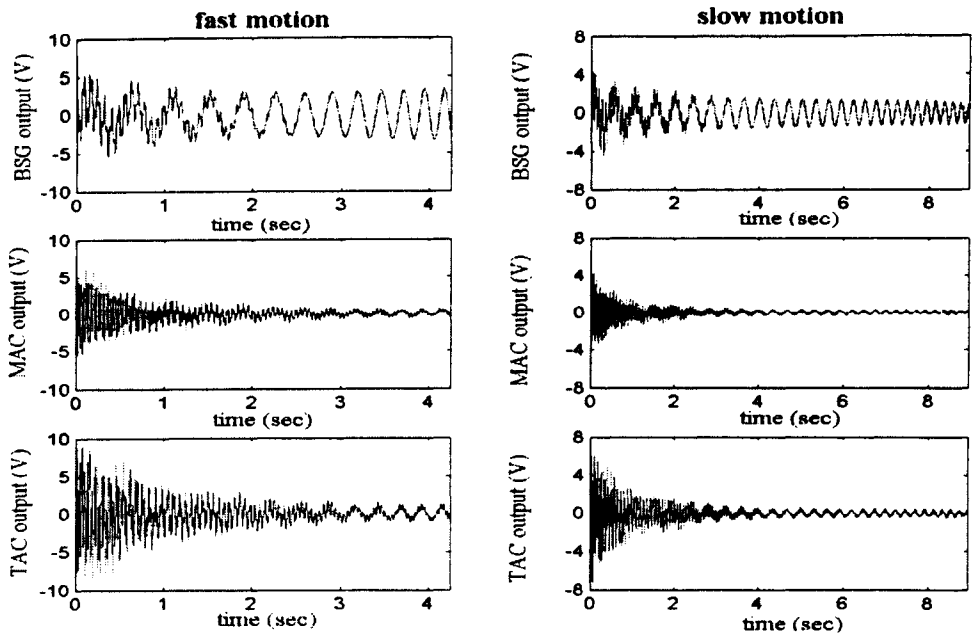

Figure 4.4.11 Comparison between the simulated and measured responses for scenario B

It can be seen that the simulated outputs agree well with the measured ones. Obviously, the outputs in scenario A decay faster than those in scenario B for the two motion speeds. The main reason is that the positive damping effect under scenario A is greater than that under scenario B since the axial extension causes the combination between the positive physical damping effects and the positive motion-induced damping one and the axial retraction causes the combination effect between the positive physical damping and the negative motion-induced damping, respectively.

4.5 Experimental Identification of "Pseudo" Natural Frequencies

In subsection 4.2.2, it was shown that the identified "pseudo" natural frequencies can be determined by eigendecomposition of the identified matrices $\widehat{G}(k+1,k)$. Here, the experimental identification of the "pseudo" natural frequencies is addressed. First, the identified "pseudo" natural frequencies are presented using the selected ensemble data. Next, the moving-average method is developed in order to select the "pseudo" natural frequencies of the vibratory modes.

Finally, the results of selection of identified "pseudo" natural frequencies of the vibratory modes are presented.

4.5.1 Identified "Pseudo" Natural Frequencies

Using the experimental data and the computational procedure in section 4.2.3, the matrix $\widehat{G}(k+1,k)$ in equation (4-2-19) can be obtained. Since the measured responses are contaminated by the noise and other unknown irregularities, the identified "pseudo" eigenvalue matrix $\widehat{\Lambda}(k)$ contains the complex pairs of eigenvalues and the real eigenvalues. Thus, the eigenvalue matrix $\widehat{\Lambda}(k)$ in equation (4-4-24) can be represented in another form

$$\widehat{\Lambda}(k) = \left[\begin{array}{ccccccccc} \widehat{\lambda}_1(k) & \widehat{\lambda}_2(k) & \cdots & \widehat{\lambda}_{n_1-1}(k) & \widehat{\lambda}_{n_1}(k) & \widehat{\lambda}_{n_1+1}(k) & \cdots & \widehat{\lambda}_{n_x}(k) \end{array} \right] \tag{4-5-1}$$

where $k = 0, 1, \cdots K_s - M - 1$ is the time instant. It is assumed that there are $n_1/2$ pairs of complex eigenvalues and eigenvectors at each time instant k. Thus, $\widehat{\lambda}_{i+1}(k) = \widehat{\lambda}_i^*(k)$ for $i = 1, 3, \cdots n_1 - 1$ are the pair of complex eigenvalues and eigenvectors, $\widehat{\lambda}_i(k)$ for $i = n_1+1, \cdots n$ are real eigenvalues. As shown in (4-5-1), the eigenvalues are arranged in such a way that the complex pairs of eigenvalues and real eigenvalues can be separated and grouped individually. Thus, the identified "pseudo" natural frequencies corresponding to the complex pairs of eigenvalues can be arranged as

$$\widehat{f}(k) = \left[\begin{array}{cccccc} \widehat{f}_1(k) & \widehat{f}_2(k) & \cdots & \widehat{f}_{n_1-1}(k) & \widehat{f}_{n_1}(k) \end{array} \right] \tag{4-5-2}$$

where

$$\widehat{f}_i(k) = \widehat{\omega}_i(k)/2\pi. \tag{4-5-3}$$

To understand how the identified "pseudo" natural frequencies are influenced by model order n_x, the identified "pseudo" natural frequencies are shown in Figure 4.5.1 using the threshold values of model order n_x and the values of block row number M mentioned in section 4.4.5. It is noted that the acronym $IPNF_i$ (ith identified "pseudo" natural frequencies) is used, or $IPNF_i(k) = \widehat{f}_i(k)$, in the following figures. It should be noted that the identified "pseudo" natural frequencies were grouped by sorting them in an ascending order according to their

magnitudes at each moment. The blue color represents the natural frequencies of the first group, green color of the second group, red color of the third group, cyan color of the fourth group, magenta color of the fifth group, yellow color of the sixth group, and black color of the seventh group.

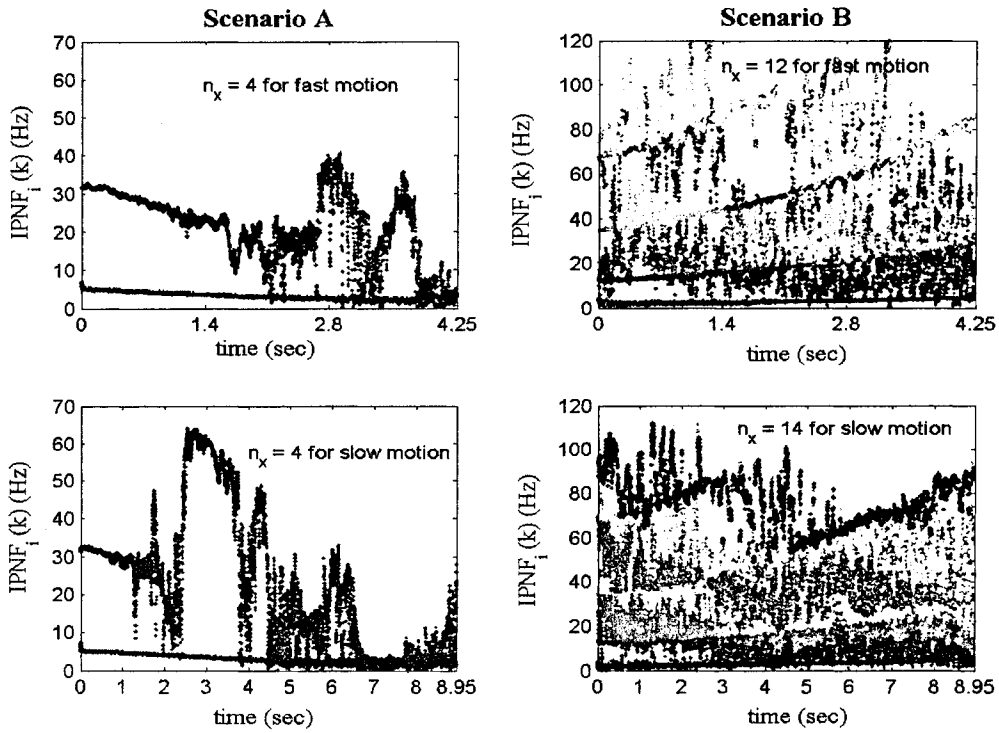

Figure 4.5.1 Identified "pseudo" natural frequencies $\widehat{f}_i(k)$ using the threholds n_x

Based on Figure 4.5.1 and the true "pseudo" modal parameters in section 3.3, the following observations can be drawn:

1. For scenario A, the identified "pseudo" natural frequency of the first vibratory mode can be observed using the the model order $n_x = 4$ while the "pseudo" natural frequency of the second vibratory mode can be observed for a short time period in begining.

2. For the case of the fast motion in scenario B, the variation trends of the first three "pseudo" natural frequencies are visible from clustering of the values of different groups. For example, the natural frequency of the third vibratory mode mainly consists of the values of the "cyan" group in begining, then the values of the "purple" group, finally the

values of the "yellow" group. In the case of slow motion, the identified values appear even more disorganized. This indicates that the sorting by magnitude ranking fails to group the identified "pseudo" natural frequencies properly.

3. If the model order is low, such as the case of scenario A, only the first mode was identified for the entire period of motion. In the case of scenario B, the model order of 12 was used and the first three vibratory modes were captured. However, with an increase of the model order, the computational modes were introduced.

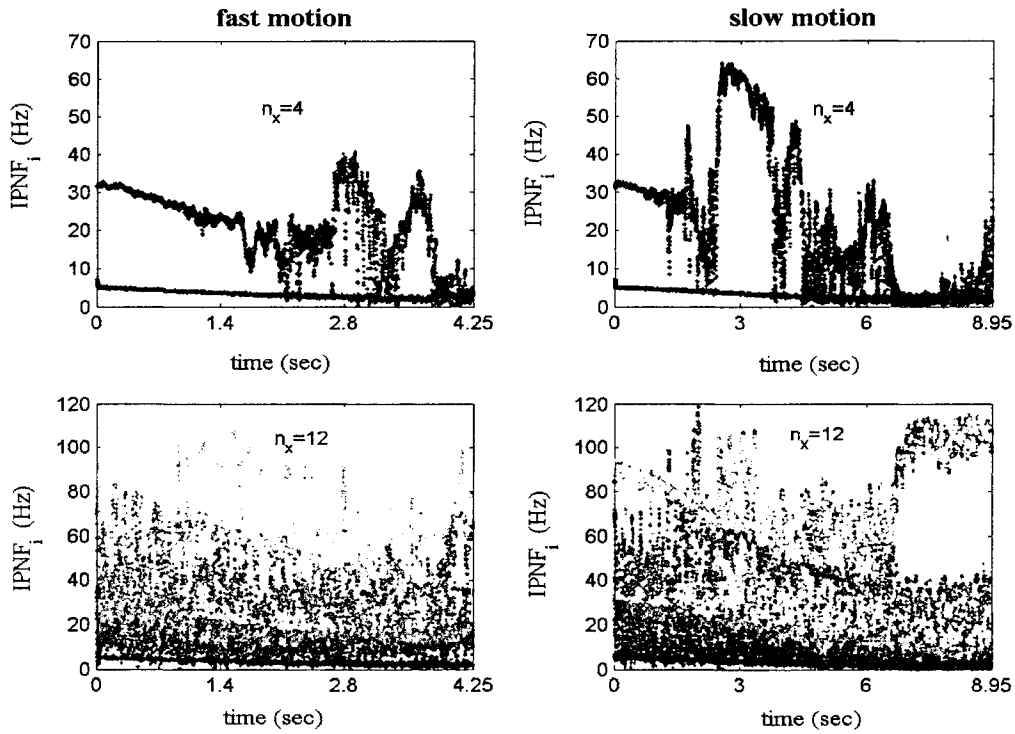

Figure 4.5.2 Comparison of $IPNF$s for $n_x = 4$ and $n_x = 12$ under scenarios A

Figure 4.5.2 shows the comparison of the "pseudo" natural frequencies identified using $n_x = 4$ and $n_x = 12$ for the fast and slow motions. It is noted that the color codes are the same as those mentioned in Figure 4.5.1 except for the seventh group of natural frequencies. This figure shows that the frequencies of the first three vibratory modes can be observed if the overparameterized model order $n_x = 12$ is used. From the observations, it is concluded that the overparameterized model order should be used in order to observe the variations of identified

"pseudo" natural frequencies of system vibratory modes.

4.5.2 Selection of the Identified "Pseudo" Natural Frequencies of the Vibratory Modes

From the descriptions given previously, the identified "pseudo" natural frequencies corresponding to the complex pairs of eigenvalues contain the natural frequencies of the vibratory modes and the computational modes at each time instant k if an overparameterized model order n_x is used. A natural question to ask is how the identified "pseudo" natural frequencies of the vibratory modes given by

$$f_i^s(k) \quad i = 1, 2, ..n, \text{ and } n \leqslant n_1, \ k = 0, 1, ..., K \tag{4-5-5}$$

are selected from the identified "pseudo" natural frequencies corresponding to the complex pairs of eigenvalues in equation (4-5-2), where n is the vibratory modes considered. The answer to the question is that $f_i^s(k)$ can be determined based on the principle that the values of $f_i^s(k)$ should be as close as possible to the reference values of the natural frequencies of the vibratory modes given by

$$f_i^r(k) \quad i = 1, 2, ..., n. \tag{4-5-6}$$

The reference values $f_i^r(k+1)$ at the time instant $k+1$ can be determined using the moving-average method. The method is used to calculate the reference values of the natural frequencies $f_i^r(k+1)$, based on average of the identified "pseudo" natural frequencies of the vibratory modes that are selected from the identified "pseudo" natural frequenices in the time period block $(k \leqslant k_1 \leqslant k + M_1 - 1)$. The selected natural frequencies expressed in

$$f_i^s(k_1) \quad (k \leqslant k_1 \leqslant k + M_1 - 1) \tag{4-5-7}$$

should be as close to the reference values $f_i^r(k)$ at time instant k_1 in the varying time period block, where the M_1 is the time period block number.

To select the "pseudo" natural frequencies of the vibratory modes given in (4-5-5) for $k = 0, 1, 2, ...K_s - M - 1$, the following procedure is developed.

1. Specify the initial reference values of the natural frequencies of vibratory modes $f_i^r(0)$;

2. Set up the time period block from k to $k + M_1 - 1$;

3. Select all $f^s(k_1)$ from $\widehat{f}(k_1)$ in (4-5-3) in the time period block ($k \leqslant k_1 \leqslant k + M_1 - 1$) based on the principles that all $f^s(k_1)$ should be as close to the reference values $f^r(k)$ as possible, calculate the average value of all $f^s(k_1)$ in the time period block given as

$$\overline{f_i^r}(k) = \frac{1}{M_1 - 1} \sum_{k_1=k}^{k+M_1-1} f_i^s(k_1). \tag{4-5-8}$$

If $k < K_s - M - M_1 - 1$, increase k by 1, let $f_i^r(k+1) = \overline{f_i^r}(k)$, and go to step 2; If the $k = K_s - M - M_1 - 1$, $f_i^s(k)$ are selected from $\widehat{f}(k)$ based on the principle that $f_i^r(k)$ should be as close to the reference values $f_i^r(K_s - M - M_1 - 1)$ as possible in the time period block $(K_s - M - M_1 - 1) \leqslant k \leqslant (K_s - M - 1)$.

4.5.3 Results of Selection of the Natural Frequencies of the Vibratory Modes

The natural frequencies of the vibratory modes at the two extreme fixed lengths listed in Table 4.1.1 are used as the initial reference values of the natural frequencies of the vibratory modes. For three vibratory modes considered, or $n = 3$, the natural frequencies of the first three vibratory modes at the shortest fixed length given by $f^r(0) = [4.9325 \quad 31.5350 \quad 87.66]$ are used as the initial reference values for motion scenario A, and the natural frequencies of the first three vibratory modes at the longest fixed length given by $f^r(0) = [1.9635 \quad 12.389 \quad 35.016]$ are used as the initial reference values for motion scenario B.

Figure 4.5.3 and Figure 4.5.4 show the identified "pseudo" natural frequencies of the first three vibratory modes considered using the parameters $n_z = 12$ and $M = 50$ for the fast and slow motions of scenario A, $n_z = 12$ and $M = 60$ for the fast motion of scenaro B, $n_z = 14$ and $M = 70$ for the slow motion of scenario B. The time period block number $M_1 = 200$ are also

used.

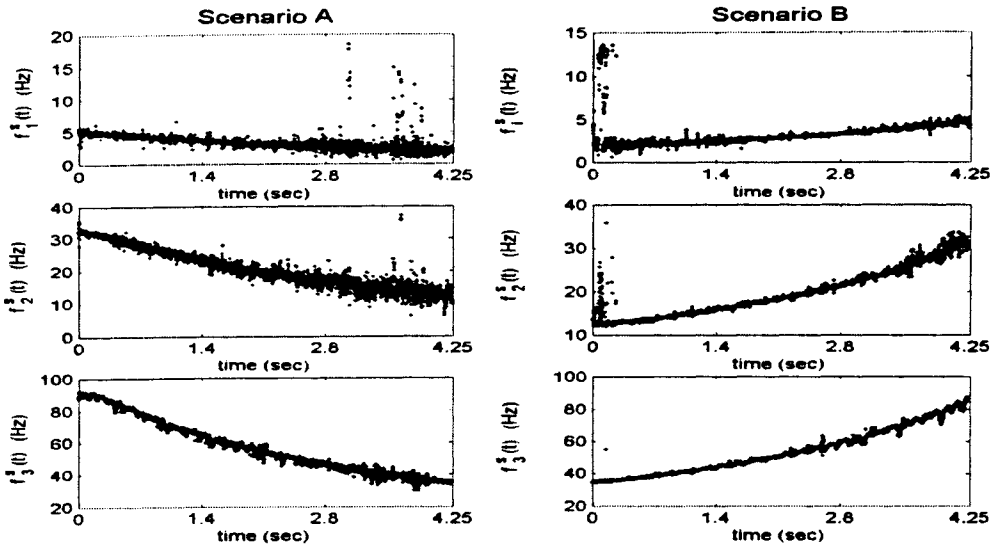

Figure 4.5.3 $IPNF$s of vibratory modes for fast motions under scenarios A and B

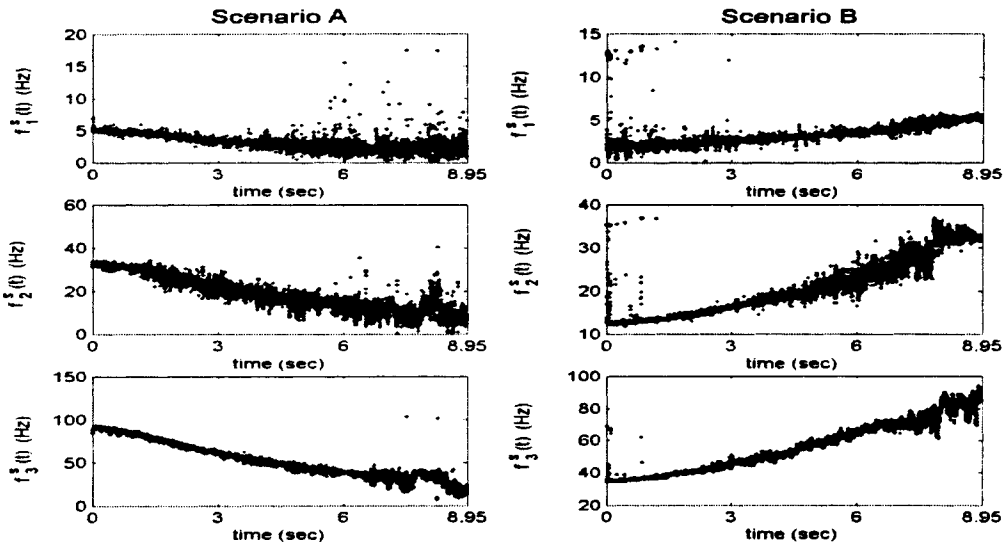

Figure 4.5.4 $IPNF$s of vibratory modes for slow motions under scenarios A and B

It can be seen that the variations of the identified "pseudo" natural frequencies of the first three vibratory modes are similar to those of the true values mentioned in Chapter 3, i.e., the identified "pseudo" natural frequencies of the first three vibratory modes vary from high values to low values for scenario A and from low values to high values for scenario B. It is noted that

the identified "pseudo" natural frequencies of vibratory modes fluctuate around their overall trends due to the fact that the measured outputs used in identification are contaminated by the noise.

Meanwhile, M_1 is an important parameter in selecting the identified "pseudo" natural frequencies of vibratory modes. Figures 4.5.5 and 4.5.6 show the comparison of the identified "pseudo" natural frequencies of the vibratory modes for $M_1 = 10$ and $M_1 = 50$ for fast and slow motions under scenario A, respectively. Figures 4.5.7 and 4.5.8 show the comparison of the identified "pseudo" natural frequencies of vibratory modes for $M_1 = 100$ and $M_1 = 200$ for fast and slow motions in scenario B, respectively.

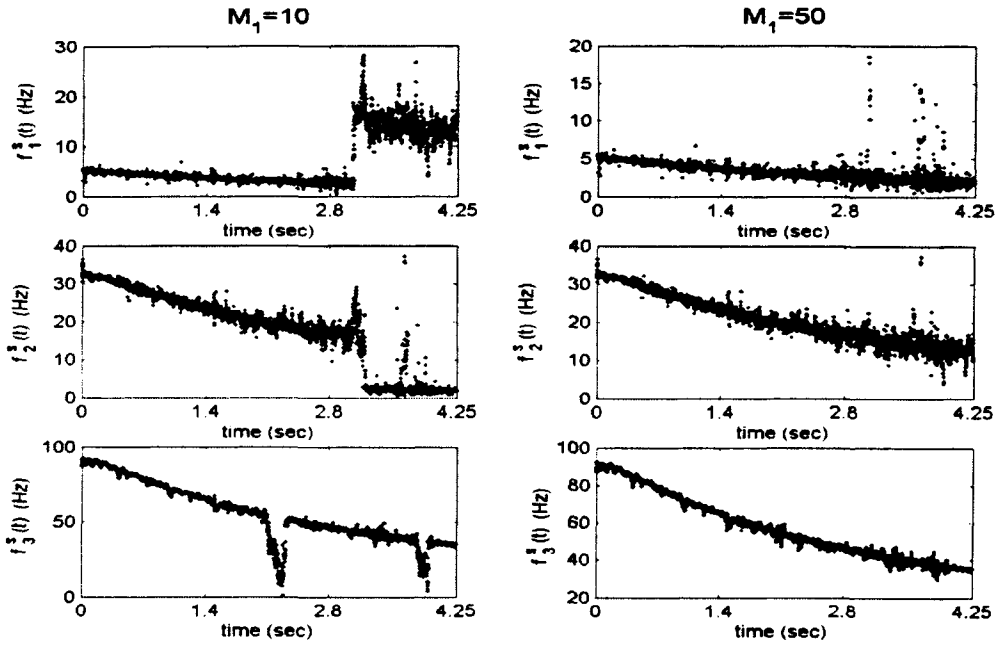

Figure 4.5.5 Selected frquencies using M_1=10 and those using M_1=50 for fast motion of scenario A

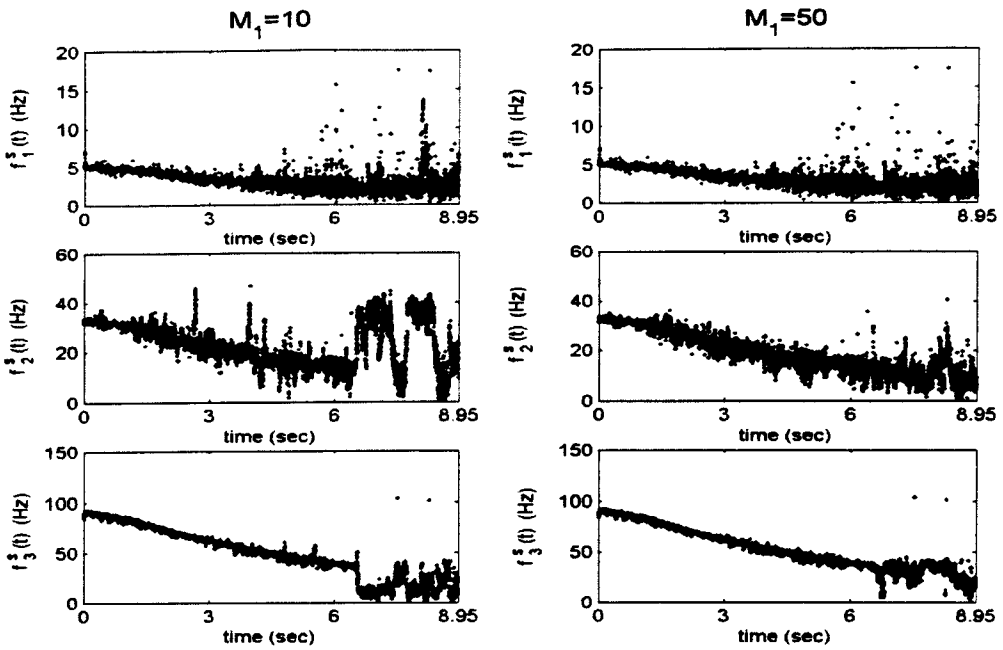

Figure 4.5.6 Selected frquencies using M_1=10 and those using M_1=50 for slow motion of scenario A

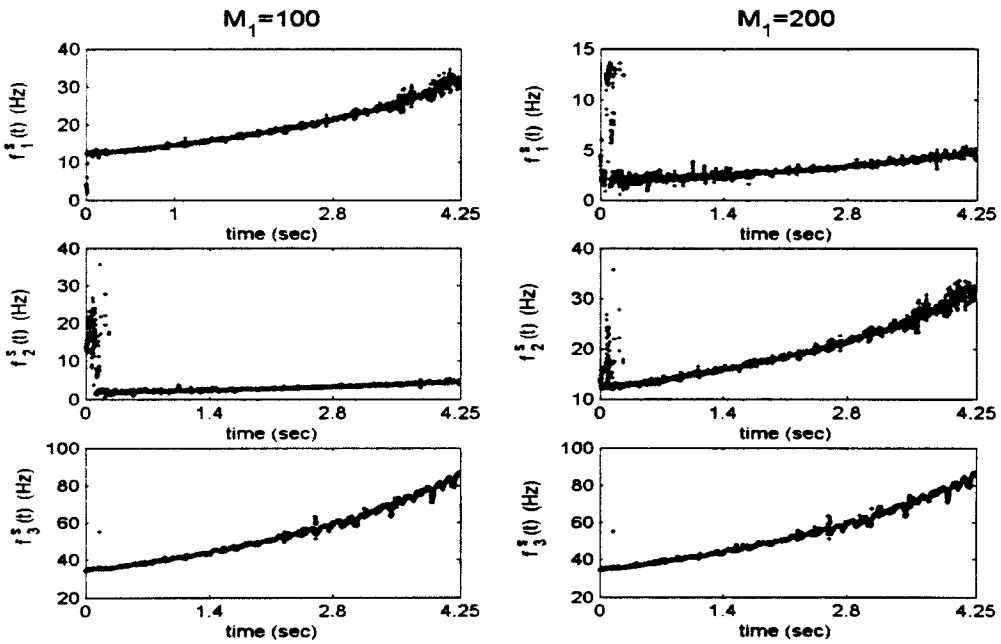

Figure 4.5.7 Selected frquencies using M_1=100 and those using M_1=200 for fast motion of scenario B

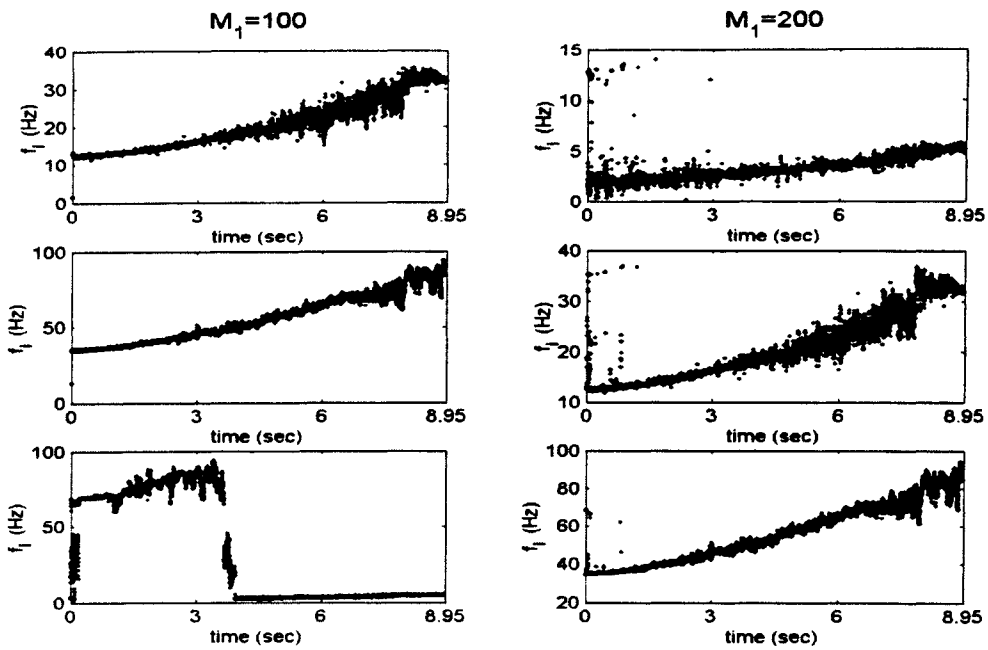

Figure 4.5.8 Selected frquencies using M_1=100 and those using M_1=200 for slow motion of scenario B

From the above figures, it is concluded that the identified "pseudo" natural frequencies of the vibratory modes selected are not reasonable if M_1 values are too small. Similarly, the variations of identified "pseudo" natural frequencies of the vibratory modes are also not reasonable if M_1 is too large. How to determine a proper value of M_1 is a topic for the future work.

4.6 Conclusions

Based on the results presented in this chapter, the following conclusions can be drawn:

1. The identification algorithm can only obtain a good approximation for the natural frequencies of the vibratory modes. However, it cannot give a meaningful estimate of the damping ratios of the vibratory modes.

2. To obtain the best identification results, it is necessary

   (a) to ensure that the system must undergo the same time-varying variation;

   (b) to generate the measured responses as independently as possibly;

(c) to use the multiple measured outputs instead of one measured output;

(d) to force the measured responses to be zeros mean;

(e) to select a small set of ensemble data from the original ensemble data.

3. The motion speed and motion scenario have a direct effect on the model accuracies.

4. To observe as many "pseudo" natural frequencies of the vibratory modes as possible, it is necessary to use the overparameterized model order.

5. The moving-average method obtains the sensible results for the variations of the identified "pseudo" natural frequencies of the vibratory modes for each combination of the motion speeds and the scenarios.

Chapter 5

Summary and Future Work

The summary of the thesis study is described as follows

1. A circuitry for DC motor current control and sensor signal conditioning has been built. The circuitry meets the requirements of controlling the axial motion of the cantilever beam and amplifying the sensor signals.

2. An analytical modeling procedure has been conducted to model the lateral vibration of an axially-moving cantilever beam. The simulation results confirm that the axial motion influences the dynamics of the system, including transient responses and " frozen" modal parameters. To evaluate the discrete-time state transition matrix reasonably, the system must undergo the same variation and an ensemble of n_x sets of initial states must be generated randomly. The "pseudo" modal parameters are evaluated by conducting eigendecomposition of the discrete-time state transition matrix. The simulation results indicate that the "pseudo" modal parameters are almost identical to the "frozen" ones for the system under study.

3. A previously developed algorithm has been applied to identify the system. The study has addressed several important issues, such as the methods of exciting system, evaluation of model accuracies, factors influencing model accuracies, relationships between model accuracies and parameters used in identification, selection of natural frequencies of the vibratory modes from identified "pseudo" natural freqeuncies. It has also been shown that the identification algorithm can provide a sensible approximation for natural

frequencies of the vibratory modes but cannot provide a reasonable estimation for damping ratios. The moving-average algorithm can be used to select the identified "pseudo" natural frequenciees of vibratory modes among the identifiied modes.

Recommendations for future work are:

1. to determine a proper value of time block number M_1 in order to obtain a better result of identified "pseudo" natural frequenices of the vibratory modes.
2. to implement identification algorithms based on forced responses of the axially-moving cantilever beam to ensure that the vibratory modes can be fully excited.
3. to develop a model reduction and updating method.

Bibliography

[1] B. Tabarrok, C. M. Leech and Y. L. Kim, " On the Dynamics of an Axially Moving Beam ", *Journal of the Franklin Institute* (1974) , 297(8), pp.201-220.

[2] A. K. Misra and V. J. Modi, " Deployment and Retrival of Shuttle Supported Tethered Satellites ", *Journal of Guidance* (1982), 5(3), pp.278-285.

[3] N. G. Chalhoub and A. G. Ulsoy, " Dynamic Simulation of a Leadscrew Driven Flexible Arm and Controller ", *Journal of Dynamic Systems, Measurement, and Control* (1974) , 108, pp.201-220.

[4] P. K. C. Wang and Jin-Duo Wei, " Vibration in a Moving Flexible Robot Arm ", *Journal of Sound and Vibration* (1987) , 116(1), pp.149-160.

[5] K. Krishnamurthy, " Dynamic Modeling of a Flexible Cylinderical Manipulator ", *Journal of Sound and Vibration* (1989) , 132(1), pp.143-154.

[6] S. H. Hyun and H. H. Yoo, " Dynamic Modeling and Stability Analysis of Axially Oscillating Cantilever Beam ", *Journal of Sound and Vibration* (1999) , 228(3), pp.543-558.

[7] W. D. Zhu and J. Ni, " Energetics and Stability of Translating Media with an Arbitrary Varying Length ", *Journal of Vibration and Acoustics* (2000) , 122, pp.295-304.

[8] A. Kumaniecka and J. Niziok, " Dynamic Stability of A Rope with Slow Variability of the Parameters ", *Journal of Sound and Vibration* (1994) , 178(2), pp.211-226.

[9] A. A. Renshaw, C. D. Rahn, J. A. Wichert, and C. D. Mote, Jr, " Energy and Conserved Functionals for Axially Moving Materials ", Transaction of the ASME (1998), 120, pp.634-636.

[10] B. Jacob, " A Formula for the Stability Radius of Time-Varying Systems ", *Journal of Differential Equations* (1998), 142, pp.167-187.

[11] H. Xiao and Y. Liu, " The Stability of Linear Time-Varying Discrete Systems with Time-Delay ", *Journal of Mathematical Analysis and Applications* (1994), 188, pp.66-77.

[12] S. Yang, " Observer-Based Robust Controller Design for a Linear System with Time-Varying Perturbations", *Journal of Mathematical Analysis and Applications* (1997), 213, pp.642-661.

[13] W. J. Rugh, " Linear System Theory ", 1996, Prentice Hall, Upper Saddle River, New Jersey.

[14] K. Liu, " Extension of Modal Analysis To Linear Time-Varying System ", *Journal of Sound and Vibration* (1999), 226(1), pp.149-167.

[15] K. Liu, " Adaptation of the Concept of Modal Analysis to Time-Varying Structures " . *Mechanical System and Signal Processing* (1999), 13(3), 413-422.

[16] K. Liu, " Identification of Linear Time-Varying System ", *Journal of Sound and Vibration* (1997), 206(4), pp.487-505.

[17] A. Benveniste, " Design of Adaptive Algorithm for the Tracking of Time-Varying System ". *International Journal of Adaptive control and Signal Processing* (1987),1, pp.3-29.

[18] S. Shokoohi and L. M. Silverman, " Identification and Model Reduction of Time-Varying Discrete-Time System", *Automatica* (1987), 23(4), pp.509-521.

[19] R. Ghanem, " A Wavelet-based Approach for the Identification of Linear Time-Varying Dynamical System ", *Journal of Sound and Vibration* (2000), 234(4), pp.555-576.

[20] K. Liu and D. W. Miller, " Time Domain State Space Identification of Structural System ". *Journal of Dynamic System, Measurement and Control* (1995), 116, pp.608-618.

[21] K. Liu and X. Sun, " System Identification and Modal Reduction for a Single-Link Flexible Manipulator", *Journal of Sound and Vibration (*2001*)*, 242(5), pp.867-897.

[22] X. Sun, " System Identification and Control of a Flexible Manipulator" , *Master Thesis* (2000), Lakehead University, Thunder Bay, Canada.

[23] J-N. Juang, "Applied System Identification", 1994, Prentice Hall, Englewood Cliffs, New Jersey.

[24] J-N. Juang and R. S. Pappa, "An Eigensystem Realization Algorithm for Modal Parameter Identification and Modal Resuction", *Journal of Guidence*, (1985), 8(5), pp.620-627.

[25] A. Fujimori, P. B. Nikiforuk and E. Koda, "Modelling of a Flexible Arm Using System Identifiecation and Model Reduction", Journal of system and Control Engineering (1985), 209, pp.13-20.

[26] S. Yu, " Control of Flexible-Link Manipulator", *Master's Thesis* (1997), Lakehead University, Thunder Bay, Ontario, Canada

[27] S. Benard, "Control of A Felxible Robotic Link Using LQR Control Algorithm", *Degree Project* (1996), Lakehead University, Thunder Bay, Ontario, Canada.

[28] D. J. Inman, "Engineering Vibration" , 1996, Prentice Hall, Upper Saddie River, New Jersey.

[29] A. Hage, "Design and Testing of a Variable Length Cantilever Beam Apparatus", *Degree Project* (2002), Lakehead University, Thunder Bay, Ontario,Canada.

[30] J. W. Dally, W. F. Riley and Kenneth G. McConnell, "Instrumentation for Engineering Measurement". 1984, John Wiley & Sons, Inc.

[31] J. D. Irwin, C. Wu, " Basic Engineering Circuit Analysis", 6th Edition, 1999, John Wiley & Sons, Inc, New York, U. S. A.

[32] J. R. Hanly, E B. Koffman, and J. C. Horvath, "C Progam Design for Engineer", 1995, Addison-Wesley Publishing Company, Inc, Menlo Park, California, U. S. A.

[33] R. H. Bishop, "Learing with LabVIEW", 1999, Addison-Wesley Publishing Company, Inc, Menlo Park. California, U. S. A.

[34] W. H. Press, S. A. Teukolsky, W. T. Vetterling, and B. P. Flannery, "Numerical Recipes in C", 2nd Editon, 1992, Cambridge University Press.

[35] J. E. Slotine, and W. Li, "Applied Nonlinear Control", 1991, Prentice Hall, Englewood Cliffs, New Jersey, U. S. A

[36] G. F. Franklin, J. D. Powell, and M. Workman, "Digital Control of Dynamic System", 3rd Edition, 1998, Addison wesley Longman, Inc, Menlo Park, California, U. S. A.

[37] K. Ogata, "Modern Control Engineering", 2nd Edition, 1990, Prentice Gall, Englewood Cliffs, New Jersey, U. S. A.

[38] M. W.Spong, and M. Vidyasagar, "Robot Dynamics and Control", 1989, John Wiley & Sons, Inc, New York, U. S. A

Appendix A

Schematic Drawings of the Circuits and The Testing Setups

Motor Power Supply Module

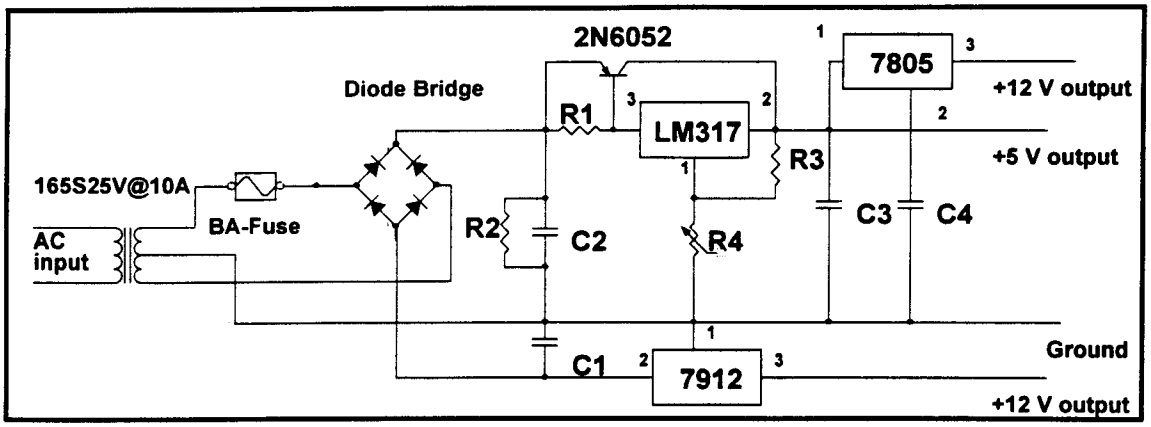

R1 =51 ohm	C1 = 470 uF
R2 = 4.7 kohm	C2 = 11000 uF
R3 = 270 ohm	C3= 2700 uF
R4 = 5 k ohm (variable)	C4= 2.2 uF

Figure A2.1 Motor Power Supply Module

Bridge Module

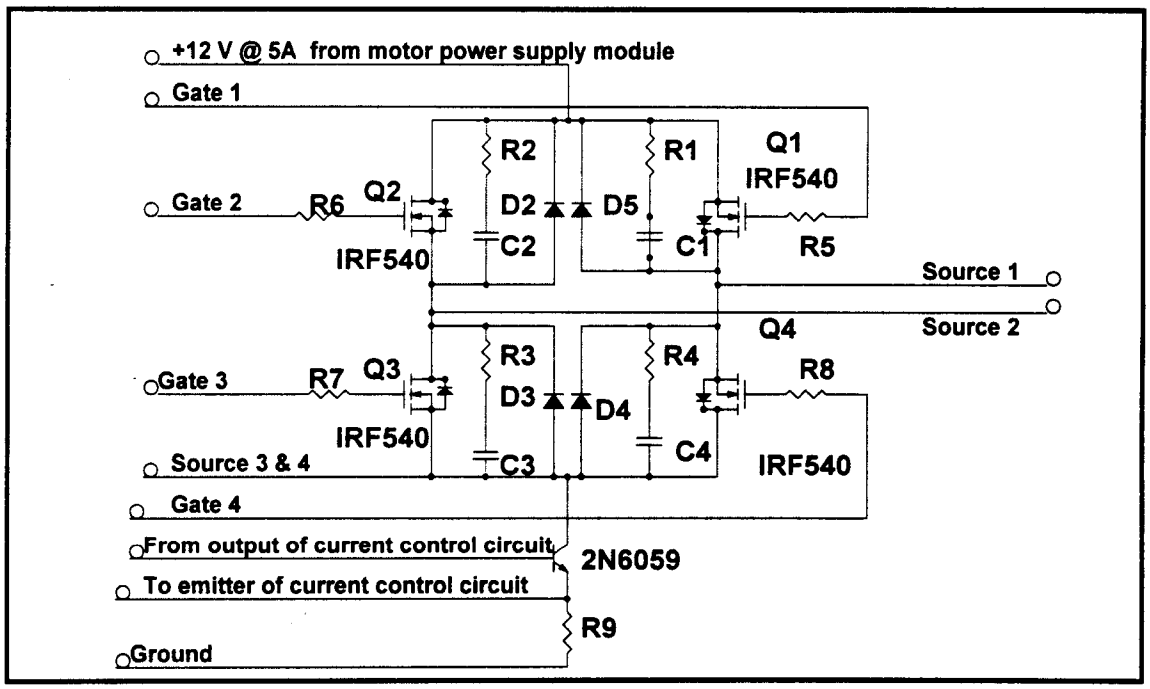

R1 = R2 = R3 = R4 = R9 = 1 ohm R5 = R6 = R7 = R8 = 12 ohm C1=C2=C3=C4=2.2 uF

Figure A2.2 Bridge Module

Current Control Module

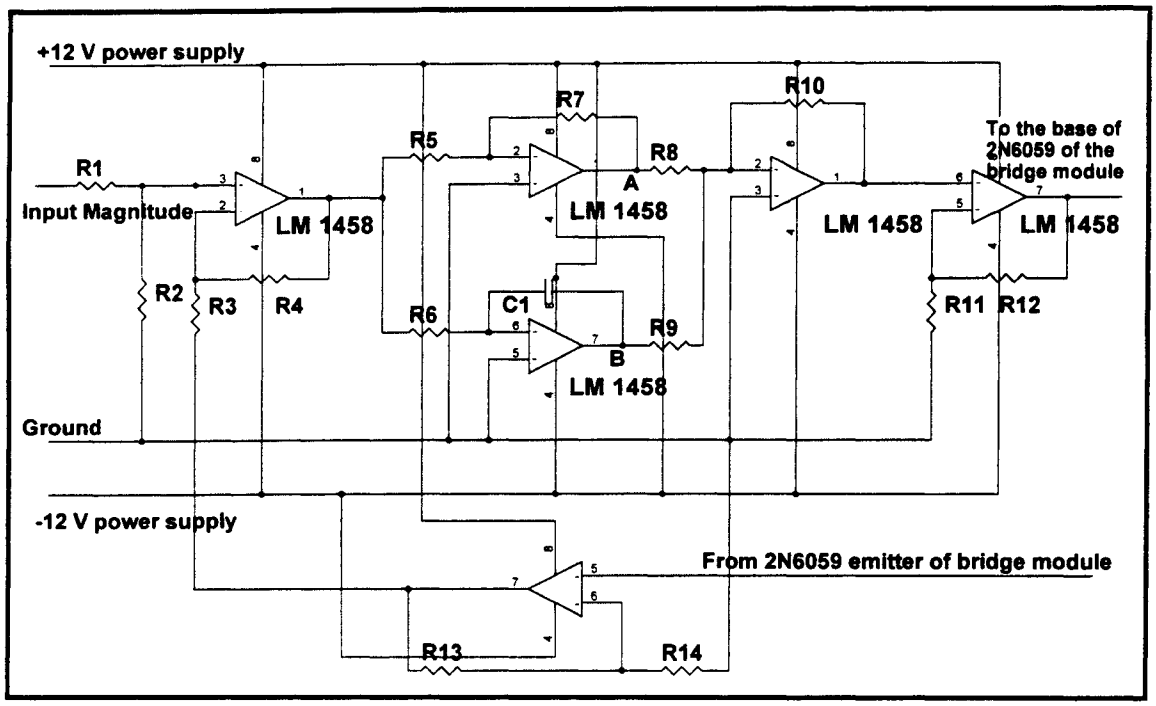

R1 = R2 = R3 = R4 = 2.2 khom
R5 = R8 = R9 = R10 = 1.2 khom
R6 =18 Kohm R7=180 ohm R11=82 kohm
R12 = 5.6 kohm R13 = R14 = 1 kohm C1=1.2nF

Figure A2.3 Current Control Module

Opto-Isolation Module "A & B"

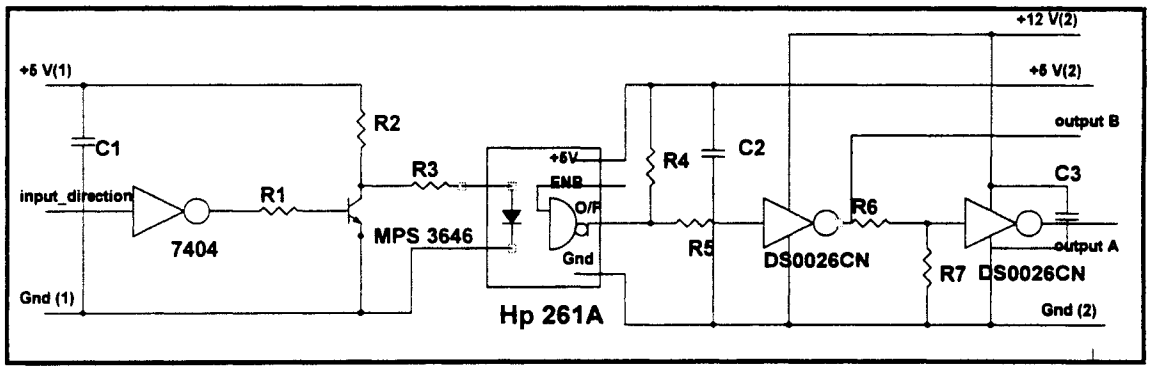

C1 = C2 = C3 = 0.1 uF R1 =4 .7 kohm
R2 = 580 ohm
R3 =160 ohm
R4 =1.0 kohm
R5 = 270 ohm
R6=10.0 kohm
R7 =5.6 kohm

Figure A2.4 Opto-Isolation Module " A & B "

Signal Separation Module

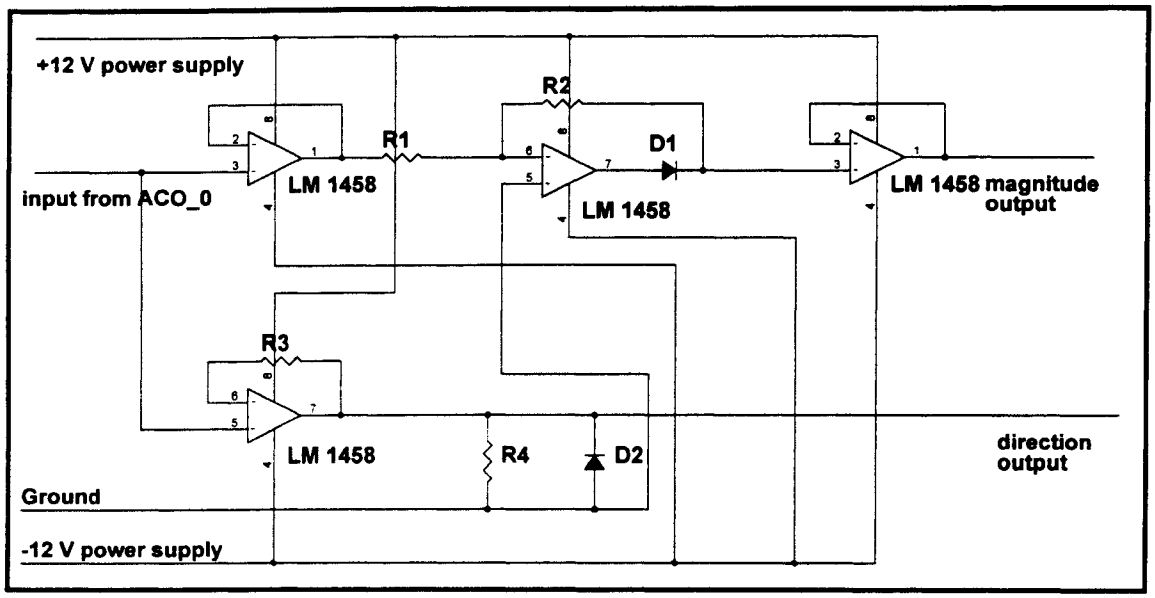

R1 = R2 = 10 kohm R3= 2.2 kohm R4 = 1 kohm

Figure A2.5 Signal Separation Module

Power Supply Module

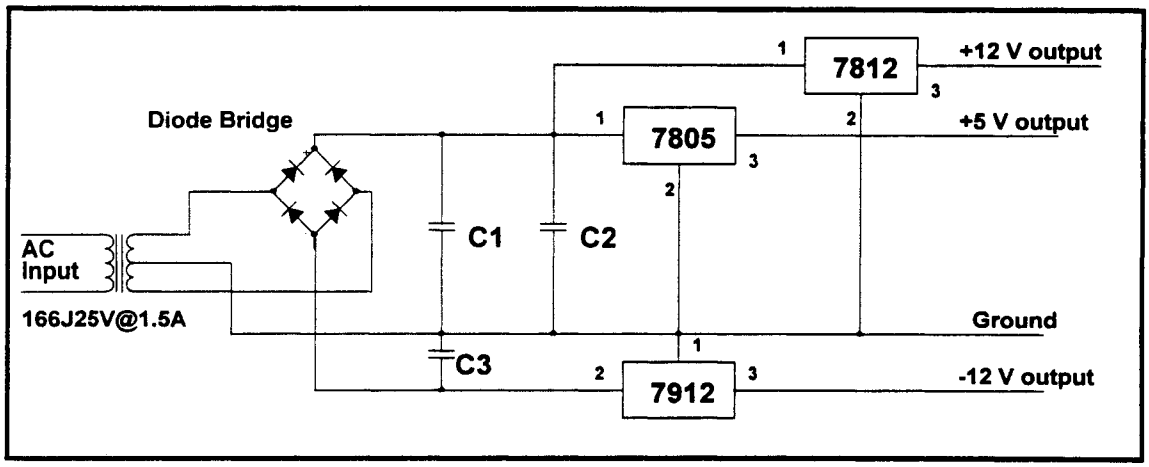

C1 = 470 uF C2 = 2700 uF C3= 470 uF

Figure A2.6 Power Supply Module

Potentiometer

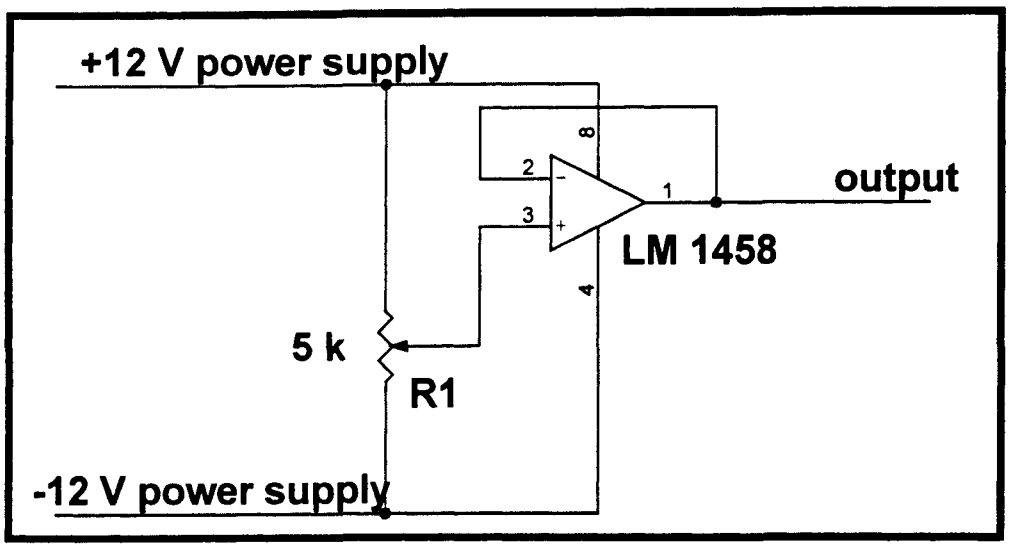

Figure A2.7 Potentiometer

Strain Gauge Module

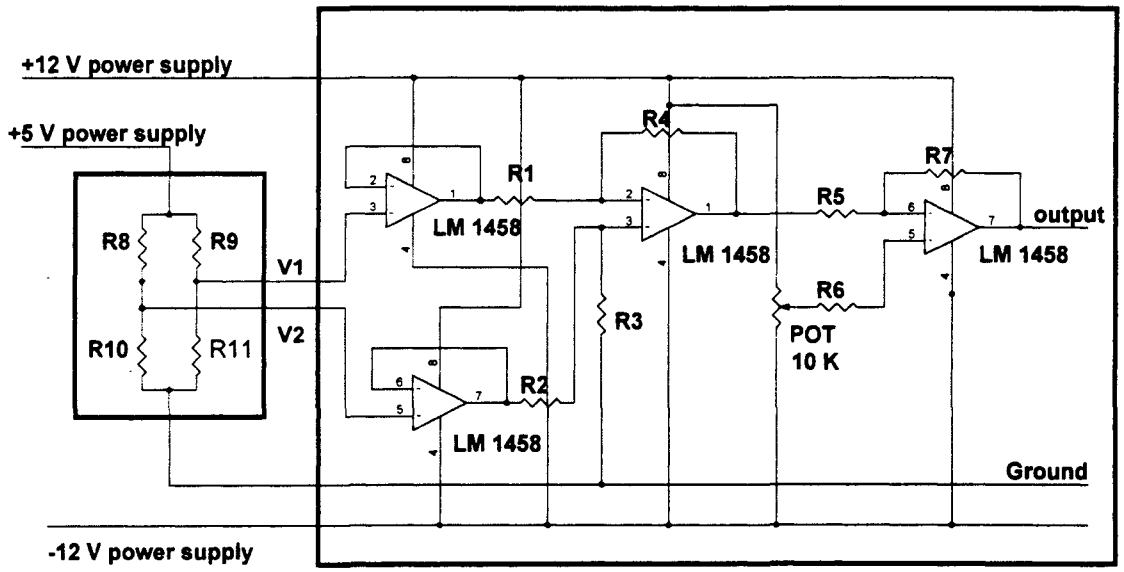

R1 = R2 = R5 = R6 = 1 kohm R8 = R9= R10= R11 = 120 ohm R3 = R4= 100 kohm R7 = 10 kohm

Figure A2.8 Strain Gauge Circuit

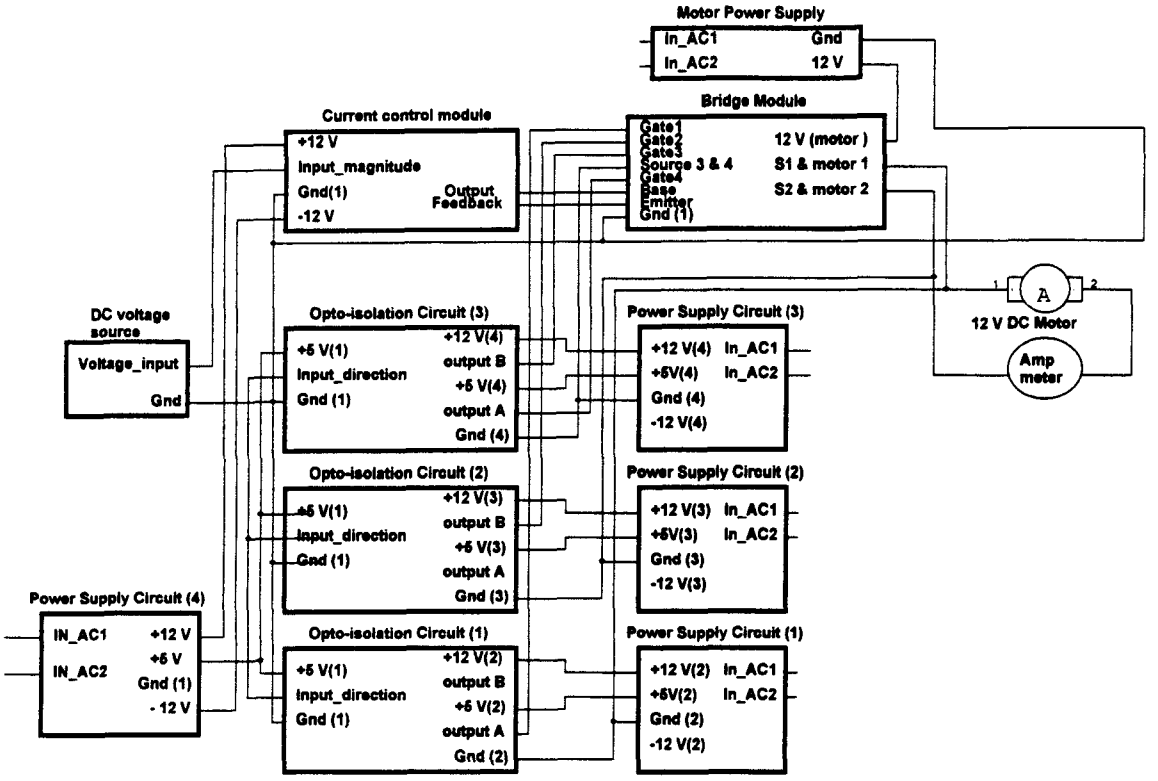

Figure A2.9 Testing Bridge Circuit and Measuring Motor Current

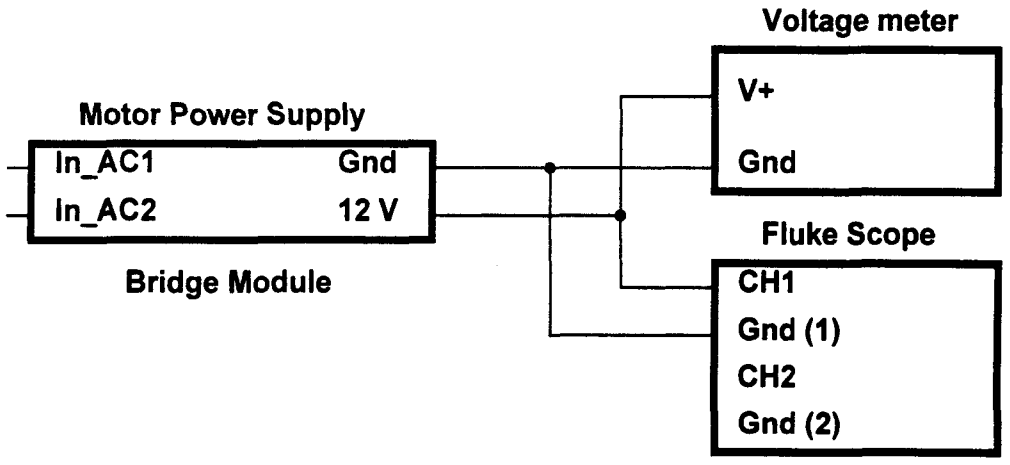

Figure A2.10 Testing Diagram of Motor Power Supply

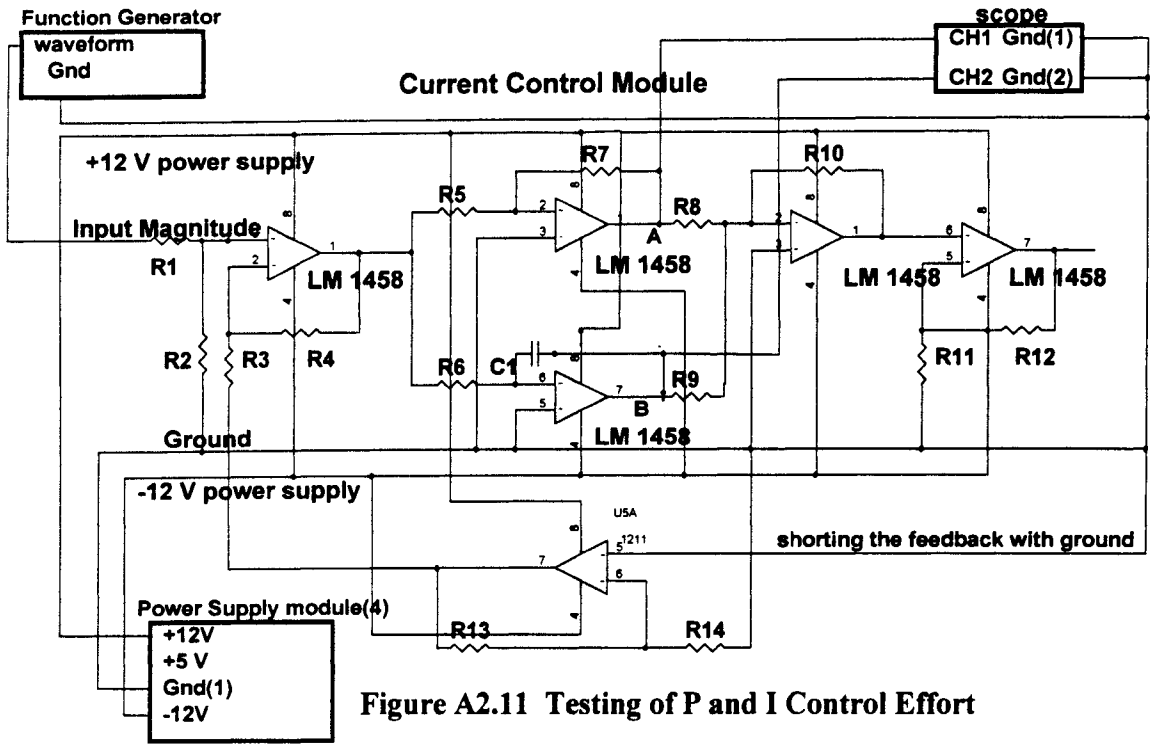

Figure A2.11 Testing of P and I Control Effort

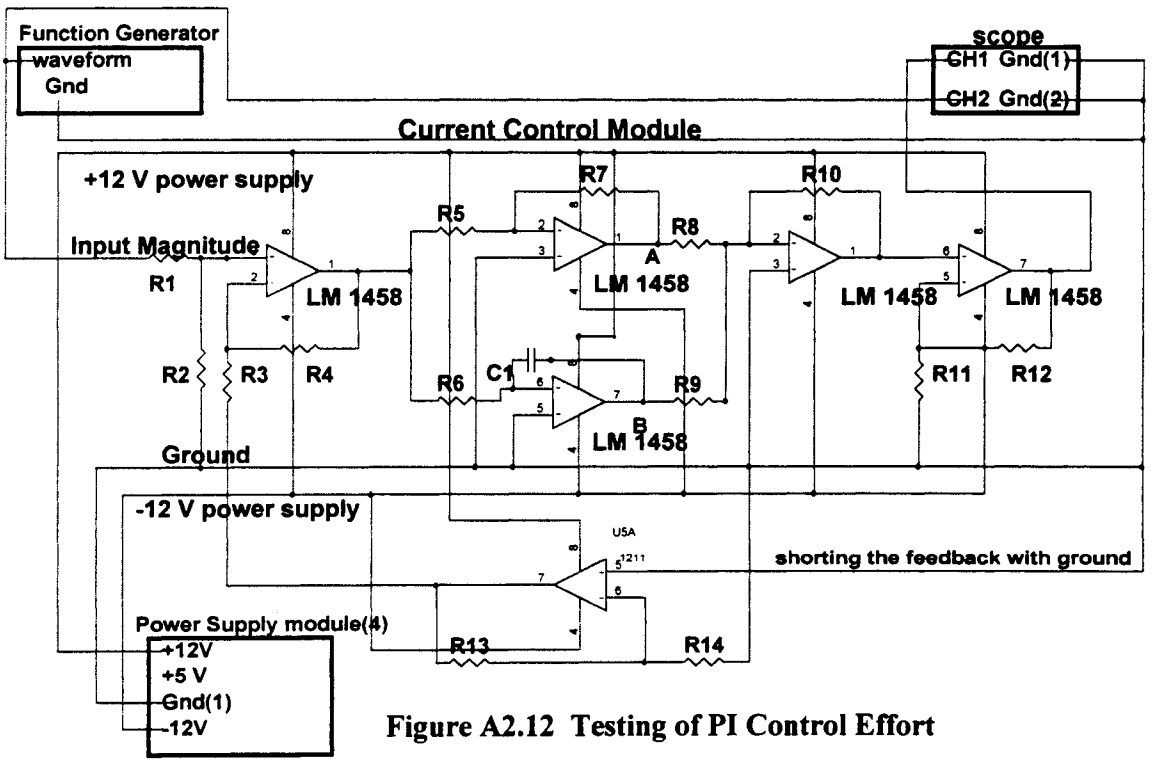

Figure A2.12 Testing of PI Control Effort

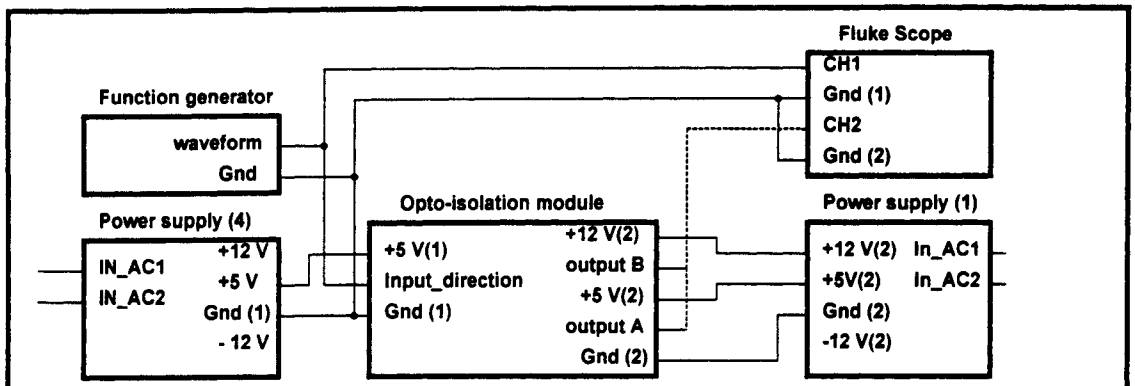

Figure A2.13 Testing Diagram of Opto-Isolation Module

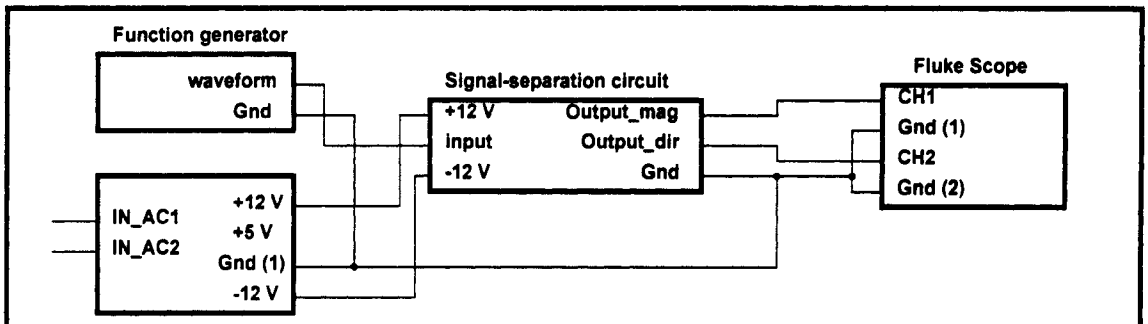

Figure A2.14 Testing of Signal-Separation Module

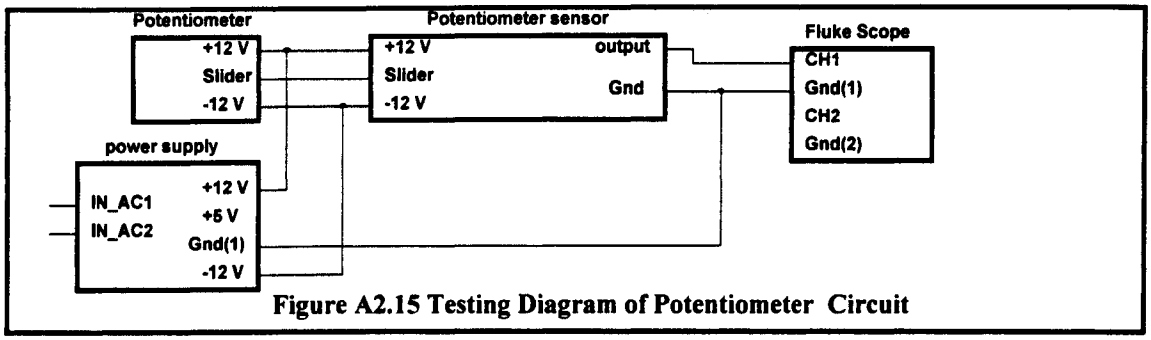

Figure A2.15 Testing Diagram of Potentiometer Circuit

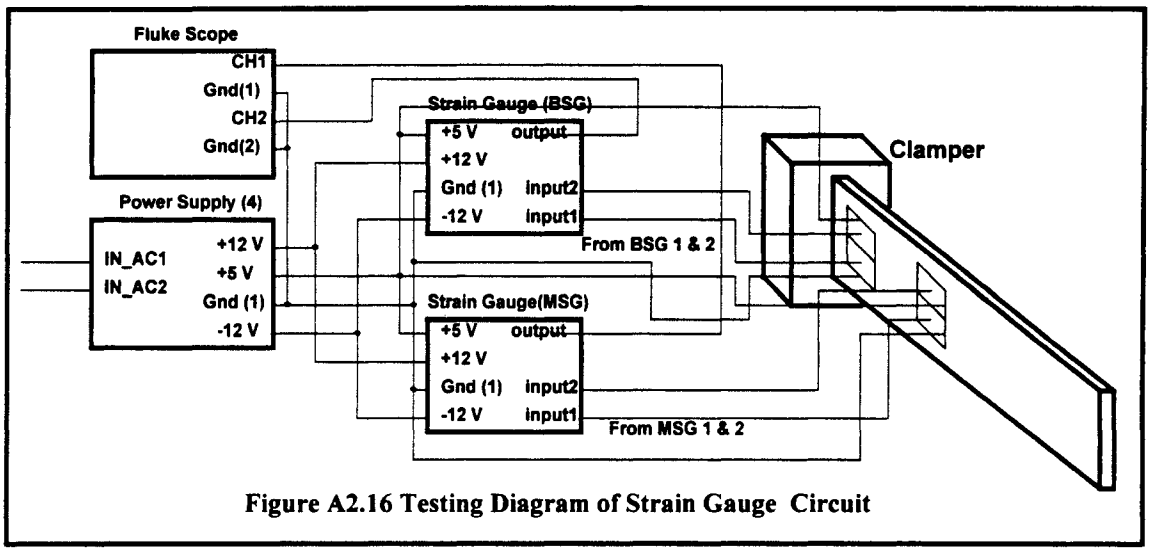

Figure A2.16 Testing Diagram of Strain Gauge Circuit

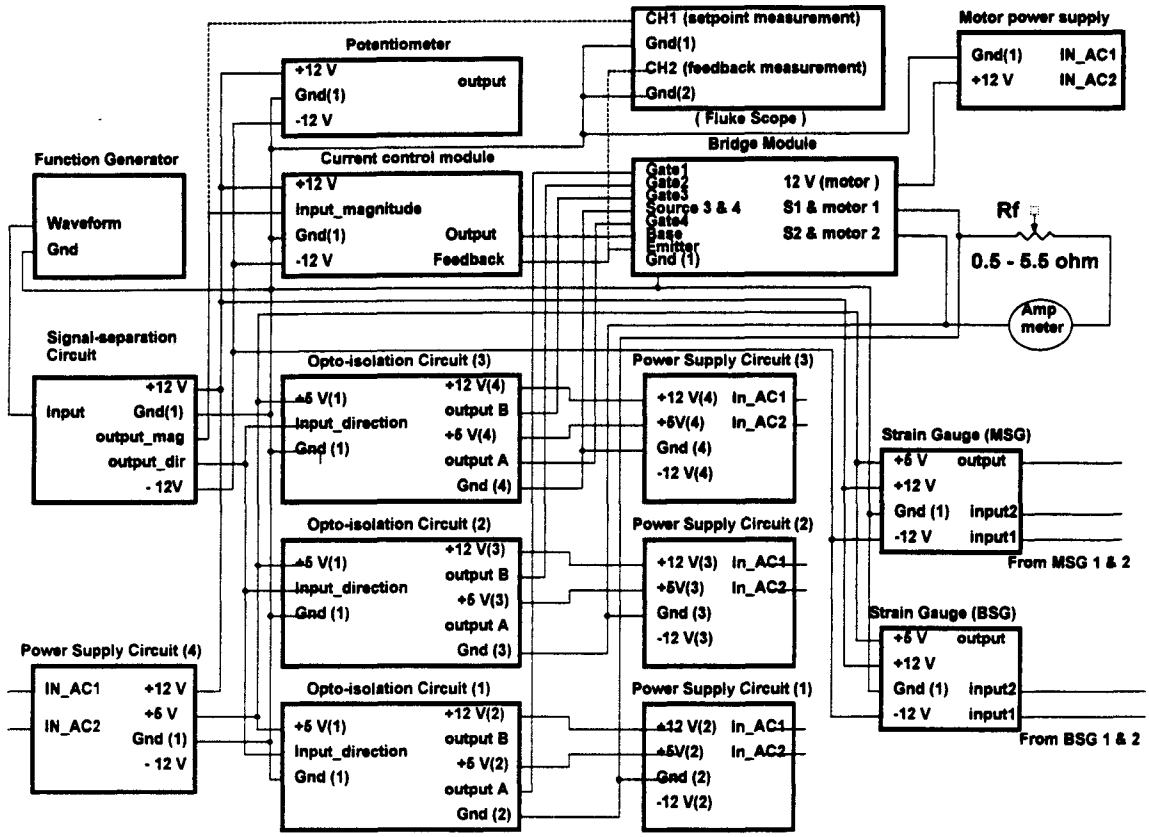

Figure A.2.17 Testing Diagram for Setpoint and Feedback Comparison

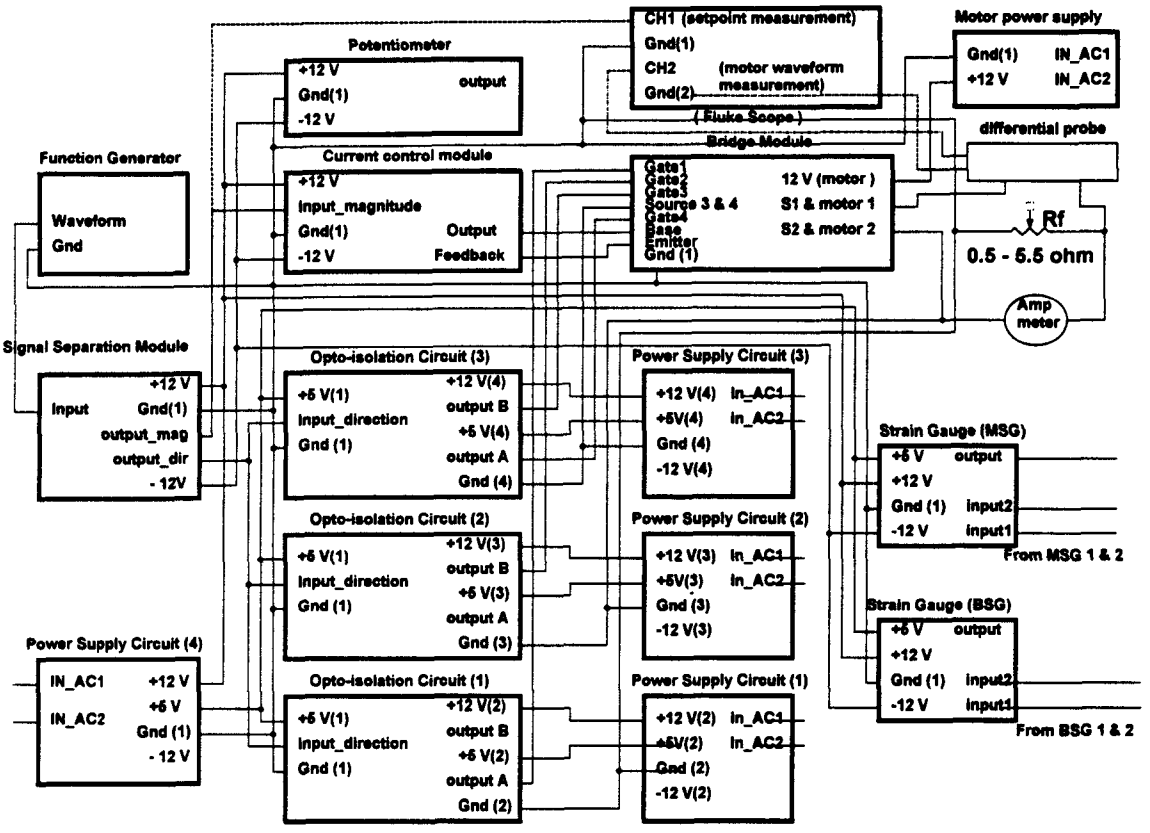

Figure A2.18 Testing Diagram for Setpoint and Motor Current Waveform